

The University of Southern Queensland

Faculty of Health, Engineering and Sciences

Quantifying the Effects of Convective Aerodynamic Heating over a Double Swept-Wedge Configuration at Mach 6

A dissertation submitted by

James Fuata

in fulfillment of the requirements of

Courses ENG4111 and ENG4112 Research Project

towards the degree of

Bachelor of Engineering (Mechanical)

Submitted: 30 October 2014

Abstract

This project sought to quantify the effects of convective aerodynamic heating over a double swept-wedge configuration at a nominal flow speed of Mach 6.

A Type K surface junction thermocouple and a mid-wave infrared camera were used to record surface temperature data, which was analysed and processed in MATLAB to determine the heat transfer rates into the model. Using the same software, surface heat flux maps were produced in order to identify and quantify regions of peak convective aerodynamic heating.

Two experimental runs (Run 280 and Run 285) were conducted at the University of Southern Queensland Hypersonic Wind Tunnel (TUSQ). The second test involved in-situ calibration of the infrared camera at the facility.

Calibration polynomial curves were generated from the calibration process and the most suitable curve was selected. This curve was then used to plot calibrated surface temperature and heat flux histories on the model.

Theoretical predictions were made of the local heat flux on the model. A modified oblique shock wave theory by Emanuel (1992), the ideal gas law and isentropic relations, were used to predict the flow conditions immediately downstream of the attached swept shock wave.

The analytical heat flux values for Run 280 and Run 285 were $3.95 \frac{kW}{m^2}$ and $3.88 \frac{kW}{m^2}$, respectively. In comparison, the heat flux values derived using the semi-infinite wall data reduction model for Run 280 and Run 285 were $34.5 \frac{kW}{m^2}$ and $29.2 \frac{kW}{m^2}$, respectively.

One of the main objectives of the project was achieved in identifying the regions of peak heating and visualising these areas with heat flux contour maps. Further work is required to adequately quantify calibrated heat flux values.

University of Southern Queensland
Faculty of Health, Engineering & Sciences

ENG4111 & ENG4112 Research Project

Limitations of Use

The Council of the University of Southern Queensland, its Faculty of Health, Engineering & Sciences, and the staff of the University of Southern Queensland, do not accept any responsibility for the truth, accuracy or completeness of material contained within or associated with this dissertation.

Persons using all or any part of this material do so at their own risk, and not at the risk of the Council of the University of Southern Queensland, its Faculty of Health, Engineering & Sciences or the staff of the University of Southern Queensland.

This dissertation reports an educational exercise and has no purpose or validity beyond this exercise. The sole purpose of the course pair entitled “Research Project” is to contribute to the overall education within the student’s chosen degree program. This document, the associated hardware, software, drawings, and other material set out in the associated appendices should not be used for any other purpose: if they are so used, it is entirely at the risk of the user.

Executive Dean

Faculty of Health, Engineering & Sciences

Certification

I certify that the ideas, designs and experimental work, results, analyses and conclusions set out in this dissertation are entirely my own effort, except where otherwise indicated and acknowledged.

I further certify that the work is original and has not previously been submitted for assessment in any other course or institution, except where specifically stated.

James Fuata

Student Number: 0050050764

Signature

Date

Acknowledgements

The last two years of this degree have been very challenging: dealing with the stress of experiencing two redundancies in the space of eight months, trying to get back into meaningful work in the engineering industry for over 18 months, all whilst trying to concentrate on doing well in my studies, and being the best family man that I could be. Undertaking this exciting and I think, difficult project in hypersonics and writing the dissertation didn't help with the stress levels either. Fortunately, my undergraduate journey is nearly over, which is marked by the submission of this dissertation.

I'd like to thank a few people. Firstly, Professor David Buttsworth (USQ), for taking time outside of his normal working hours to help me with the experiments and enlightening me on the fascinating world of hypersonics. You're a nice fellow, and the fact that you also specialise in hypersonics, is, well...cool.

A thank you also goes to Dr. Ray Malpress and Mr. Chris Galligan for manufacturing the sting for my model, and the model itself, respectively..

On the theoretical front, I'd like to thank Dr. George Emanuel. He's all the way in the Good 'ol USA, but he took the time to help me understand his modified oblique shock theory. Professor Larry Redekopp, whose pioneering work with the late Professor Andrew Charwat on characterising the flow over axial corners, is also to be thanked. I managed to track him down via the web, but when I did get in contact with him, he was more than happy to help.

To my beautiful children Aleah and Jacob: although neither of you will be able to read these words right now, Daddy wants you to know that he adores you both and his love and passion for you and your mum motivated him to climb this mountain of study and stress of being unemployed, especially over the last few years.

Lastly, I'd like to thank my darling wife Jennifer Leah Kokoska. Your love and belief in me can never be adequately expressed in words. You are my angel. Thank you for choosing me.

Contents

Chapter 1	1
Prepare for Takeoff	1
1.1 Introduction	1
1.2 Convective Aerodynamic Heating	2
1.3 Practical Significance of Experimental Model.....	3
1.4 Overview of the Dissertation.....	3
Chapter 2	4
Heat transfer in hypersonic flow	4
2.1 Chapter Overview.....	4
2.2 A “Definition” of Hypersonic Flow	4
2.2.1 Thin shock layers	5
2.2.2 Entropy layer.....	5
2.2.3 Viscous interactions and high temperature flows	6
2.3 Shock Wave-Boundary Layer Interactions	7
2.4 Convective Aerodynamic Heating	9
2.5 Axial Corner Flow.....	10
2.6 Hypersonic Heat Transfer Measurements	13
2.6.1 Surface junction thermocouples.....	14
2.6.2 Infrared thermography	14

2.7	Heat Transfer Measurements in Hypersonic Flow Studies	16
2.8	Chapter Summary	18
Chapter 3		19
Swept oblique shocks and heat transfer		19
3.1	Chapter Overview	19
3.2	Predicting Flow Conditions and Local Heat Flux	20
3.2.1	Experimental model geometry	20
3.2.2	Upstream flow conditions	21
3.2.3	Downstream flow conditions using Oblique Shock Wave with Sweep....	23
3.2.4	Aerodynamic heating	28
3.3	Semi-infinite Slab Data Reduction Model	31
3.4	Chapter Summary	33
Chapter 4		34
Experimental Methods		34
4.1	Chapter Overview	34
4.2	Test Facility and Experimental Model	34
4.2.1	Test Facility	34
4.2.2	Initial flow conditions for facility operation	35
4.2.3	Experimental Model	35
4.3	Instrumentation and Setup	38
4.3.1	Type K surface junction thermocouples	38
4.3.2	Thermocouple location	39

4.3.3	AD595-AQ Thermocouple amplifier	40
4.3.4	Piezoelectric pressure transducer	40
4.3.5	Data acquisition.....	40
4.3.6	Onca-MWIR-MCT-640 infrared camera	42
4.3.7	Calibration of the infrared camera	43
4.4	Chapter Summary	45
Chapter 5	46
Results	46
5.1	Chapter Overview.....	46
5.2	Run 280	46
5.2.1	Stagnation conditions	46
5.2.2	Surface temperature	48
5.3	Run 285	49
5.3.1	Stagnation conditions	49
5.3.2	Surface temperature	50
5.4	Infrared Camera Calibration Curves	50
5.5	Chapter Summary	52
Chapter 6	53
Analysis and Discussion	53
6.1	Chapter Overview.....	53
6.2	Comparison of Analytical and Empirical Values of Local Heat Flux.....	54
6.3	Calibration of Infrared Camera	55

6.3.1	In situ calibration.....	55
6.3.2	Derivation of temporal information from Run 285 video.....	56
6.3.3	Comparisons of recorded surface temperature history with calibrated temperature values	57
6.4	Identifying Peak Heating Regions and the Axial Corner Flow Phenomena	62
6.4.1	Inspection of calibrated temperature curve	63
6.4.2	Surface heat flux mapping	64
6.4.3	Identification of boundary layer separation and reattachment.....	66
6.5	Uncertainty in Measurements.....	68
6.6	Chapter Summary.....	68
	Chapter 7.....	69
	Conclusions and Further Work	69
7.1	Brief Review of Dissertation.....	69
7.2	Conclusions	70
7.3	Further Work	71
7.4	Closing.....	71
	Appendix A.....	A.1
	Project Specification	A.1
	Appendix B	B.1
	Oblique Shock Wave with Sweep.....	B.1
	Introduction	B.2
	Nomenclature	B.2

Assumptions and Methodology	B.2
Appendix C	C.1
Analytical Calculations for Run 280.....	C.1
Introduction.....	C.2
Upstream Flow Conditions	C.2
C.1.1 Stagnation conditions	C.2
Downstream Flow Conditions.....	C.5
C.1.2 Assumptions.....	C.5
C.1.3 Mach number, flow deflection angle, and shock wave angle in the sweep plane	C.5
Summary of Flow Conditions	C.11
Aerodynamic Heating	C.11
Appendix D.....	D.1
Analytical Calculations for Run 285.....	D.1
Introduction.....	D.2
Upstream Flow Conditions	D.2
D.1.1 Stagnation conditions	D.2
Downstream Flow Conditions.....	D.5
D.1.2 Assumptions.....	D.5
D.1.3 Mach number, flow deflection angle and shock wave angle in the sweep plane	D.5
Summary of Flow Conditions	D.9
Aerodynamic Heating	D.10

Appendix E	E.1
MATLAB Code	E.1
Analytical Calculations for Run 280.....	E.2
Analytical Calculations for Run 285.....	E.6
Impulse Response Function Based on Semi-Infinite Wall Model (Oldfield 2000)	E.10
Stagnation Pressure and Temperature Plotting for Run 280.....	E.13
Stagnation Pressure and Temperature Plotting for Run 285.....	E.15
Calibration Sequences.....	E.17
Comparison of Calibrated and Recorded Plots	E.19
Heat Flux Mapping	E.22

List of Figures

Figure 1.1: Double swept-wedge model	2
Figure 1.2: Damage to the X-15 as a result of shock-wave impingement, right (a), front (b), and left (c) views (Armstrong 2014)	2
Figure 1.3: Rectangular to Elliptical Transition (REST) model with notched cowl (Smart 1999)	3
Figure 2.1: Physical effects characteristic of hypersonic flow (Anderson 2006)	5
Figure 2.2: Thin shock layer (Anderson 2006)	5
Figure 2.3: Entropy layer (Anderson 2006)	6
Figure 2.4: Temperature profile in a hypersonic boundary layer (Anderson 2006)	7
Figure 2.5: Shock interactions categorised by Edney (Albertson & Venkat 2005)	8
Figure 2.6: Schematic of the shock-wave boundary-layer interaction (Anderson 2006) ..	9
Figure 2.7: Axial corner flow configuration (Panaras 1996)	11
Figure 2.8 Corner flowfields on a supersonic flight vehicle (Hummel 1989)	11
Figure 2.9: Corner flow flowfield structure proposed by Charwat and Redekopp (1967)	12
Figure 2.10: (a) Model geometry (b) Flow pattern (Gounko and Mazhul 2013).....	13
Figure 2.11: Approximate locations of the surface junction thermocouples (Smart 2001)	17
Figure 3.1: Experimental model for analysis	20
Figure 3.2: Schematic of oblique shock wave with sweep theory (Emanuel 1992)	23

Figure 3.3 Flow pattern at Mach 6 with flow direction indicated by the red arrow (Gounko and Mazhul 2013)	29
Figure 3.4: Semi-infinite substrate heat transfer gauge (Oldfield 2000)	32
Figure 4.1: Scale drawing of the facility in the Ludwig Tube mode (Buttsworth 2010)	35
Figure 4.2: Photograph of the experimental model mounted in the test section of TUSQ	36
Figure 4.3: Plan and elevation views of the experimental model	36
Figure 4.4: Plan and elevation views of Type K thermocouple (Omega Engineering Inc. 2014)	38
Figure 4.5: Location of functioning thermocouple for experiments	39
Figure 4.6: AD595AQ Thermocouple amplifier	40
Figure 4.7: Schematic of TUSQ showing relative positions of transducer and diaphragm (Widodo 2012)	40
Figure 4.8: (A) Edwards ADC controller, (B) Druck DPI-260 pressure indicator, (C) NI-PXIe-1082 platform and (D) NI-PXIe-8108 embedded controller	41
Figure 4.9: NI-BNC-2110 connector	41
Figure 4.10: Overall view of the data acquisition system	42
Figure 4.11: IR camera positioned above horizontally mounted experimental model ...	43
Figure 4.12: Tunnel test section closed, with IR camera focused on experimental model through Calcium Fluoride optical access window	43
Figure 4.13: Heat gun positioned in open test section for IR camera calibration	44
Figure 5.1: Stagnation pressure in nozzle reservoir region	47
Figure 5.2: Stagnation temperature derived from pressure measurements in nozzle reservoir region	47

Figure 5.3: Surface temperature recorded by thermocouple (Run 280).....	48
Figure 5.4: Surface temperature recorded by thermocouple during flow (Run 280).....	48
Figure 5.5: Stagnation pressure in nozzle reservoir region.....	49
Figure 5.6: Stagnation temperature derived from pressure measurements in nozzle reservoir region	49
Figure 5.7: Surface temperature recorded by thermocouple during flow for Run 285...	50
Figure 5.8: Sequence 1 calibration curve.....	51
Figure 5.9: Sequence 2 calibration curve.....	51
Figure 5.10: Sequence 3 calibration curve.....	52
Figure 6.1: Surface heat flux on model during test flow (Run 280)	55
Figure 6.2: Surface heat flux on model during test flow (Run 285)	55
Figure 6.3: Recorded temperature curve and calibrated temperature curve using Sequence 1	57
Figure 6.4: Recorded temperature curve and calibrated temperature curve using Sequence 2	58
Figure 6.5: Recorded temperature curve and calibrated temperature curve using Sequence 3	58
Figure 6.6: Filtered surface temperature history at Thermocouple 2 (Run 285)	60
Figure 6.7: Thermograph of model approximately 75°C (flow direction indicated with red arrow).....	61
Figure 6.8: Calibrated surface temperature history for pixel range (331:340, 81:90)	62
Figure 6.9: Calibrated surface temperature history for pixel range (343:345, 86:88)	62
Figure 6.10: Calibrated surface temperature at thermocouple junction (a) Time (b) Number of frames	63

Figure 6.11: Surface heat flux maps of Frame 166 and Frame 168 for Run 285.....	64
Figure 6.12: Filled contour heat flux maps of Frame 166 to Frame 174 for Run 285....	65
Figure 6.13: Streamwise locations on model to plot calibrated temperature and surface temperature histories	67
Figure 6.14: Temperature histories in streamwise direction for Locations (1), (2), and (3).....	67
Figure 7.1: Close-up of measurements taken by piezoelectric pressure transducer in nozzle reservoir region.....	C.2
Figure 7.2: Stagnation temperature in the nozzle reservoir section during flow (Run 280)	C.3
Figure 7.3 Flow pattern at Mach 6 with flow direction indicated by the red arrow (Gounko and Mazhul 2013)	C.13
Figure 7.4: Close-up of measurements taken by piezoelectric pressure transducer in nozzle reservoir region during Run 285.....	D.2
Figure 7.5: Stagnation temperature in nozzle reservoir during Run 285	D.3

Nomenclature

Symbol	Definition	Units
a	Speed of sound	$\frac{m}{s}$
θ	Flow deflection angle	$^{\circ}$
δ	Boundary layer thickness	m
Λ	Sweep angle	$^{\circ}$
β	Shock wave angle	$^{\circ}$
c_p	Specific heat capacity at constant pressure	$\frac{J}{kg \cdot K}$
h	Enthalpy	$\frac{J}{kg}$
\dot{q}	Heat flux	$\frac{W}{m^2}$
T	Temperature	$^{\circ}$ or K
p	Pressure	Pa
μ	Viscosity	$\frac{kg}{m \cdot s}$
ρ	Density	$\frac{kg}{m^3}$
k	Thermal conductivity	$\frac{W}{m \cdot K}$
t	Time	s
u	Velocity	$\frac{m}{s}$
R	Specific gas constant	$\frac{J}{kg \cdot K}$
γ	Ratio of specific heats	
M	Mach number	
Pr	Prandtl number	
C_H or St	Stanton number	
Re	Reynolds number	
Subscripts		
0	At stagnation conditions	

1	Upstream
2	Downstream
aw	Adiabatic wall
e	Boundary layer edge
∞	Freestream
w	At the wall i.e. model surface
ref	Reference
amb	Ambient
atm	Atmospheric

Abbreviations

ADC	Active digital controller
fps	Frames per second
IR	Infrared
IRT	Infrared thermography
MWIR	Mid-wave infrared
NI	National Instruments
PCB	Printed circuit board
PMMA	Polymethyl Methacrylate
TUSQ	The University of Southern Queensland Hypersonic Wind Tunnel
VKI	Von Karman Institute

Chapter 1

Prepare for Takeoff

For some years I have been afflicted with the belief that flight is possible to man. The disease has increased in severity and I feel it will soon cost me an increased amount of money, if not my life.

— Wilbur Wright, beginning of his first letter to Octave Chanute, 13 May 1900

A significant date in aeronautical history is 24 February 1949. This marks the day when the V2/WAC Corporal Rocket became the first object of human origin to successfully achieve hypersonic flight. Hypersonic flow will be more clearly defined in Chapter 2, but for now, a nominal speed of Mach 5 (or five times the speed of sound) will define and signify the start of the hypersonic flight envelope.

Welcome aboard a ‘flight’ into the world of hypersonics.

1.1 Introduction

The design process of an aircraft generally begins with defining its mission. This step dictates aspects such as geometry, materials, and the flight environment. For hypersonic aircraft, three main types of missions have been identified (NASA 2014), namely (a) re-entry from orbit, (b) air-breathing accelerator, and (c) air-breathing cruiser. The vehicle speeds vary, from about Mach 5 for cruising to Mach 25 for re-entry from orbit.

The purpose of this experimental research project is to quantify the effects of aerodynamic heating over the double swept-wedge configuration at Mach 6 (Figure 1.1). More specifically, it aims to investigate the use of infrared thermography to identify and quantify regions of peak aerodynamic heating.

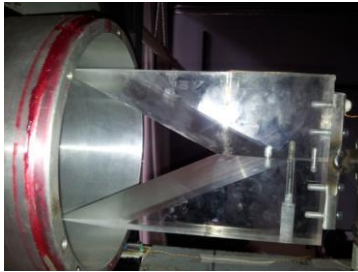


Figure 1.1: Double swept-wedge model

Experiments for this project were conducted at the University of Southern Queensland Hypersonic Wind Tunnel (TUSQ). With a pressure in the test section of approximately 700Pa, a flow speed of Mach 6, and the model geometry, the tests were designed to simulate the air flow over part of the intake of a hypersonic aircraft flying at Mach 6 at an altitude of 30km.

1.2 Convective Aerodynamic Heating

Travelling through the atmosphere at hypersonic speeds involves various critical problems such as aerodynamic heating. Although this phenomenon and its causes will be described in Chapter 3, the purpose of this section is to illustrate the detrimental effects of severe aerodynamic heating. The next illustration (Figure 1.2) is of the considerable structural damage to the X-15 experimental aircraft during a test flight at Mach 6.7. The damage was caused by multiple shock wave/boundary layer interactions that led to intense aerodynamic heating.

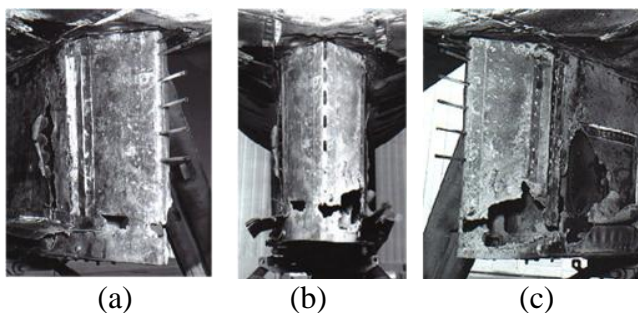


Figure 1.2: Damage to the X-15 as a result of shock-wave impingement, right (a), front (b), and left (c) views (Armstrong 2014)

1.3 Practical Significance of Experimental Model

The double swept-wedge configuration can be found on scramjet inlet designs such as the Rectangular-to-Elliptical Shape Transition (REST) model by Dr Michael Smart, as depicted in Figure 1.3. Although a simplification of the notched cowl closure region of the inlet, the author predicts that the locations of peak heating due to convective aerodynamic heating will be similar.



Figure 1.3: Rectangular to Elliptical Transition (REST) model with notched cowl (Smart 1999)

1.4 Overview of the Dissertation

Essential theory relevant to the present study will be presented in Chapter 2. Chapter 3 will present theoretical predictions of post-shock flow conditions. Chapter 4 discusses the experimental methods, including the test facility and instrumentation (surface junction thermocouples and thermal infrared camera). The experimental results will be presented in Chapter 5 with the analysis and discussion provided in Chapter 6. Conclusions will be discussed and further work will be described in Chapter 7.

The author hopes that this sojourn into the world of hypersonics will be an enjoyable one, in which the reader will gain some insight into the complexities of the flowfield over a double swept-wedge configuration and the importance of considering the effects of aerodynamic heating in hypersonic vehicle design.

The ‘flight’ is ready and it is time for takeoff.

Chapter 2

Heat transfer in hypersonic flow

2.1 Chapter Overview

Background knowledge and studies relevant to the present work are covered in this chapter.

The chapter will open with a definition of hypersonic flow, followed by introductions to shock wave-boundary layer interactions and convective aerodynamic heating.

Studies in axial corner flow and the use of surface junction thermocouples and infrared thermography in hypersonic flow studies will then be discussed.

2.2 A “Definition” of Hypersonic Flow

A generally accepted value for the lower limit of the hypersonic envelope is Mach 5 (Anderson 2006). The physical effects that differentiate hypersonic from supersonic flow include thin shock layers, entropy layers, high temperatures, and viscous interactions (Figure 2.1). Combined, these constitute a “definition” of hypersonic flow (Anderson 2006).

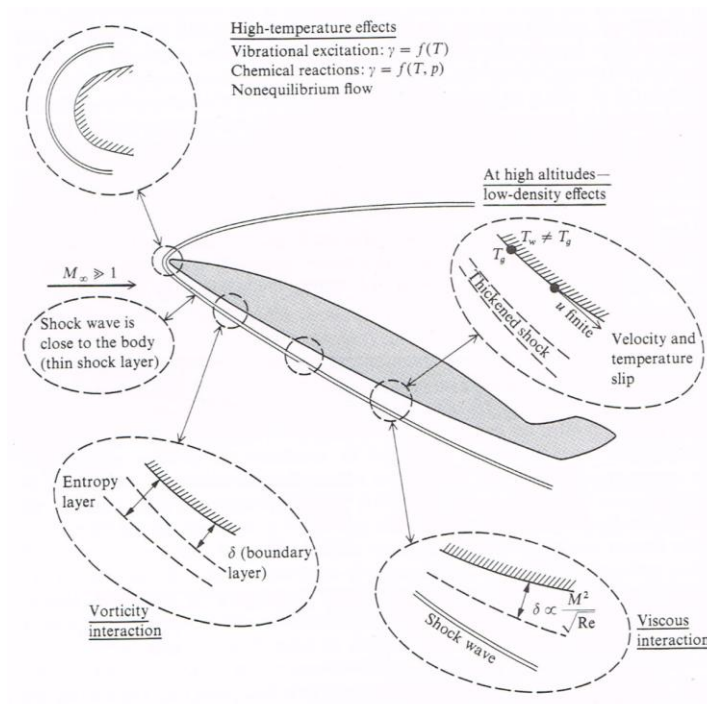


Figure 2.1: Physical effects characteristic of hypersonic flow (Anderson 2006)

2.2.1 Thin shock layers

The shock layer is the flowfield region between the shock wave and the surface of an object (Figure 2.2). This layer becomes thinner as the Mach number increases because. This causes the shock wave angle (in Figure 2.2, $\beta = 18^\circ$) to approach the flow deflection or wedge angle ($\theta = 15^\circ$). As the shock layer becomes thinner, it begins to merge with the rapidly growing boundary layer. This creates the problem of a fully viscous shock layer, which leads to increased skin-friction drag.



Figure 2.2: Thin shock layer (Anderson 2006)

2.2.2 Entropy layer

The entropy through a shock wave is influenced by the shock wave strength (Figure 2.3). The entropy gradients are generally stronger at the leading edge of an object. Therefore, for a blunt object, as shown in Figure 2.3, the entropy gradient is stronger

due to the normal portion of the bow shock wave. The rapidly growing boundary layer along the surface also interacts with this entropy layer. Since the entropy layer is a region of high vorticity, the interaction between the two layers is known as a vorticity interaction (Anderson 2006).

However, this layer is not as influential for the experimental model in the current work as the leading edges of the model are sharp.

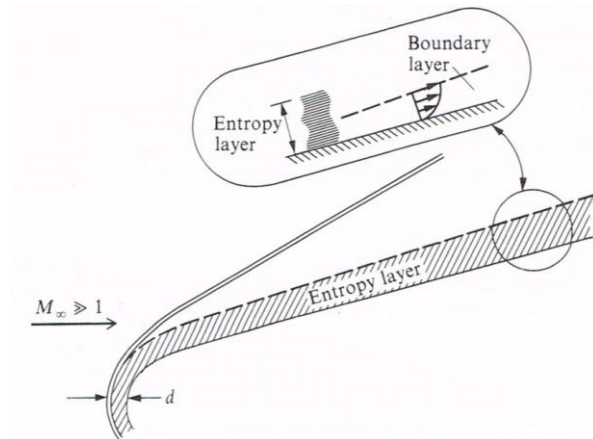


Figure 2.3: Entropy layer (Anderson 2006)

2.2.3 Viscous interactions and high temperature flows

The two main types of viscous interactions that occur in a hypersonic flow are firstly, between the rapidly growing (viscous) boundary layer and the outer (inviscid) flow, and secondly, when a shock wave impinges the boundary layer.

The first type is normally labelled a viscous interaction, and will be described in this section. The second type of interaction is called a shock wave-boundary layer interaction and will be described in the next section.

A viscous interaction is a pressure interaction between the hypersonic boundary layer and outer inviscid flow. In a process known as viscous dissipation, the fast moving gas particles in the inviscid flow dissipate some of their kinetic energy to the slower moving particles in the boundary layer. These particles respond to this energy transfer by increasing their internal energy, consequently observed as a rise in temperature.

An adiabatic wall concept says that heat transfer to the wall is negligible. For this wall boundary condition, the high temperature seen at the surface is due to heating by

viscous dissipation and the temperature rise in the fluid from the conversion of kinetic energy into internal energy.

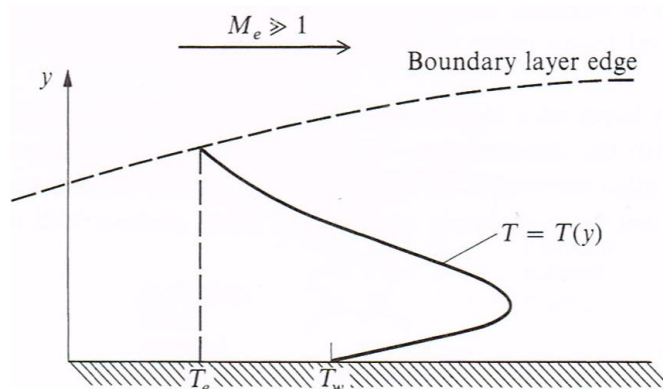


Figure 2.4: Temperature profile in a hypersonic boundary layer (Anderson 2006)

Extreme temperatures are generated in the boundary layer at very high Mach numbers, such as those seen in planetary re-entry vehicles. For instance, Apollo 11 re-entered the Earth's atmosphere at Mach 36. At this speed, temperatures in excess of 10,000K are reached. This results in the gas molecules dissociating and/or ionising, making the boundary layer chemically reactive. For this type of flow, the real gas assumption is more relevant than the ideal gas assumption.

2.3 Shock Wave-Boundary Layer Interactions

In a high-speed flow, a shock wave can interact with another shock wave or immediately with the boundary layer over the surface of an object.

In the late 1960s, Edney categorised six patterns of shock- interactions that have been investigated by numerous researchers including Albertson and Venkat (2005). The leading edge schematic (Figure 2.5) shows the interaction patterns between an oblique shock wave and the leading edge bow shock. A detailed treatment of these interactions is outside the scope of the current study, as the purpose in this instance is to simply bring these types of interactions to the reader's awareness and illustrate the complex interactions that can occur in high-speed flow.

Three of the interaction types (I, II, and V) result in shock wave-boundary layer interactions. They are the second type of viscous interaction between the boundary layer and outer flow and will now be briefly described.

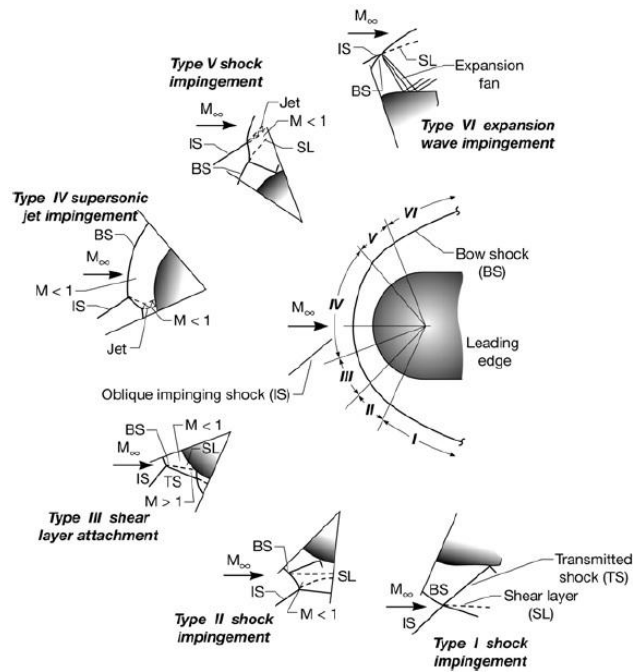


Figure 2.5: Shock interactions categorised by Edney (Albertson & Venkat 2005)

Shock wave-boundary layer interactions are characterised by a number of phenomena (Anderson 2006), namely

- (i) an incident shock
- (ii) an induced separation shock
- (iii) a reattachment shock
- (iv) an embedded expansion wave, and
- (v) a separated flow region

As evidenced by the example given in Chapter 1 of the X-15 experimental aircraft, shock wave-boundary layer interactions can cause severe aerodynamic heating that will result in extensive structural damage. Understanding these interactions can help flight vehicle designers to identify measures that would prevent or control the effects aerodynamic heating.

A schematic of a two-dimensional shock wave-boundary layer interaction is depicted in Figure 2.6.

When a shock wave impinges the boundary layer, it causes a large pressure rise across the boundary layer. Furthermore, this also imposes a severe adverse pressure gradient on the boundary, leading to local boundary separation and the formation of a “separation bubble”.

The presence of this bubble further disrupts the flow, leading to the formation of a second shock wave: the induced separation shock.

The separated boundary layer turns back towards the plate, and eventually reattaches to the surface. When it does, the third shock wave (reattachment shock) is generated.

The boundary layer is thinner, further downstream of the separation activity. Therefore, when the separated boundary layer reattaches, it encounters the thinner boundary layer, and because the pressure is still high, then the viscous interaction is high and so are the effects of aerodynamic heating.

Further away from the plate, the separation and reattachment shocks merge to form the conventional reflected shock wave.

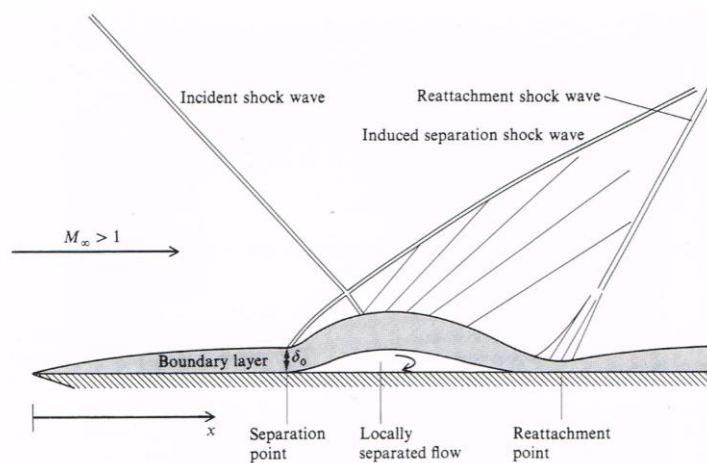


Figure 2.6: Schematic of the shock-wave boundary-layer interaction (Anderson 2006)

The scale and severity of the interaction depends on whether the boundary layer is laminar or turbulent. Laminar boundary layers separate more readily than turbulent boundary layers, so aerodynamic heating is more severe for laminar than turbulent interactions (Anderson 2006).

2.4 Convective Aerodynamic Heating

The transfer of heat from a gas to the body surface is known as aerodynamic heating. The two types of heating, radiative and convective are driven by different sources. Irrespective of the hypersonic flight speed, aerodynamic heating is significant, such that it determines the configuration design of most hypersonic vehicles.

Convective aerodynamic heating is the dominant form of heating at Mach 6, and will be the focus of this section. The driving source in convective aerodynamic heating is the temperature gradient of the gas at the solid surface and its governing equation is:

$$q_w = \rho_e u_e C_H (h_{aw} - h_w) \quad (2.1)$$

Determining the wall boundary conditions is important in viscous flows. One of the unknowns in a high-speed flow problem is usually the wall (surface) temperature. The heat transfer to the wall by conduction can be estimated using Fourier's Law of Heat Conduction:

$$q_w = -k \left(\frac{\partial T}{\partial n} \right)_w \quad (2.2)$$

The thermal conductivity of the gas at the wall is denoted by k and $(\partial T / \partial n)_w$ is the normal temperature gradient existing in the gas immediately at the wall. Heat is being conducted in the opposite direction of the temperature gradient and is indicated by the minus sign.

The adiabatic wall concept is a special case of the heat-transfer wall boundary condition, where there is negligible heat transfer to the wall. This condition applies to the temperature gradient, and not on the wall temperature itself.

$$\left(\frac{\partial T}{\partial n} \right)_w = 0 \quad (2.3)$$

2.5 Axial Corner Flow

Panaras (1996) discussed four basic configurations that can occur at different locations on a hypersonic aircraft: (a) Fin/plate configuration, (b) Swept compression corner, (c) Wedge/plate configuration, and (d) Axial corner or wedge/wedge configuration. Of the four configurations, the axial corner is the most relevant to the present study.

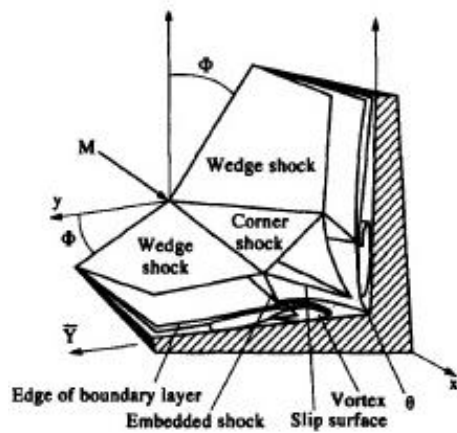


Figure 2.7: Axial corner flow configuration (Panaras 1996)

The axial corner configuration is formed by two wedges and can be found in high speed intakes (Figure 2.8). The flow over the configuration is initially compressed by two swept and planar oblique shock waves attached to the leading edges of the wedges. These waves interact with each other in the corner region to form a corner shock wave and also interact with the boundary layer to create a complex system of interactions.

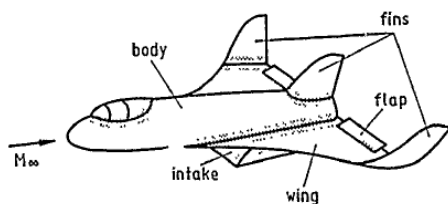


Figure 2.8 Corner flowfields on a supersonic flight vehicle (Hummel 1989)

Geometry dictates flowfield symmetry. Thus, if the sweep and wedge angles are the same, then the flowfield is symmetric. The supersonic or hypersonic flows about these geometries are also characterised by the appearance of straight separation lines on the surfaces, and peak heating and pressure near the corner. If the interactions are strong enough, then reattachment lines are also observed.

Aside from the flow conditions, the strength of the interaction depends on the wedge, sweep and corner angles, the geometry (fin, wedge, swept or unswept) and on the boundary layer (turbulent or laminar).

Charwat and Redekopp (1967) performed the first systematic study on swept shock/boundary layer interactions for supersonic laminar flow over two intersecting wedges. In their experiments, they took surface pressure measurements and pitot

pressure surveys and also used oil to visualise the flow over the model. From their analysis, Charwat and Redekopp proposed the flowfield model illustrated in Figure 2.9. The flowfield model is characterised by transmitted and reflected shocks and interactions with the boundary layer. A detailed discussion of these shock waves, the conical nature of the flow, and the local boundary layer separation and reattachment activity in this region, are beyond the scope of the present study.

Since the pioneering work of Charwat and Redekopp, other experimental and numerical studies have been conducted by researchers such as Cresci et al. (1969), Watson and Weinstein (1970), Korkegi (1971), and the Braunschweig Research Group at the Technical University of Braunschweig (1975 – 1989). All studies confirmed the same basic flowfield model for two intersecting wedges, albeit with slight variations to flow conditions and geometry. Moreover, the basic flowfield model applies irrespective of the speed (supersonic or hypersonic) or flow regime (laminar or turbulent).

As noted by Korkegi (1971 p.778): ‘The corner heat-transfer distribution has distinct features in common with two-dimensional shock wave laminar boundary-layer interaction – a drop in heat-transfer rates beyond separation (the trough) followed by a rise to high values (peaks) at reattachment.’ These studies showed that the heat transfer rate measurements followed a similar pattern exhibited by the surface pressure readings.

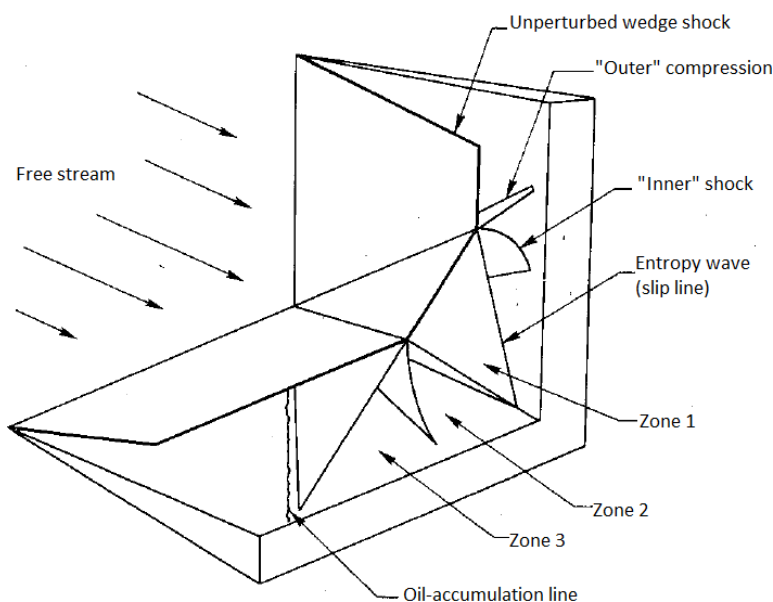


Figure 2.9: Corner flow flowfield structure proposed by Charwat and Redekopp (1967)

Another notable study in axial corner flow was a numerical investigation into supersonic and hypersonic flow over a double swept wedge model by Gounko and Mazhul (2013). As shown in Figure 2.10 (a), their model geometry is very similar to the current experimental model, except for the presence of the pre-compression ramp (A'B'CBA). One of the most relevant aspects of their work in the context of the current study is the flow pattern produced from their simulation, depicted in Figure 2.10 (b).

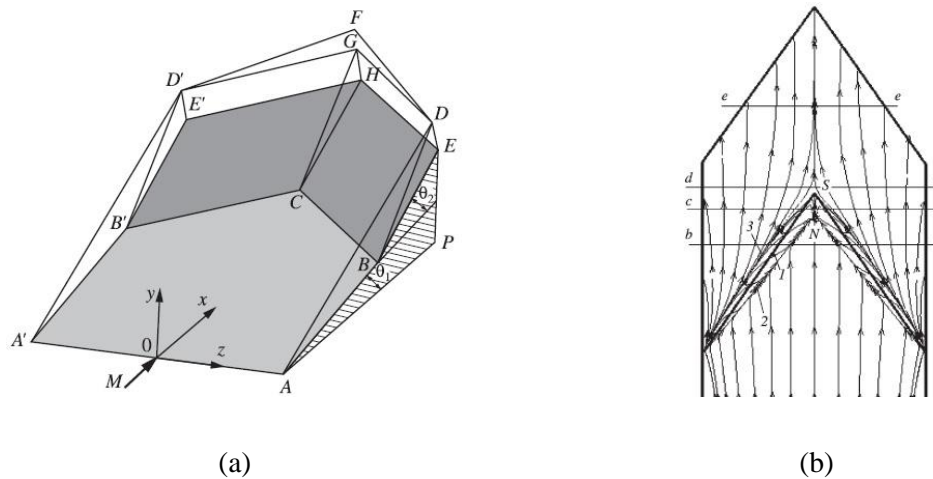


Figure 2.10: (a) Model geometry (b) Flow pattern (Gounko and Mazhul 2013)

This flow pattern allowed this author to estimate the distance x required in determining the local Reynolds number as part of the aerodynamic heating equation.

Although not performed in the present study, it would be beneficial to visualise the flow over the model (using oil, for instance) to compare against the flow pattern simulated by Gounko and Mazhul. Moreover, numerically simulating the flow over the current model and comparing it to the above flow pattern would be beneficial. The pattern will of course be a slight variation to that illustrated above because no pre-compression ramp is used. Nonetheless, the numerical simulation would be helpful in gaining an understanding of the flow pattern and possibly an insight into the conical nature of the flow in the corner region, should the current study be extended in the future.

2.6 Hypersonic Heat Transfer Measurements

Transient temperature measurements can be taken in hypersonic flow with discrete-point gauges such as surface junction thermocouples and spatial heat information can be

achieved using infrared thermography. With these measurement tools, one can derive heat transfer rates and identify critical areas on the test model affected by peak heating.

2.6.1 Surface junction thermocouples

Surface junction thermocouples operate on the Seebeck effect (McGee 1988). The current work is not an investigation into the theoretical aspects or calibration of thermocouples. Moreover, since the theory and operation of thermocouples are well understood, the reader is simply referred to the studies of Roache (2004) and Widodo (2009) or the book by McGee (1988) for excellent descriptions on the principles of thermocouples. Thermocouples were used in the current experiments for surface temperature measurements and as part of the in-situ calibration of the infrared camera. A discussion pertaining to their use in the in-situ calibration is provided below.

2.6.2 Infrared thermography

Infrared thermography is a non-intrusive thermal mapping technique, whose operation is based on Planck's Law of Radiation. It comprises a camera equipped with a series of optics, an infrared detector and a computer. The detector is a transducer that absorbs infrared energy emitted by an object (whose surface temperature is to be measured), and converts this information into an electrical current or voltage. The information is then converted into a digital format that is read by a computer to produce a two-dimensional image (a thermogram or thermal image).

This technology has been used in a variety of applications, including hypersonic flow studies (Henckels & Maurer 1989). It can be used to provide a quick full field surface temperature distribution on wind tunnel models over complex geometries, which aid in locating and understanding critical areas that may be excessively heated (Simeonides et al. 1993).

2.6.2.1 Advantages and disadvantages

Cardone and Carlomagno (1998) listed some of the advantages of infrared thermography including the fact that it is non-intrusive, provides good spatial heat information, and the equipment can have good thermal sensitivity.

One major limitation with infrared thermography is that a unique temperature range over the model must be chosen for each test. Therefore, in order to avoid saturation of

the signal in regions of high heating, higher noise-to-signal ratios must be tolerated in lower heating regions (Simeonides et al. 1993). The problem can be alleviated either by making two tests with different temperature ranges or reducing data at two different times from the effective beginning of the test (Simeonides et al. 1993).

2.6.2.2 In situ calibration of infrared thermography with thermocouples

Calibrating the infrared camera is an important first step and can be performed in-situ using discrete-point gauges such as thermocouples. It is one of the most accurate means of calibrating the camera and provides a quick and accurate method of doing so (Simeonides et al. 1993).

In situ calibration with thermocouples can be achieved either by changing the temperature of the object transiently while monitoring the detector optical signal by taking readings of several thermocouples placed in different temperature regions.

The transient technique was used in this study and was first applied by Thomann and Frisk in 1968 (Schulz et al. 2009).

In this type of calibration, surface temperature data is collected simultaneously from two sources: discrete-point sensors, e.g. thermocouples, attached to the model surface to measure local temperatures and an infrared camera to capture thermograms (thermal images) of the surface. The aim here is to simultaneously collect temperature data from two sources and correlate their data to yield a one-to-one relation between changes in surface temperature and changes in the intensity measured.

The wind tunnel model may serve as the calibration surface and can be heated by a high power source such as a 1kW photographic lamp or heat gun. The simultaneous measurements are then taken during the transient cooling of the model surface after the heat source is switched off.

Correlating temperature and the detected radiation is challenging, and is partly to do with purity of the object signal. The signal is not only attenuated by optical viewing windows, but is also affected by extraneous emissions close to the model. These sources include the emission of the gas and reflections of hot surrounding walls or objects.

A second or third order polynomial relationship between the two sources is then derived, where temperature is a function of gray scale value. With the calibration

polynomial, the recorded digitised data, location maps of thermocouple positions and surface temperature distributions over the entire test surfaces are determined from spatially resolved distributions of gray scale values recorded with the infrared camera.

The polynomial allows other information to be determined, such as the magnitudes of spatially resolved convective heat transfer coefficients, Nusselt numbers, or surface effectiveness values.

2.6.2.3 Accuracy of measurements during calibrations

The accuracy of a thermocouple reading depends upon factors such as its calibration curve, its exact position in the model surface and its orientation with respect to temperature gradients (Schulz et al. 2009). It also depends on identifying the correct pixels on the thermogram as part of determining the calibration polynomial (Lafferty and Collier 1991).

According to Schulz et al. (2009), thermocouples placed in regions of high temperature and heat flux gradients often cannot be used for the calibration because they significantly decrease the overall accuracy of the calibration.

Lafferty and Collier (1991) found differences and scatter between their two measurement sets using thermocouples and an infrared camera. They identified possible sources of error including the inability to find the exact location of the thermocouples in the infrared image. They concluded that the exact location of the thermocouple in the thermogram is necessary to compare the two measurements.

2.7 Heat Transfer Measurements in Hypersonic Flow Studies

Thermocouples have been used in numerous hypersonic flow studies (Buttsworth and Widodo 2010; Smart 2001; Roache 2004).

Smart (2001) used type E coaxial thermocouples to monitor the temperature of the Rectangular to Elliptical Transition (REST) hypersonic inlet (Figure 2.11) and also to obtain an estimate of the heat transfer to the model. The focus of this study was to validate the use of the design methodology of fixed geometry inlets suitable for airframe integrated scramjets, rather than identify and quantify the regions of peak aerodynamic heating.

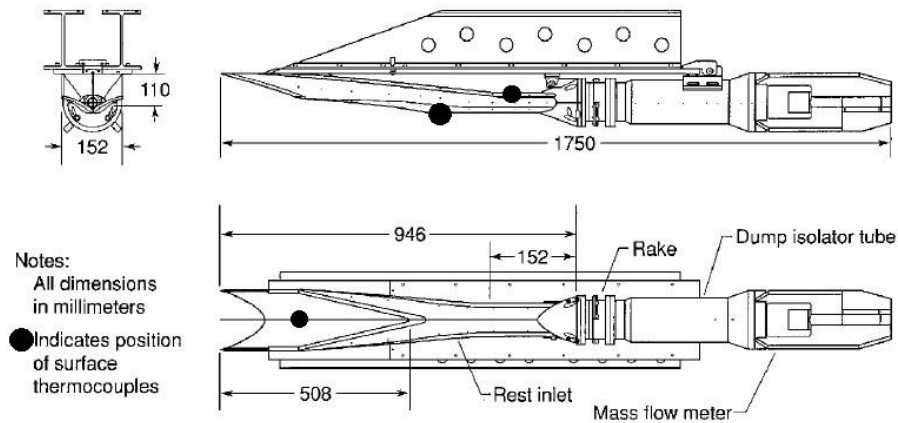


Figure 2.11: Approximate locations of the surface junction thermocouples (Smart 2001)

Infrared thermography has been applied in hypersonic flow studies as well. Henckels and Maurer (1989) investigated its use for the measurements of the surface temperature distribution on models exposed to a hypersonic flow. The method was shown to be a powerful tool to obtain a quick survey of the surface temperature distribution on wind tunnel models. They also focused part of their efforts in quantifying heat flux on some of their models, such as the swept-wing plate (Henckel & Maurer 1989). As will be discussed in a later chapter, these investigators plotted the heat flux histories to quantify the effects due to aerodynamic heating, which is very relevant to the present study.

Simeonides et al. (1993) used infrared thermography at the H-3 Mach 6 blowdown wind tunnel of the Von Karman Institute (VKI). There, they emphasised applying infrared thermography to simplified configurations that simulated components of hypersonic lifting re-entry vehicles exhibiting shock wave-boundary layer interactions. One of those configurations was the axial corner, which is the type of configuration under investigation in the present study. In their research, they developed heat transfer distribution plots and temperature contour plots over a variety of geometries. They demonstrated the high efficiency and accuracy of this technique, in terms of temperature, temporal and spatial resolution, making it comparable to discrete point gauges. Furthermore, due to the success of an earlier related study, infrared thermography became the prime kinetic heating measurement technique in the VKI Mach 6 blowdown tunnel.

At the time of writing, the author has not identified previous studies where detailed heat flux contour maps were produced.

2.8 Chapter Summary

An introduction to hypersonic flow theory opened this chapter. Additionally, shock wave boundary layer interactions and convective aerodynamic heating were discussed

The chapter then introduced the axial corner flow configuration, which is the most relevant configuration to the present experimental model. Accompanying that was a review of relevant studies. The chapter closed with the topic of hypersonic heat transfer measurements, the instrumentation used in heat transfer measurements in hypersonic flow studies, and relevant studies in this area.

In the next chapter, the analytical tools used to provide theoretical predictions of local heat transfer rates on the experimental model will be presented.

Chapter 3

Swept oblique shocks and heat transfer

3.1 Chapter Overview

In this chapter, the analytical tools used to estimate the flow conditions in the vicinity of the swept oblique shock waves, as well as the local heat flux into the experimental model will be introduced. The data reduction model used to convert the recorded temperature data into heat flux values will also be described.

More specifically, the flow conditions immediately upstream of the shock will be determined with the isentropic relations for an ideal gas and the ideal gas equation (Fox et al. 2010). The downstream flow conditions will be estimated with a modified form of the oblique shock wave theory by Emanuel (1992) that accounts for a sweep angle. Finally, the aerodynamic heating equation, as presented in Anderson (2006), will provide an estimate of the local heat flux on the experimental model. Representative flow conditions will be applied to the governing equations to demonstrate these methods.

The chapter will close with a description of the MATLAB functions by Oldfield (2000). These functions are based on the semi-infinite slab data reduction model, which was used to convert the transient temperature data into corresponding heat flux values.

3.2 Predicting Flow Conditions and Local Heat Flux

The analysis will be divided into three main areas:

- (1) Flow conditions immediately upstream of the shock
- (2) Flow conditions immediately downstream of the shock
- (3) Heat flux due to convective aerodynamic heating

This methodology will be illustrated by analysing the experimental model under a set of representative flow conditions. The equations and the results only will be accompanied by a short explanation. The derivation of the method and its application to predict the flow conditions for the current experiments, are presented in the appendices.

3.2.1 Experimental model geometry

The experimental model is depicted in Figure 3.1 and the angles of interest for the proceeding analysis are listed in Table 3.1.

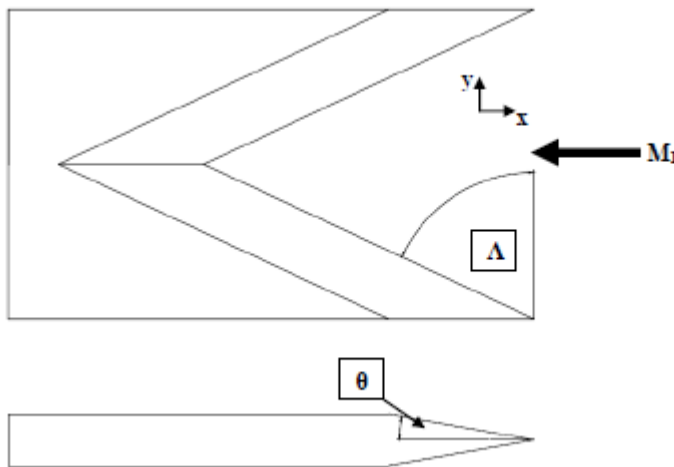


Figure 3.1: Experimental model for analysis

Table 3.1: Wedge geometry

Property	Symbol	Value
Wedge angle in x-y plane	θ	10°
Sweep angle	Λ	65°

3.2.2 Upstream flow conditions

The test gas is compressed slowly at TUSQ, so the process can be considered isentropic. Therefore, the isentropic gas relations (Fox et al. 2010 p.599) can be used in this instance to determine the flow conditions immediately upstream of the shock wave. Furthermore, the test gas (air) is assumed to be ideal, with a specific heat ratio, $\gamma = 1.4$. Therefore, the ideal gas equation (3.4) can also be used in this analysis.

Table 3.2: Local isentropic stagnation properties for an ideal gas (Fox et al. 2010)

Ratio	Formula	
Pressure	$\frac{p_0}{p_1} = \left(1 + \frac{\gamma - 1}{2} M_1^2\right)^{\frac{\gamma}{\gamma - 1}}$	(3.1)
Density	$\frac{\rho_0}{\rho_1} = \left(1 + \frac{\gamma - 1}{2} M_1^2\right)^{\frac{1}{\gamma - 1}}$	(3.2)
Temperature	$\frac{T_0}{T_1} = 1 + \frac{\gamma - 1}{2} M_1^2$	(3.3)

$$p = \rho RT \quad (3.4)$$

Two of the known values for the current study are the stagnation pressure (in the nozzle reservoir region as measured by the piezoelectric transducer) and the stagnation temperature. The stagnation temperature is derived from the stagnation pressure value using an ideal gas isentropic relation (3.5). Another known value will be the measured surface (wall) temperature on the experimental model (T_w).

$$\frac{T_0}{T} = \left(\frac{p_0}{p}\right)^{\frac{\gamma - 1}{\gamma}} \quad (3.5)$$

$$\therefore T_0 = T_{amb} \left[\left(\frac{p_0}{p_{amb}}\right)^{\frac{\gamma - 1}{\gamma}} \right] \quad (3.6)$$

The representative flow conditions that will be used to demonstrate the analytical methods are presented in Table 3.3.

Table 3.3: Representative upstream flow conditions

Property	Symbol	Value
Mach number	M_1	5.85
Stagnation temperature	T_0	565K
Stagnation pressure	p_0	980kPa
Ratio of specific heats	γ	1.4

Using Equation (3.1), the upstream pressure is given by:

$$p_1 = \frac{p_0}{\left(1 + \frac{\gamma - 1}{2} M_1^2\right)^{\frac{\gamma}{\gamma - 1}}} \quad \therefore p_1 = 724.9 \text{ Pa}$$

The upstream temperature is given by Equation (3.3).

$$T_1 = \frac{T_0}{\left(1 + \frac{\gamma - 1}{2} M_1^2\right)} \quad \therefore T_1 = 72.03 \text{ K}$$

Finally, the upstream density is determined by rearranging the ideal gas equation (3.4).

$$\rho_1 = \frac{p_1}{RT_1} \quad \therefore \rho_1 = 0.0351 \frac{\text{kg}}{\text{m}^3}$$

The upstream flow conditions will now be used in the following analysis to determine the flow conditions immediately downstream of the oblique shock wave.

3.2.3 Downstream flow conditions using Oblique Shock Wave with Sweep

Oblique attached shock waves with sweep are a relatively common occurrence in high speed aerodynamics (Emanuel 1992). In practical terms, an oblique shock wave is a three-dimensional phenomenon, but the local flow conditions immediately downstream of the shock can be determined using a two-dimensional approach (Anderson 1990). The reason for this approach is simplicity, as the analysis of a three-dimensional wave is time and computationally intensive.

The oblique shock relations that are commonly found in undergraduate textbooks in fluid mechanics do not account for sweep angles. Therefore, a modification of these relations is required to analyse the flow conditions over the double swept-wedge experimental model. The author identified a method by Emanuel (1992) that analyses an oblique shock wave with sweep. A schematic of the model and the coordinate system used, are depicted in Figure 3.2.

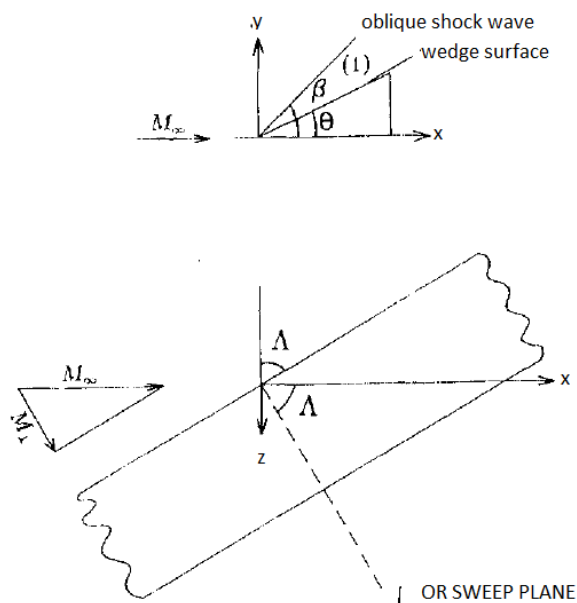


Figure 3.2: Schematic of oblique shock wave with sweep theory (Emanuel 1992)

This method focuses on the fluid dynamics due to the sweep. Simplifying assumptions include a planar, inviscid and uniform flow with the shock wave attached to the leading edge of the wedge.

Nomenclature used in the analysis

As depicted in Figure 3.2 and earlier in Figure 3.1, a cartesian coordinate system is used, where x is aligned with the flow direction and y and z lay in planes perpendicular to the flow direction.

In the x, y plane, the upper wedge surface and planar shock have angles θ and β , respectively. The leading edge of the wedge has a sweep angle of Λ . A plane that is perpendicular to the leading edge is called the sweep plane and is denoted with a \perp subscript. Downstream of the attached shock, the flow is denoted with a subscript of 2.

Mach number, flow deflection angle and shock wave angle in the sweep plane

The derivation of this method is quite comprehensive. Therefore, in this section, only the equations from this method and the results using the representative flow conditions will be presented. Additional assumptions and the derivation of this method are presented in Appendix B.

$$M_{\perp} = M_{\infty} \cos \Lambda \quad \therefore M_{\perp} = 2.472$$

$$\theta_{\perp} = \tan^{-1} \left(\frac{\tan \theta}{\cos \Lambda} \right) \quad \therefore \theta_{\perp} = 22.65$$

$$\beta_{\perp} = \tan^{-1} \left\{ \frac{M_{\perp}^2 - 1 + 2\lambda \cos[(4\pi\delta + \cos^{-1} \chi)/3]}{3 \left(1 + \frac{\gamma-1}{2} M_{\perp}^2 \right) \tan \theta_{\perp}} \right\} \quad (3.7)$$

where

$$\lambda = \left[(M_{\perp}^2 - 1) - 3 \left(1 + \frac{\gamma-1}{2} M_{\perp}^2 \right) \left(1 + \frac{\gamma+1}{2} M_{\perp}^2 \right) \tan^2 \theta_{\perp} \right]^{\frac{1}{2}} \quad \therefore \lambda = 4.057$$

$$\chi = \frac{1}{\lambda^3} \left[(M_{\perp}^2 - 1)^3 - 9 \left(1 + \frac{\gamma-1}{2} M_{\perp}^2 \right) \right. \\ \left. \times \left(1 + \frac{\gamma-1}{2} M_{\perp}^2 + \frac{\gamma+1}{4} M_{\perp}^4 \right) \tan^2 \theta_{\perp} \right] \quad \therefore \chi = 0.7160$$

Substituting known values into (3.7) gives

$$\therefore \beta_{\perp} = 46.96^{\circ}$$

The shock wave angle in the x-y plane and the normal component of the Mach number in the sweep plane are

$$\beta = \tan^{-1}(\cos \Lambda \tan \beta_{\perp}) \quad \therefore \beta = 24.35^{\circ}$$

$$M_{\perp n} = M_{\perp} \sin \beta_{\perp} \quad \therefore M_{\perp n} = 1.807$$

The upstream sonic speed is given by

$$a_1 = \sqrt{\gamma RT_1} \quad \therefore a_1 = 170.1 \frac{m}{s}$$

The velocity components immediately downstream of the shock wave can be determined from the following relation

$$\begin{aligned} \mathbf{w}_2 = a_1 \left\{ \left[M_1 - \frac{2}{\gamma + 1} \frac{M_{\perp n}^2 - 1}{M_{\perp n} \sqrt{(\csc^2 \beta + \tan^2 \Lambda)}} \right] \hat{\mathbf{t}}_x \right. \\ \left. + \frac{2}{\gamma + 1} \frac{M_{\perp n}^2 - 1}{M_{\perp n} \sqrt{(\csc^2 \beta + \tan^2 \Lambda)}} \times (\cot \beta \hat{\mathbf{t}}_y + \tan \Lambda \hat{\mathbf{t}}_z) \right\} \end{aligned} \quad (3.8)$$

The velocity components along the three orthogonal directions are

$$u_{2x} = a_1 \left(M_1 - \frac{2}{\gamma + 1} \frac{M_{\perp n}^2 - 1}{M_{\perp n} \sqrt{(\csc^2 \beta + \tan^2 \Lambda)}} \right) \quad \therefore u_{2x} = 940.3 \frac{m}{s}$$

$$u_{2y} = a_1 \left(\frac{2}{\gamma + 1} \frac{\cot \beta (M_{\perp n}^2 - 1)}{M_{\perp n} \sqrt{(\csc^2 \beta + \tan^2 \Lambda)}} \right) \quad \therefore u_{2y} = 121.3 \frac{m}{s}$$

$$u_{2z} = a_1 \left(\frac{2}{\gamma + 1} \frac{\tan \Lambda (M_{\perp n}^2 - 1)}{M_{\perp n} \sqrt{(\csc^2 \beta + \tan^2 \Lambda)}} \right) \quad \therefore u_{2z} = 117.7 \frac{m}{s}$$

The magnitude of the downstream velocity is therefore

$$u_2 = \sqrt{u_{2x}^2 + u_{2y}^2 + u_{2z}^2} \quad \therefore u_2 = 955.4 \frac{m}{s}$$

The oblique shock relations (Fox et al. 2010 pp.670-671) will now be used to determine the other flow properties downstream of the shock, namely pressure, temperature and density.

$$\text{Pressure ratio} \quad \frac{p_2}{p_1} = \frac{2\gamma}{\gamma+1} M_{\perp n}^2 - \frac{\gamma-1}{\gamma+1} \quad \therefore \frac{p_2}{p_1} = 3.643$$

$$\text{Density ratio} \quad \frac{\rho_2}{\rho_1} = \frac{\left(\frac{\gamma+1}{2}\right) M_{\perp n}^2}{1 + \left(\frac{\gamma-1}{2}\right) M_{\perp n}^2} \quad \therefore \frac{\rho_2}{\rho_1} = 2.370$$

$$\text{Temperature ratio} \quad \frac{T_2}{T_1} = \frac{\left(1 + \left[\frac{\gamma-1}{2}\right] M_{\perp n}^2\right) \left(\gamma M_{\perp n}^2 - \left[\frac{\gamma-1}{2}\right]\right)}{\left(\frac{\gamma+1}{2}\right)^2 M_{\perp n}^2} \quad \therefore \frac{T_2}{T_1} = 1.537$$

Finally, the flow conditions immediately downstream of the oblique shock wave can be calculated.

$$\text{Density} \quad \rho_2 = \rho_1 \times 2.37 \quad \therefore \rho_2 = 0.0831 \frac{kg}{m^3}$$

$$\text{Temperature} \quad T_2 = T_1 \times 1.537 \quad \therefore T_2 = 110.7K$$

$$\text{Pressure} \quad p_2 = p_1 \times 3.643 \quad \therefore p_2 = 2640Pa$$

The local speed of sound downstream of the shock

$$a_2 = \sqrt{\gamma R T_2} \quad \therefore a_2 = 210.9 \frac{m}{s}$$

Downstream Mach number

$$M_2 = \frac{u_2}{a_2} \quad \therefore M_2 = 4.53$$

Listed in Table 3.4 is a summary of the flow conditions determined from the foregoing analysis.

Table 3.4: Summary of flow conditions

Property	Upstream	Downstream
Pressure	724.9Pa	2640Pa
Temperature	72.03K	110.7K
Density	$0.0351 \frac{kg}{m^3}$	$0.0831 \frac{kg}{m^3}$
Flow velocity	$995.2 \frac{m}{s}$	$955.4 \frac{m}{s}$
Local speed of sound	$170.1 \frac{m}{s}$	$210.9 \frac{m}{s}$
Mach number	5.85	4.53

The downstream absolute viscosity coefficient can be calculated from Sutherland's Law (Anderson 2006 p.292). This law is accurate for air over a range of several thousand degrees and is certainly appropriate for the current calculations.

$$\frac{\mu}{\mu_{ref}} = \left(\frac{T}{T_{ref}} \right)^{\frac{3}{2}} \frac{T_{ref} + S}{T + S}$$

For air, the reference values are

$$T_{ref} = 288K$$

$$\mu_{ref} = 1.789 \times 10^{-5} \frac{kg}{ms}$$

$$S = 110K$$

$$T = T_2 = 110.7K$$

The viscosity coefficient immediately through the shock wave is therefore

$$\mu_2 = \mu_{ref} \left[\left(\frac{T}{T_{ref}} \right)^{\frac{3}{2}} \left(\frac{T_{ref} + S}{T + S} \right) \right] \quad \therefore \mu_2 = 7.687 \times 10^{-6} \frac{kg}{ms}$$

3.2.4 Aerodynamic heating

As noted by Anderson (2006), the “driving potential” for aerodynamic heating to the surface is the enthalpy difference, $(h_{aw} - h_w)$. The governing equation of aerodynamic heating is

$$q_w = \rho_e u_e C_H (h_{aw} - h_w) \quad (3.9)$$

Since the analysis is based on an inviscid flow, then the flow conditions determined in the previous section are the boundary layer edge flow conditions in (3.9).

$$\rho_e = \rho_2 = 0.0831 \frac{kg}{m^3}$$

$$u_e = u_2 = 955.4 \frac{m}{s}$$

$$T_e = T_2 = 110.7K$$

$$\mu_e = \mu_2 = 7.687 \times 10^{-6} \frac{kg}{ms}$$

The wall temperature is the peak value measured with the surface junction thermocouple during the test flow:

$$T_w = 301K$$

The wall to boundary layer edge temperature ratio is therefore

$$\frac{T_w}{T_e} = \frac{301}{110.7} = 2.72$$

In order to calculate the flat-plate Stanton number, the wall to boundary layer edge temperature ratio and the ordinate in Figure 6.12 in Anderson (2006 pp. 297) need to be located and determined i.e. $C_H\sqrt{Re_x}$.

$$C_H\sqrt{Re_x} = 0.34$$

The next step is to calculate the local Reynolds number(Re_x), which involves estimating the distance from the leading edge of the wedge to the thermocouple junction (x). This distance is measured by following a streamline to the thermocouple junction (indicated by a red dot in Figure 3.3), and finding the sum of the straight-line segments of this path.

For simplicity, the author identified a numerical study that used a geometric model similar to the experimental model in the present study. Although this model uses a pre-compression ramp, the flow pattern of the current experimental model is still likely to be a variation of this pattern, and therefore can be used to estimate the distance from the leading edge, x .

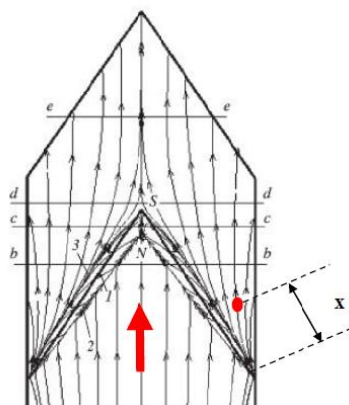


Figure 3.3 Flow pattern at Mach 6 with flow direction indicated by the red arrow (Gounko and Mazhul 2013)

Using this method, the distance is

$$x = 40 \times 10^{-3}m$$

The local Reynolds number is therefore

$$Re_x = \frac{\rho_e u_e x}{\mu_e} = 4.132 \times 10^5$$

Finally, the Stanton Number (C_H) is given by

$$C_H = \frac{C_H \sqrt{Re_x}}{\sqrt{Re_x}} = 5.290 \times 10^{-4}$$

The recovery factor (r) accounts for the viscous dissipation of the high kinetic energy through the viscous boundary layer. Its formula for laminar flow is presented in Table 3.5. Also presented in this table are the various enthalpy quantities involved in the formulation of the aerodynamic heating equation. A comprehensive treatment of these quantities and their corresponding equations as applied to the current study is presented in the appendices, namely Appendix B, Appendix C, and Appendix D.

Table 3.5: Important quantities for the aerodynamic heating equation

Quantity	Formula	Value
Specific heat capacity at constant pressure	$c_p = \frac{7R}{2}$	$\therefore c_p = 1004.5 \frac{J}{kgK}$
Prandtl number for laminar flow	$r = \sqrt{Pr}$	0.846
Boundary-layer edge enthalpy	$h_e = c_p T_e$	$\therefore h_e = 1.112 \times 10^5 \frac{J}{kg}$
Total (stagnation) enthalpy	$h_0 = h_e + \frac{u_e^2}{2}$	$\therefore h_0 = 5.675 \times 10^5 \frac{J}{kg}$
Adiabatic wall enthalpy	$h_{aw} = h_e + r(h_0 - h_e)$	$\therefore h_{aw} = 4.971 \times 10^5 \frac{J}{kg}$
Wall enthalpy	$h_w = c_p T_w$	$\therefore h_w = 3.024 \times 10^5 \frac{J}{kg}$

Finally, the local heat flux can be determined using Equation (3.9).

$$\therefore q_w = 8178 \frac{W}{m^2} = 8.18 \frac{kW}{m^2}$$

3.3 Semi-infinite Slab Data Reduction Model

The semi-infinite slab data reduction model will be used to convert the measured surface temperature values into heat transfer rates.

The technique has been used in numerous hypersonic flow studies (Henckels 1989; Simeonides et al.. 1993) and assumes that the heat transfer rate into the surface of the model is computed from the time variation of its surface temperature. The model is assumed to be sufficiently thick, so that its back surface temperature remains unaffected by the heating of the front surface. Discrete-point gauges like surface junction thermocouples are embedded in the front surface and surface temperature measurements

are taken. Additionally, steady, one-dimensional heat conduction is assumed in this model for simplicity.

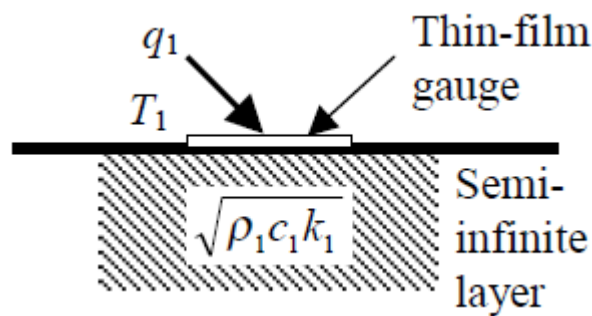


Figure 3.4: Semi-infinite substrate heat transfer gauge (Oldfield 2000)

Oldfield (2000) wrote a suite of MATLAB functions that process digitised temperature signals transient gauges such as surface junction thermocouples on a variety of substrates that includes a semi-infinite substrate.

The functions are based on the impulse response technique and are used in conjunction with the MATLAB Signal Processing Toolbox function `fftfilt`.

The premise of the impulse response method is that the response of any linear time invariant (LTI) system such as a surface junction thermocouple (with surface temperature $T(t)$ and surface heat transfer rate $q(t)$), can be calculated from the impulse response $h(t)$ of that system by a convolution integral.

The details of this integral and the impulse response method are presented in the guide produced by Oldfield (2000).

The impulse response function used in this study is:

```
[h, shift] = desT2qsiimp1 (fs,np,rrck,test)
```

This function designs (`des`) a filter to convert the measured surface temperature T to heat transfer rate q (`T2q`) for a semi-infinite substrate (`si`) and gives an impulse response (`imp`), h .

The `filter` function used in the design process will not work if the first term of $q_1[n]$ is zero. Therefore, the flag, `shift`, is required to move the $q_1[n]$ sequence one place to the left.

fs = sampling frequency (Hz)

np = number of sampling points

rrck = thermal product of the substrate¹

test =

The measured temperature (T) is then converted to heat flux (q) with the following function:

q = fftfilt(h, T)

3.4 Chapter Summary

In this chapter, the analytical tools used in this study to predict the flow conditions immediately downstream of the oblique shock waves and the local heat flux values were introduced and an illustrative example presented. In addition, the semi-infinite data reduction model was described, which was used to convert the transient temperature data into heat flux values.

The next chapter will cover the experimental equipment and methods used in this study.

¹ Thermal product, $TP = \sqrt{\rho ck}$, where ρ is the density (kg/m^3), c = specific heat capacity ($\text{Jkg}^{-1}\text{K}^{-1}\text{s}^{-0.5}$), and k = thermal conductivity ($\text{Wm}^{-1}\text{K}^{-1}$) of the substrate.

Chapter 4

Experimental Methods

4.1 Chapter Overview

The experimental setup and methods for the current study will be covered in this chapter. It will begin with brief descriptions of the test facility and experimental model. The focus will then shift to descriptions of the instrumentation used in the experiments and the main setup parameters. The chapter will close with a description of the infrared camera and the in-situ calibration procedure.

4.2 Test Facility and Experimental Model

4.2.1 Test Facility

The test facility for the current experiments is the University of Southern Queensland Hypersonic Wind Tunnel (TUSQ). It is a long-duration (up to 200ms) Ludwieg Tube facility that can physically simulate supersonic and hypersonic flows and operates in one of two modes: atmospheric pressure blow-down or Ludwieg tunnel, with or without free piston compression heating.

In the current work, the facility was operated as a Ludwieg tunnel, with a Mach 6 contoured nozzle that produces a nominal flow of Mach 5.85 (Ennis 2013). A detailed description of the nozzle and facility operation is provided in the paper by Buttsworth (2010).

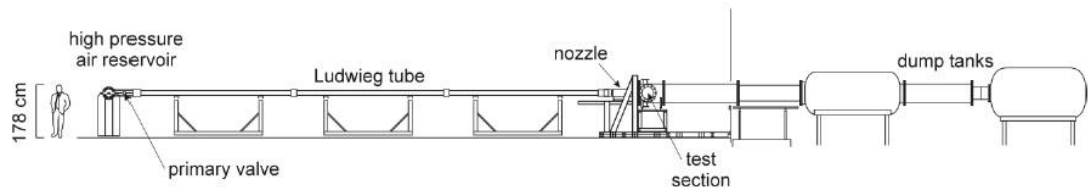


Figure 4.1: Scale drawing of the facility in the Ludwieg Tube mode (Buttsworth 2010)

4.2.2 Initial flow conditions for facility operation

The initial flow conditions for the two experimental runs are presented in Table 4.1.

Table 4.1: Initial conditions for facility operation

Property	Value	
	Run 280	Run 285
$p_{reservoir}$	3MPa	
p_{amb}	94.17kPa	94.94kPa
T_{amb}	288.7K	292K

This information was recorded with a thermometer and barometer in the TUSQ facility and the piezoelectric pressure transducer described earlier. The tunnel was operated in accordance with the TUSQ operating procedure and manual (Malpress & Buttsworth 2013) and experiments were carried out under the supervision of qualified personnel. A description of the standard operating procedures of the TUSQ is outside the scope of the present study.

4.2.3 Experimental Model

Figure 4.2 shows a photograph of the experimental model mounted in the TUSQ test section. It was mounted on the sting with four equidistant M10 bolts, at a depth of approximately 25mm. It comprises two symmetrical and adjacent wedges with sharp swept leading edges and sweep and wedge angles of 65° and 10° , respectively (Figure 4.3).



Figure 4.2: Photograph of the experimental model mounted in the test section of TUSQ

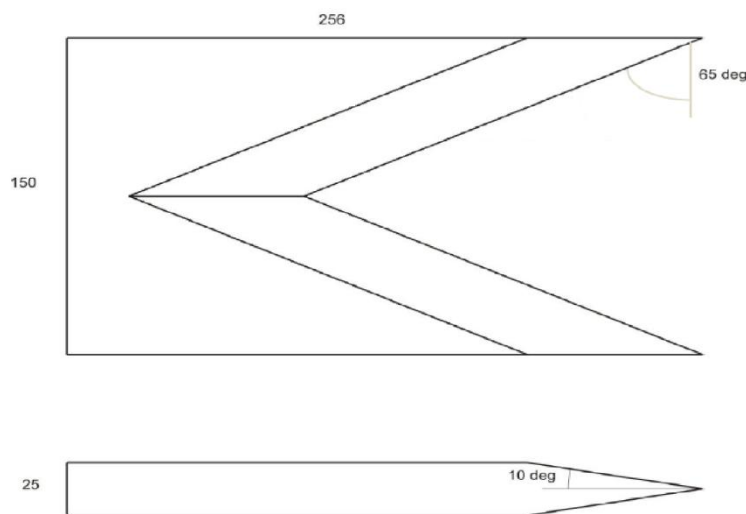


Figure 4.3: Plan and elevation views of the experimental model

The model was manufactured from Perspex (Polymethyl methacrylate), whose thermal properties are listed in Table 4.2. At the time of writing, the exact reason for the use of Perspex as the model material is unknown to the author. Hence, relevant literature was reviewed to identify possible reasons.

Henckels and Maurer (1989) investigated the applications of infrared thermography in hypersonic flow studies. Here, they used Perspex as the model material and said: ‘For the applied measurement technique of heat transfer values, it is necessary that the amount of heat conduction inside the model wall is sufficiently small compared to the heat load caused by the flow’ (Henckels & Maurer 1989, p.517). Therefore, it was important to have a material with a low thermal diffusivity, such as Perspex. With a low thermal diffusivity, this meant that heat penetrated only through thin layers of the model

surface. Moreover, this allowed the assumption of a semi-infinite wall during the test runs.

The data reduction model in the current work is the semi-infinite slab model. Therefore, this author concludes that the rationale provided by Henckels and Maurer (1989) in selecting Perspex as the model material, is the mostly likely reason for the selection of the same material in the current experiments².

Table 4.2: Thermal properties of Perspex (Productive Plastics 2014)

Property	Symbol	Value
Density	ρ	$1190 \frac{kg}{m^3}$
Thermal conductivity	k	$0.189 \frac{W}{mK}$
Specific heat capacity at constant pressure	c_p	$1465.4 \frac{J}{kgK}$

An important quantity in transient temperature measurements is thermal product (Buttsworth 2001). It is used to derive heat flux from surface temperature measurements and is expressed as,

$$TP = \sqrt{\rho k c_p} \quad (4.1)$$

Using the values listed in Table 4.2, the thermal product for the experimental model is:

$$TP = 574.1 \frac{J}{m^2 K \sqrt{s}}$$

² A better idea would have been for the author to ask his supervisor. However, doing so would've taken the joy out of learning something new.

4.3 Instrumentation and Setup

Heat flux is derived from transient surface temperature data using an appropriate reduction model. In the current work, the surface temperature measurements were recorded with surface junction thermocouples and spatial heat information was captured using infrared thermography.

4.3.1 Type K surface junction thermocouples

A Type K Chromega®-Alomega® thermocouple (CO2-K) was used in the current experiments (Figure 4.4).

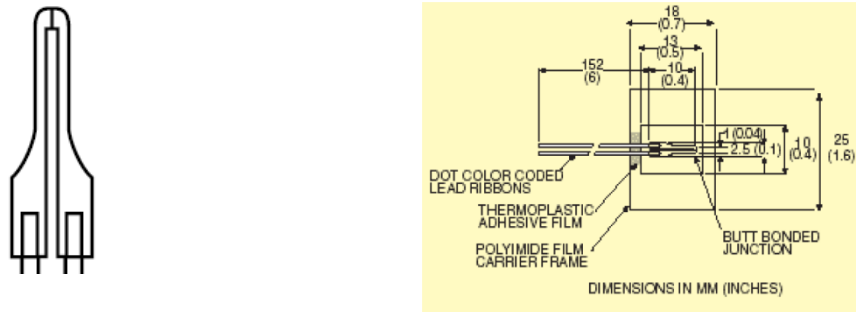


Figure 4.4: Plan and elevation views of Type K thermocouple (Omega Engineering Inc. 2014)

Technical specifications of the thermocouple are provided in Table 4.3. The Style 2 thermocouple is flat, with a very low thermal inertia, which makes it ideal for situations when a very fast response is desired (Omega Engineering Inc. 2014). Hence, this thermocouple is well suited for hypersonic flow studies, where the flow durations are very short and transient measurements are required.

Table 4.3: Technical specifications of the CO2-K Thermocouple (Omega Engineering Inc. 2014)

Quantity	Value
Length	150mm
Maximum temperature (Continuous)	540°C
Maximum temperature (600hr)	540°C
Maximum temperature (10hr)	650°C
Response time when “grounded” or “cemented” to surface	2ms – 5ms
Thickness of butt-welded thermocouple junction	0.013mm
Thermal sensitivity	100mV/°C

4.3.2 Thermocouple location



Figure 4.5: Location of functioning thermocouple for experiments

The thermocouples were bonded to the model surface with Cyanoacrylate (Super Glue™). One thermocouple (with the junction indicated by a red oval in Figure 4.5) was used in Run 280, and two more were subsequently bonded to the model for Run 285. Unfortunately, the additional thermocouples malfunctioned. However, the first thermocouple still functioned and surface temperature histories were recorded for both experimental runs.

4.3.3 AD595-AQ Thermocouple amplifier

An AD595-AQ (9943) monolithic thermocouple amplifier (with cold junction compensation) amplified the output signal from the surface junction thermocouple. A technical data sheet of this device is available in the references (Digi-key Corporation 2014).



Figure 4.6: AD595AQ Thermocouple amplifier

4.3.4 Piezoelectric pressure transducer

Pressure measurements for the experiment were recorded with a PCB piezoelectric (charge mode) pressure transducer. The output signal was amplified with a Kistler charge amplifier. The transducer was positioned approximately 130mm upstream of the 100 μ m Mylar diaphragm (Figure 4.7).

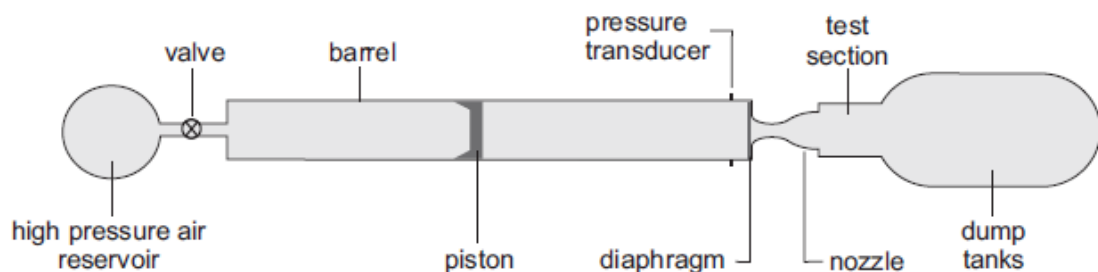


Figure 4.7: Schematic of TUSQ showing relative positions of transducer and diaphragm (Widodo 2012)

4.3.5 Data acquisition

The analog output signals from the pressure and temperature transducers were converted to digital form by a National Instruments PXI-6123 multifunction data acquisition system (DAQ). The information was stored in a text file using the National Instruments software, NI-DAQmx, and processed by the author using MATLAB.

The data acquisition system comprised the following components

- NI-PXIe-1082 platform
- NI-PXIe-8108 embedded controller
- NI-BNC-2110; shielded connector block with BNC for X series and M series
- Edwards ADC (Active Digital Controller) single gauge controller
- Druck DPI-260 pressure indicator

Photographs of the equipment are shown in Figure 4.8, Figure 4.9, and Figure 4.10. Further details of the data acquisition equipment are available from the manufacturers' websites listed in the references.

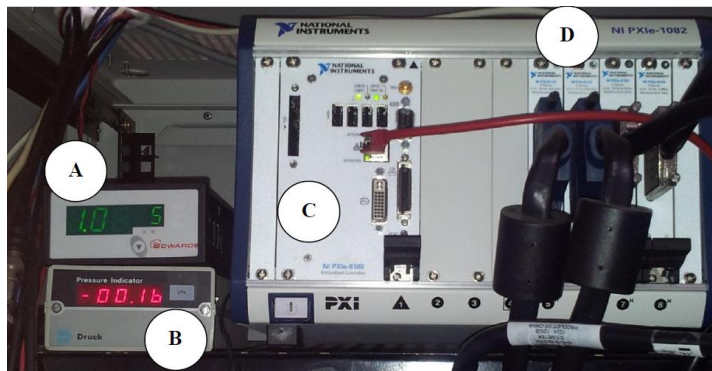


Figure 4.8: (A) Edwards ADC controller, (B) Druck DPI-260 pressure indicator, (C) NI-PXIe-1082 platform and (D) NI-PXIe-8108 embedded controller



Figure 4.9: NI-BNC-2110 connector



Figure 4.10: Overall view of the data acquisition system

4.3.6 Onca-MWIR-MCT-640 infrared camera

The Onca-MWIR-MCT-640 infrared camera was used to capture spatial heat information about the experimental model. It is a mid-wave infrared camera with a two-dimensional Mercury-Cadmium Telluride (MCT) focal plane array.

According to the manufacturer (Ishchenko, D 2014, pers. comm., 23 October) the camera operates in a similar fashion to a digital photograph camera and captures images during an integration time determined by the operator. The optical signal is read and converted into a digital form, which is sent to the computer either by an Ethernet or Camera-link interface. The camera outputs a digital signal of 14-bit, at a maximum frame rate of approximately 100Hz. The images have a maximum resolution of 640 x 512 pixels. The images are displayed on the computer using Xeneth, a graphical user interface (GUI) that allows for easy control of the camera parameters and acquisition of images.

For the current experiments, the model was mounted horizontally, and the camera positioned approximately 1500mm directly above the model (Figure 4.11). The optical access window is made of Calcium Fluoride, which has a high transmissivity (Figure 4.12). The camera was set with an integration time of $2000\mu\text{s}$ and an image resolution of 512 x 400 pixels. A video of Run 285 was recorded at 111 fps (frames per second).

In addition, 200 individual thermograms were captured by the author. The video and the thermograms will be discussed in further detail in Chapter 6.

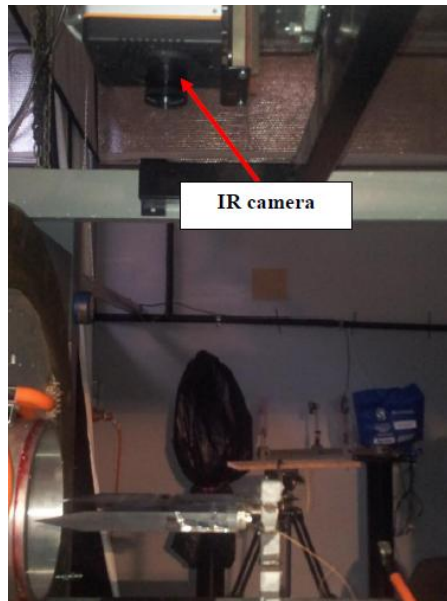


Figure 4.11: IR camera positioned above horizontally mounted experimental model



Figure 4.12: Tunnel test section closed, with IR camera focused on experimental model through Calcium Fluoride optical access window

4.3.7 Calibration of the infrared camera

4.3.7.1 In situ calibration

In-situ calibration of infrared thermography systems was described in Chapter 2. The same procedure was used in the current experiments, where the calibration procedure was performed in the (closed) test section of the tunnel. The experimental model acted as the calibration surface, and a Type K surface junction thermocouple and the camera

simultaneously recorded the temperature information as the model was being heated by a heat gun. Three sets of calibrations were performed and the results are presented in the next chapter and analysed in detail in Chapter 6.

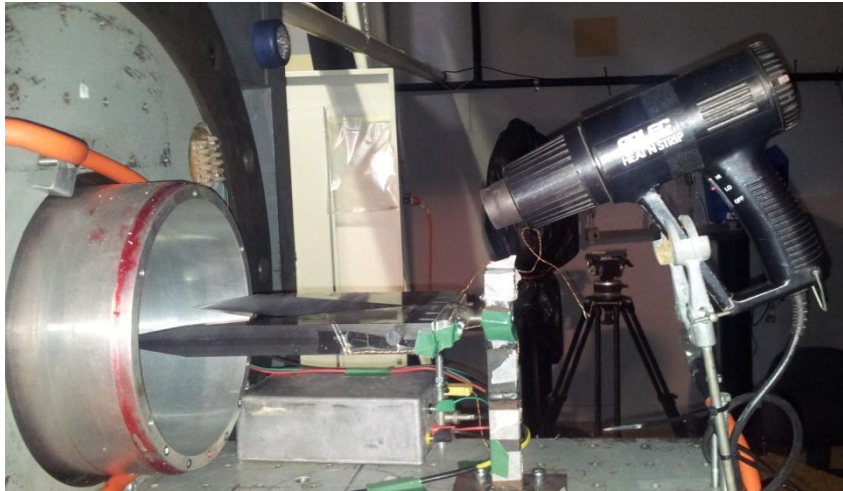


Figure 4.13: Heat gun positioned in open test section for IR camera calibration

4.3.7.2 Calibration curves

Post-processing of the thermal information from the calibration process was achieved using MATLAB. The information from the camera (the number of photons detected) and the thermocouple (the surface temperature) were correlated and the MATLAB `polyfit` and `polyval` functions were used to generate polynomial coefficients and consequently calibration curves.

In order to identify the best calibration curve, it was necessary to inspect the thermograms to discern the correct pixels for the thermocouple junction. Once identified, each calibration curve was applied to these pixels to generate calibrated surface temperature history curves. The calibrated curves were then compared against the surface temperature history recorded by the Type K surface junction thermocouple and the best fit was selected. Results of this process are presented and discussed in Chapter 6.

4.3.7.3 Surface heat flux mapping

The best calibration curve was then used to create calibrated surface temperature curves for particular areas of the model, namely those identified from the recorded video that exhibited peak heating. The calibrated temperature information was converted into heat

flux values using the impulse response functions by Oldfield (2000); these were introduced in the previous chapter. Finally, heat flux contour maps were created to quantify the effects due to convective aerodynamic heating on the model from the nominal Mach flow.

4.4 Chapter Summary

The experimental equipment and methods applied in the present study were described in this chapter. More specifically, the reader was introduced to the test facility, TUSQ, the instrumentation and experimental procedures that included in-situ calibration of the infrared camera.

In the next two chapters, the reader will be presented with the results of experiments Run 280 and Run 285 (Chapter 5) and a discussion and analysis of those results (Chapter 6).

Chapter 5

Results

5.1 Chapter Overview

Plots of the recorded data³, namely the stagnation pressure and temperature in the nozzle reservoir region and the surface temperature on the model, are presented with minimal discussion in this chapter. Calibration curves for the infrared camera will also be presented. The analysis and discussion of these results have been reserved for Chapter 6.

5.2 Run 280

5.2.1 Stagnation conditions

Two features of the stagnation plots that the author wishes to bring to the reader's attention are firstly, the almost linear portion of the first half of the plots, and secondly, the first major "step" at approximately $t = 1.55$ s. The linear portion is attributed to the slow gas compression by the free piston, whereas the first step indicates the diaphragm rupturing, which marks the start of the test flow.

The stagnation temperature values were derived from the pressure values using an ideal gas isentropic relation (Fox et al. 2010). The method was explained in Chapter 3, but the equations will be repeated here for convenience.

³ A large amount of data was recorded by the acquisition system (30,000 readings) for each experiment. This is too much data to present in the current study, so readers interested in accessing the full data can attempt to contact the staff at TUSQ.

$$\frac{T_0}{T} = \left(\frac{p_0}{p}\right)^{\frac{\gamma-1}{\gamma}}$$

$$\therefore T_0 = T_{amb} \left[\left(\frac{p_0}{p_{amb}}\right)^{\frac{\gamma-1}{\gamma}} \right]$$

5.2.1.1 Pressure

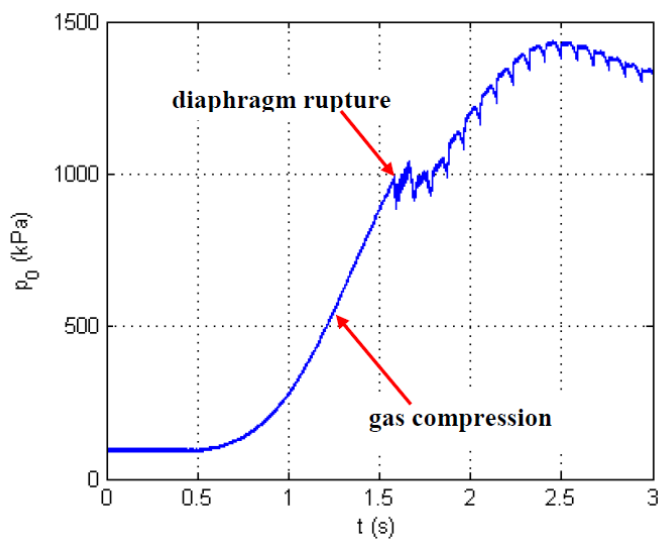


Figure 5.1: Stagnation pressure in nozzle reservoir region

5.2.1.2 Temperature

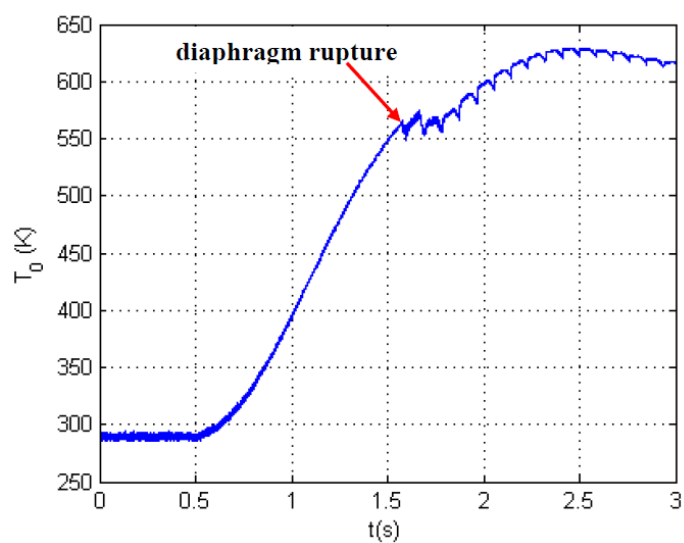


Figure 5.2: Stagnation temperature derived from pressure measurements in nozzle reservoir region

5.2.2 Surface temperature

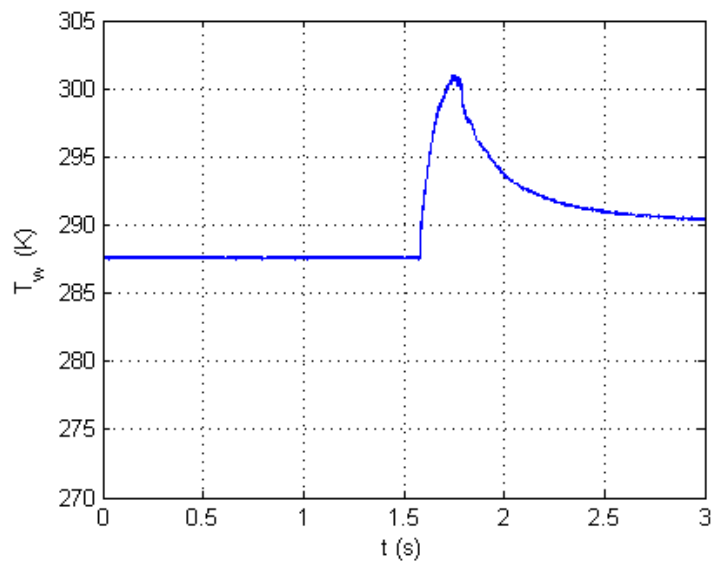


Figure 5.3: Surface temperature recorded by thermocouple (Run 280)

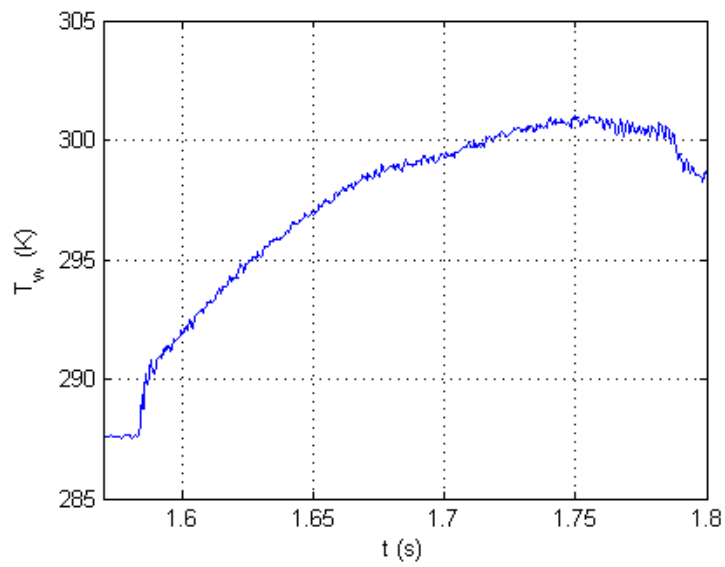


Figure 5.4: Surface temperature recorded by thermocouple during flow (Run 280)

5.3 Run 285

5.3.1 Stagnation conditions

5.3.1.1 Pressure

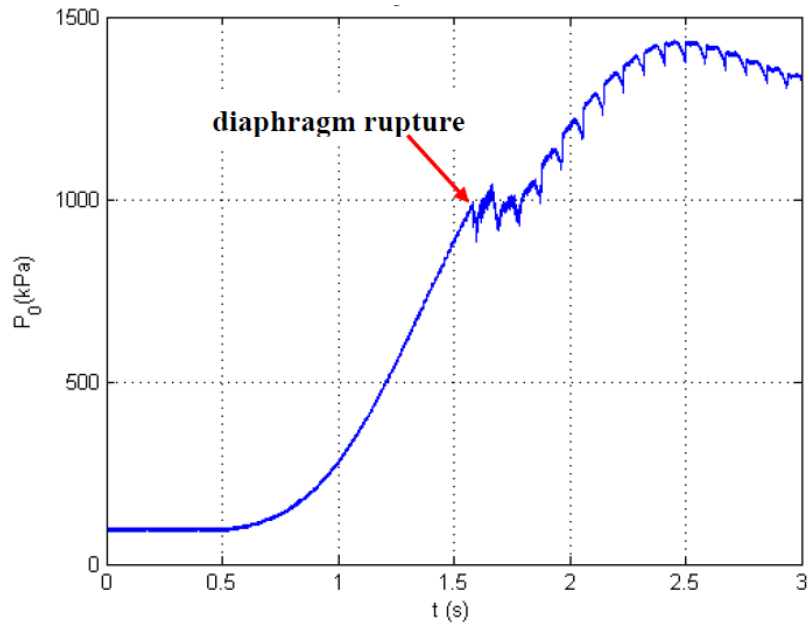


Figure 5.5: Stagnation pressure in nozzle reservoir region

5.3.1.2 Temperature

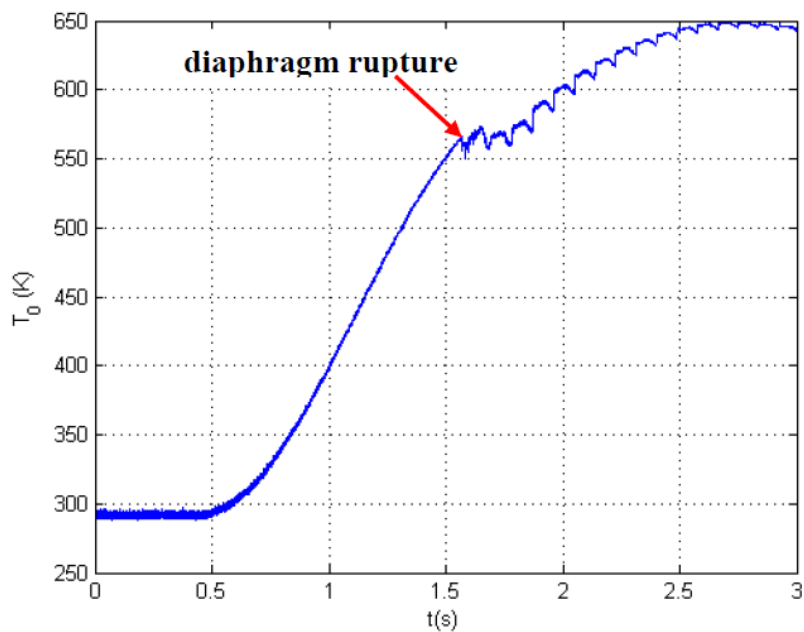


Figure 5.6: Stagnation temperature derived from pressure measurements in nozzle reservoir region

5.3.2 Surface temperature

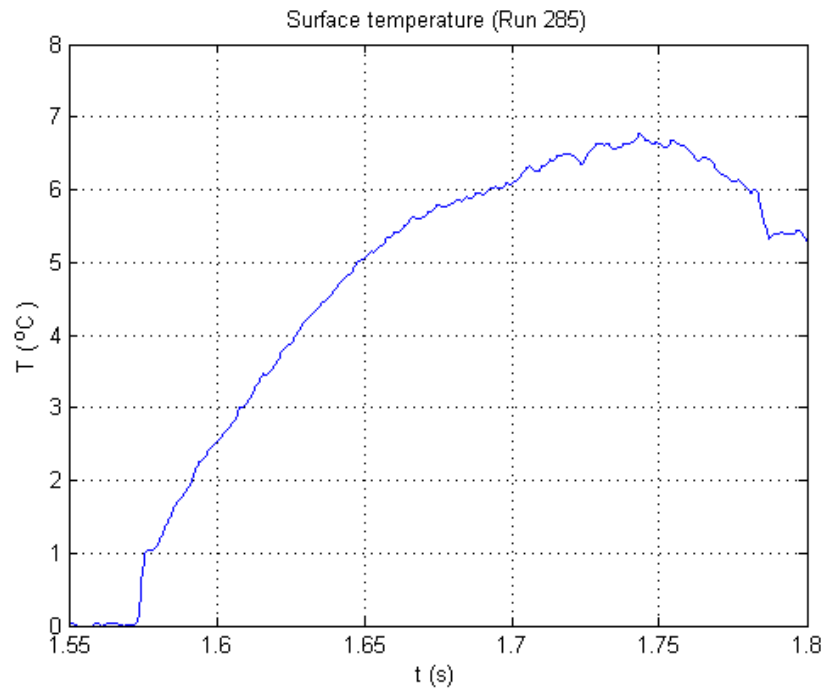


Figure 5.7: Surface temperature recorded by thermocouple during flow for Run 285

5.4 Infrared Camera Calibration Curves

An in-situ calibration of the infrared camera was performed in the test section of the tunnel. The temperature ranges used in the calibrations are presented in Table 5.1. Calibration curves were generated and are depicted in Figure 5.8, Figure 5.9, and Figure 5.10. The significance of these curves will be highlighted and discussed in Chapter 6.

Table 5.1: Temperature ranges used in IR system calibration sequences

Sequence	Range ($^{\circ}\text{C}$)	Increment ($^{\circ}\text{C}$)
1	$30 < T_w < 75$	5
2	$25 < T_w < 37$	1
3	$16 < T_w < 26$	0.5

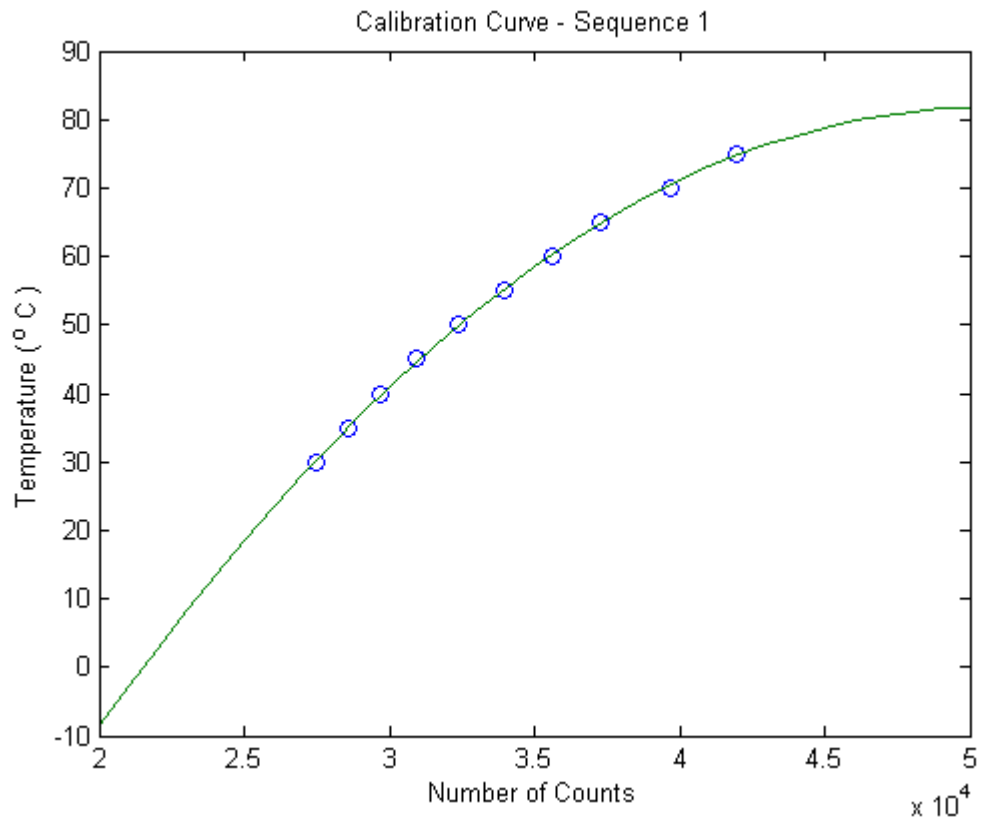


Figure 5.8: Sequence 1 calibration curve

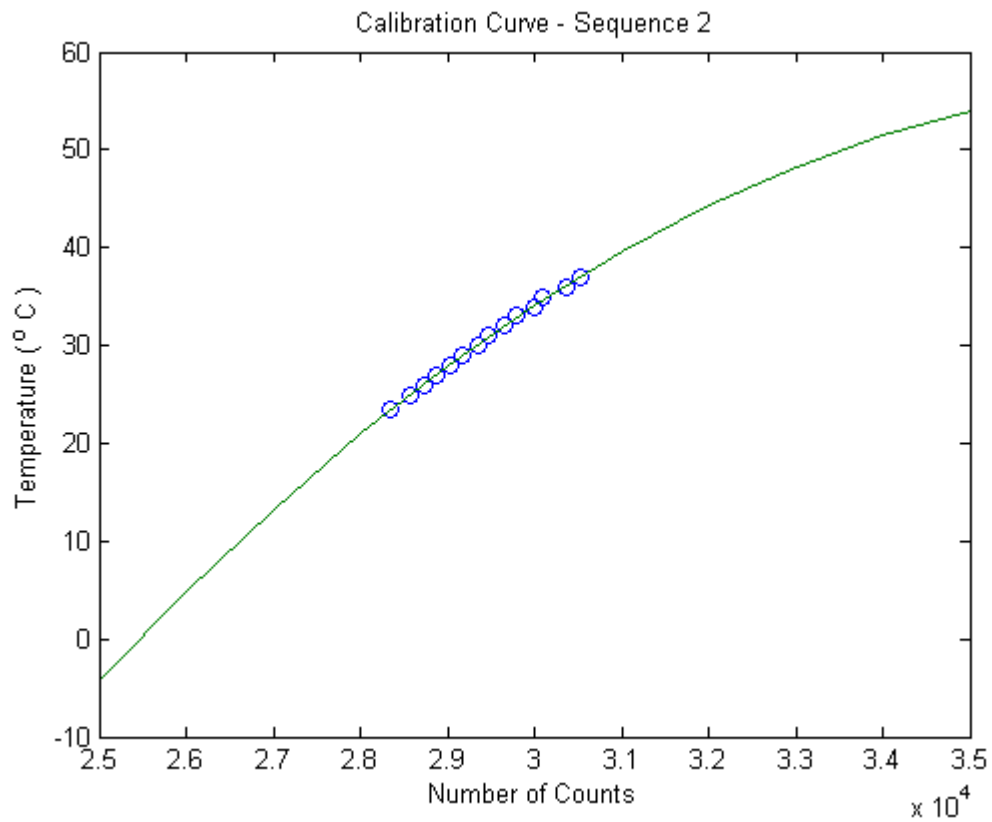


Figure 5.9: Sequence 2 calibration curve

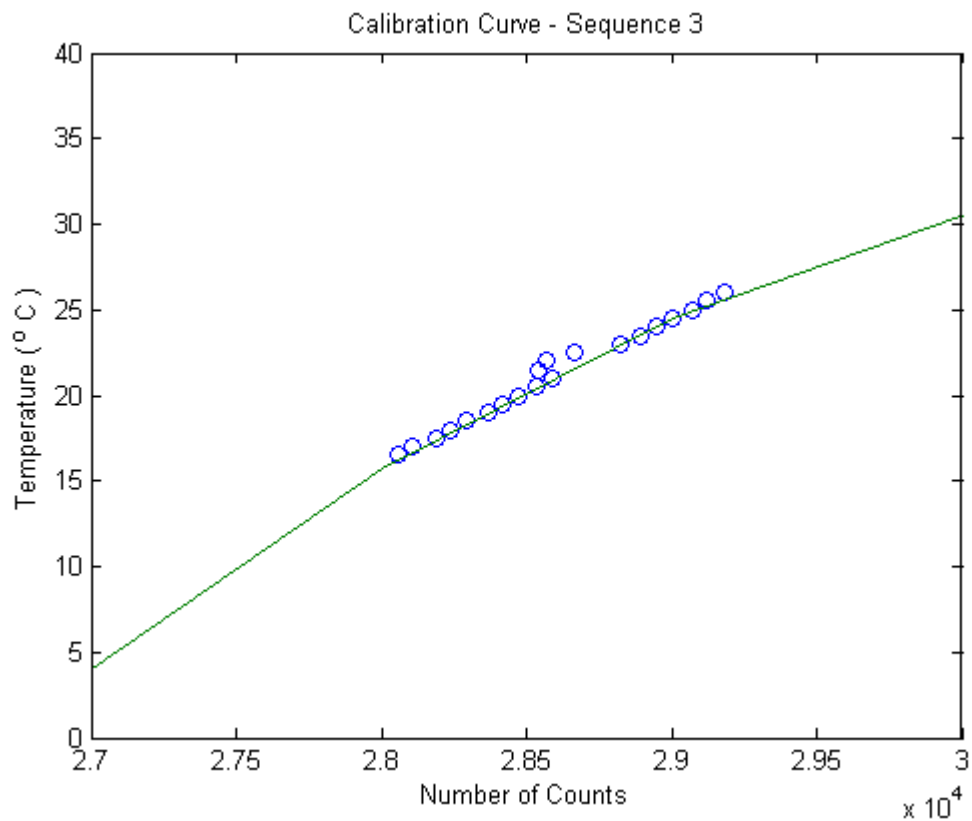


Figure 5.10: Sequence 3 calibration curve

Note that the outliers in the calibration curve for Sequence 3 (Figure 5.10) are due to operator error during the in-situ calibration.

5.5 Chapter Summary

The experimental results were presented in this chapter, namely the plots of the stagnation pressure as measured by the piezoelectric pressure transducer, the derived stagnation temperature plots and the surface temperature histories recorded by the surface junction thermocouple. The calibration curves for the infrared camera were also presented.

Chapter 6 will cover a detailed analysis and discussion of these results.

Chapter 6

Analysis and Discussion

'...it should be clear that an integral part of any test program should be the analysis of the data and comparisons with theoretical/computational solutions.

- John Bertin, *Hypersonic Aerothermodynamics* (1994 pp.175-176)

6.1 Chapter Overview

An analysis and discussion of the results presented in Chapter 5 will be covered in this chapter.

The chapter will open with a comparison of the analytically and empirically derived values of the local heat flux on the model.

Then thermal infrared camera calibration results will then be discussed. This section will highlight the importance of proper calibration of the camera, and how aspects such as selecting the correct temperature range and pixels on the thermograms (thermal images) to locate the thermocouples, must not be overlooked.

The chapter will conclude with a presentation of calibrated surface heat flux plots. The knowledge gained from the author's comprehensive review of studies in axial corner flow and the use of infrared thermography in hypersonic experiments will be applied in this instance in an attempt to identify and quantify the effects of aerodynamic heating on the model.

6.2 Comparison of Analytical and Empirical Values of Local Heat Flux

The results of the local heat flux values derived empirically and analytically are presented in Table 6.1.

The analytical results are approximately 11% and 13% of the empirical values for Run 280 and Run 285, respectively. The differences would be attributed to a couple of possibilities. One likely cause was the simplicity of the analysis. The flow was assumed to be inviscid, laminar and steady. However, indicators such as the high local Reynolds numbers for both analyses and the high local heat flux derived from the transient measurements, points to a turbulent flow. As discussed earlier in Chapter 2, the shock wave-boundary layer interactions in a configuration such as that used in the present study are very complex and results in severe aerodynamic heating effects, even in a cold flow.

Therefore, in spite of accounting for viscous dissipation through the recovery factor in the aerodynamic heating prediction (Anderson 2006 p.298) it was obviously inadequate in predicting heating due to the presence of phenomena such as boundary layer reattachment and the transmitted and reflected shocks in the corner region.

Table 6.1: Analytical and empirical values of local heat flux

Experiment	Analytical	Empirical
Run 280	$3.95 \frac{kW}{m^2}$	$34.5 \frac{kW}{m^2}$
Run 285	$3.88 \frac{kW}{m^2}$	$29.2 \frac{kW}{m^2}$

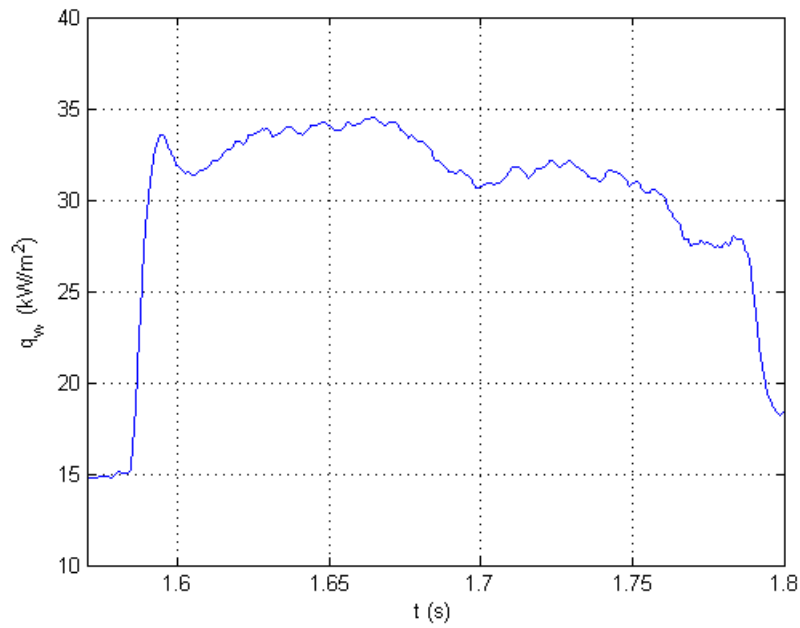


Figure 6.1: Surface heat flux on model during test flow (Run 280)

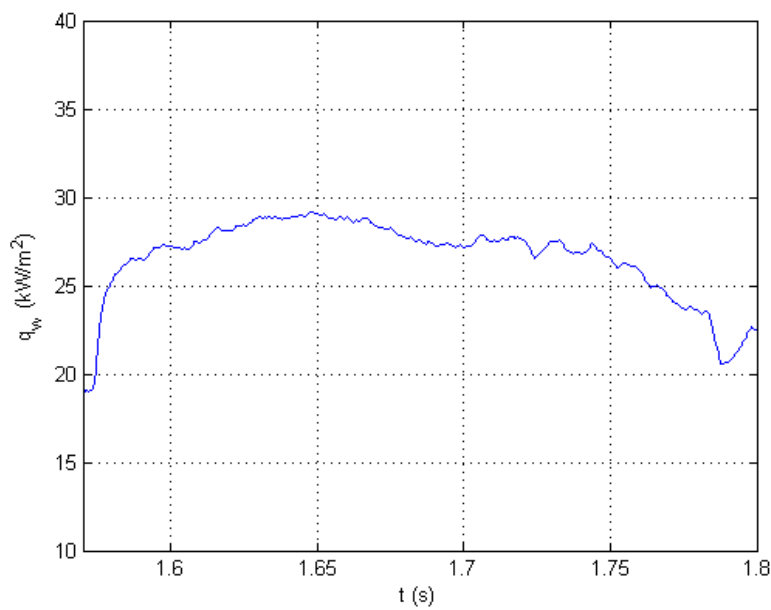


Figure 6.2: Surface heat flux on model during test flow (Run 285)

6.3 Calibration of Infrared Camera

6.3.1 In situ calibration

An in situ calibration (as described in Chapter 2) of the thermal infrared camera using the K-type thermocouple was performed inside the test section of the tunnel for Run 285.

6.3.2 Derivation of temporal information from Run 285 video

The camera software generates only spatial information of the temperature distribution over its target object. In order to compare the calibrated plots to those produced from the recorded data, a time scale needed to be established. Therefore, the author developed a novel method of achieving this task using MATLAB.

The MATLAB file is presented in Appendix E. The MATLAB functions `VideoReader` and `get` were used to determine the number of frames and duration of the recorded video file of Run 285 (`run285.avi`). This information was then used to calculate the duration of the 200 thermograms that were individually captured by the author. Of the results presented in Table 6.2, the author wishes to draw the reader's attention to the calculation of t_{flow} . The number of frames during the flow period is increased by one. This was to ensure that all frames in this range were counted and thus included in the calculation.

Table 6.2: Results from temporal calculations for video of Run 285

Property	Value
Duration (t_{vid})	2.5766s
Number of frames (n_{frames})	286
Frame duration (t_{frame})	$t_{\text{frame}} = \frac{2.5766s}{286 \text{ frames}} = 9.0091 \times 10^{-3} \frac{s}{\text{frame}}$
Duration of 200 frames	$9.0091 \times 10^{-3} \frac{s}{\text{frame}} \times 200 \text{ frames} = 1.802s$
Start frame for flow (f_{start})	148
End frame for flow (f_{end})	170

Flow duration from frame and time information (t_{flow})	$t_{flow} = [(f_{end} - f_{start}) + 1] \times t_{frame}$ $t_{flow} = ((170 - 148) + 1)frames \times 9.0091 \times 10^{-3} \frac{s}{frame}$ $\therefore t_{flow} = 0.20721s = 207.21ms$
--	---

6.3.3 Comparisons of recorded surface temperature history with calibrated temperature values

It was important before mapping the surface heat flux to ensure that the camera was calibrated as correctly as possible. Therefore, the calibration curves presented in a previous section were used to plot calibrated temperature values at the thermocouple location used in Run 285. These curves were then compared with the surface temperature history provided by the thermocouple reading for this run to determine the most accurate calibration curve to use for creating a surface heat flux map.

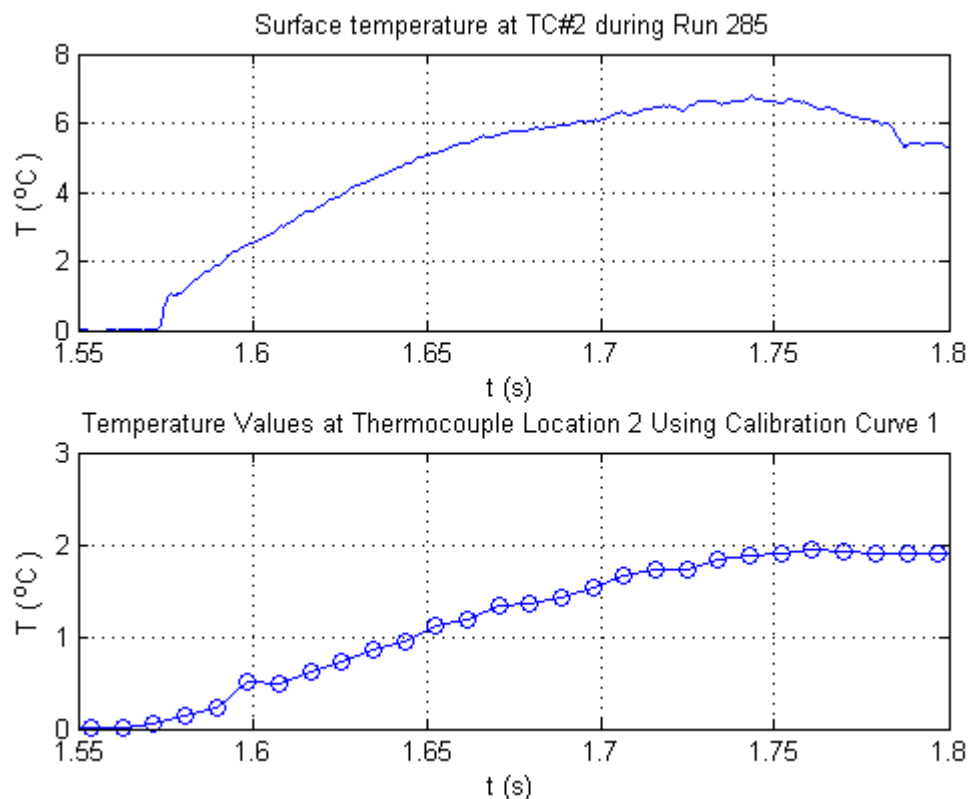


Figure 6.3: Recorded temperature curve and calibrated temperature curve using Sequence 1

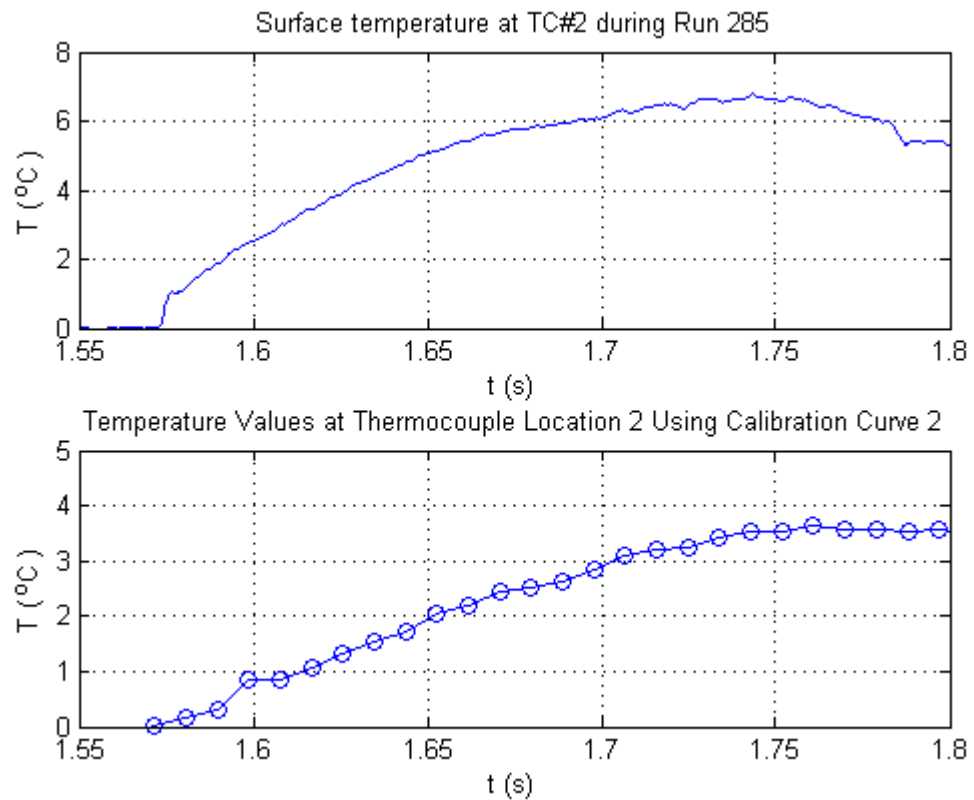


Figure 6.4: Recorded temperature curve and calibrated temperature curve using Sequence 2

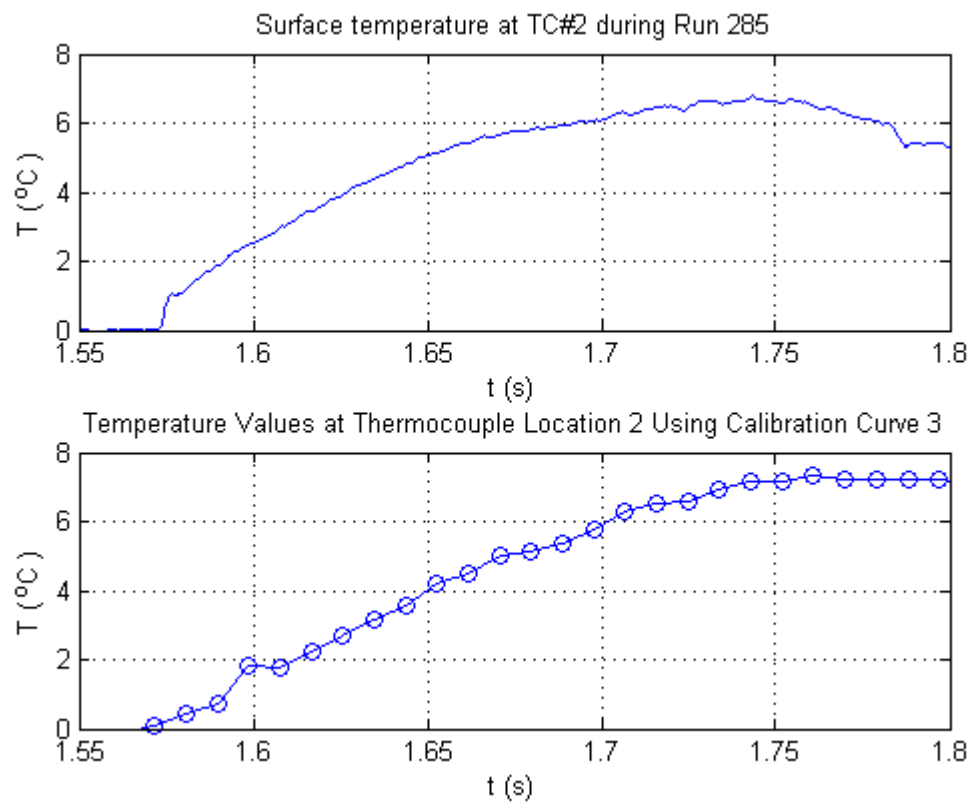


Figure 6.5: Recorded temperature curve and calibrated temperature curve using Sequence 3

Each calibrated temperature curve is similar in shape to the recorded surface temperature history curve.

However, upon closer inspection, the curve produced by Calibration Sequence 1 (Figure 6.3) differs from the recorded temperature curve by a factor of three. Similarly, the calibrated curve from Sequence 2 (Figure 6.4) differs from the recorded temperature curve by a factor of two. The calibrated curve from Sequence 3 is the most identical to the recorded temperature curve.

These differences highlight three of the important considerations of in-situ calibrations that were described in Chapter 2: understanding the effects of extraneous emissions, selecting the correct temperature range and selecting the correct pixels in the thermogram.

6.3.3.1 Identifying and understanding the effects of extraneous emissions during calibration

The gradients in all the calibrated curves are steeper than the recorded temperature curve. The presence of extraneous emissions in the tunnel during the calibration process (most notably the heat gun) would most certainly have affected the signal detected by the Mercury Cadmium Telluride (MCT) detector in the camera, contributing to a steeper temperature gradient.

A corollary to the aforementioned reason is the other likely reason for the discrepancy between the two curves. As discussed in Chapter 3, the experimental model is made of Perspex, which is a material with a low thermal diffusivity, α . It retains incident thermal energy longer that makes it ideal for infrared thermography. The Mercury Cadmium Telluride (MCT) detector array would have detected the residual heat radiating from the Perspex model even after the flow had stopped, resulting in the calibrated temperature curve (Figure 6.5) exhibiting the plateaus after $t = 1.75s$.

Conversely, the type K thermocouple has a higher thermal diffusivity, and conducts heat faster. It also has a high thermal sensitivity that makes it suitable for transient temperature measurement in hypersonic flow studies. This means that the temperature it senses is virtually that experienced by the surface to which it is attached. Thus, the thermocouple recorded temperature curve (Figure 6.5) tapers off sooner than the calibrated curve in response to the test flow ending.

6.3.3.2 Selecting the correct temperature range to calibrate the camera

The most likely cause for the differences between the recorded temperature history and the Sequence 1 and 2 calibration curves are the temperature ranges at which the camera was calibrated. As described in Chapter 2, it is important with in-situ calibrations that the measured thermocouple values must cover the whole temperature range of interest (Simeonides 1993).

The original recorded data at Thermocouple 2 for Run 285 (Figure 6.6) showed a range of approximately $18.6^{\circ}\text{C} < T_w < 25.2^{\circ}\text{C}$. As Calibration Sequences 1 and 2 fell outside that range, it therefore led to the discrepancies depicted in Figure 6.3 and Figure 6.4.

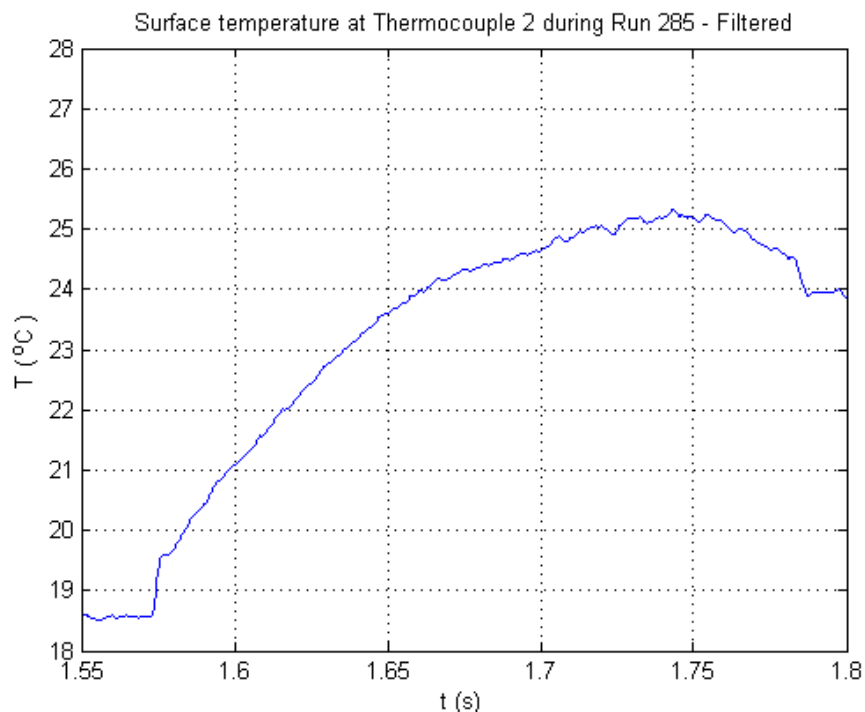


Figure 6.6: Filtered surface temperature history at Thermocouple 2 (Run 285)

6.3.3.3 Correctly locating the thermocouple junction in the thermograms

A thermocouple only senses the temperature of its junction (Simeonides et al. 1993). Generating the calibration curves involves carefully inspecting the thermographs and estimating the pixel locations over the thermocouple junction. As Lafferty and Collier (1991) realised, the exact location of the thermocouple in the thermograph is necessary to compare the calibrated and thermocouple recorded data.

As an example, a thermograph of the experimental model at approximately 75°C was taken during the calibration process (Figure 6.7). The image resolution, per the settings described in Section 4.3.6, is 512 x 400 pixels. Plots of the calibrated surface temperature history over the thermocouple junction region are shown in Figure 6.8 and Figure 6.9. The first set of numbers in (331:400, 81:90) refers to the range of pixels along the vertical direction. The second set of numbers refers to the range of pixels along the horizontal direction.

As depicted, the larger range of pixels selected resulted in a calibrated curve that differed from the recorded curve (Figure 6.6) by a factor of about two. When the pixel range was reduced, the calibrated curve was more alike the recorded curve. This confirms the findings Lafferty and Collier (1991) in relation to pixel selection.

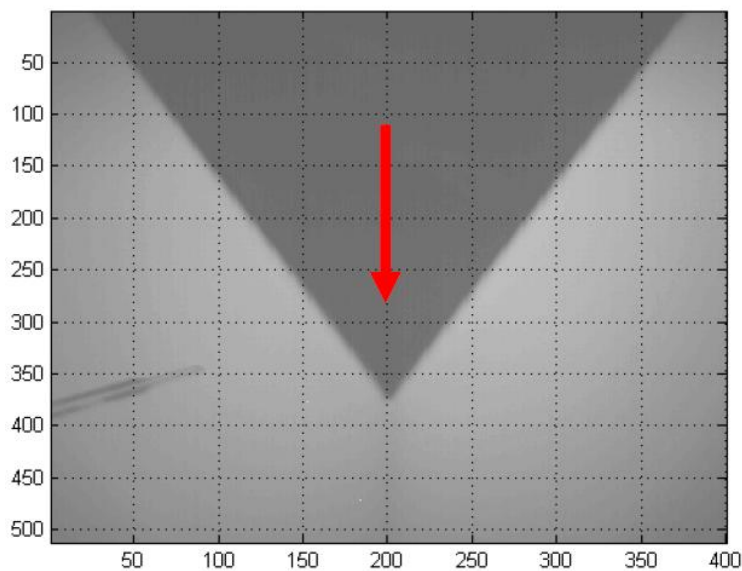


Figure 6.7: Thermograph of model approximately 75°C (flow direction indicated with red arrow)

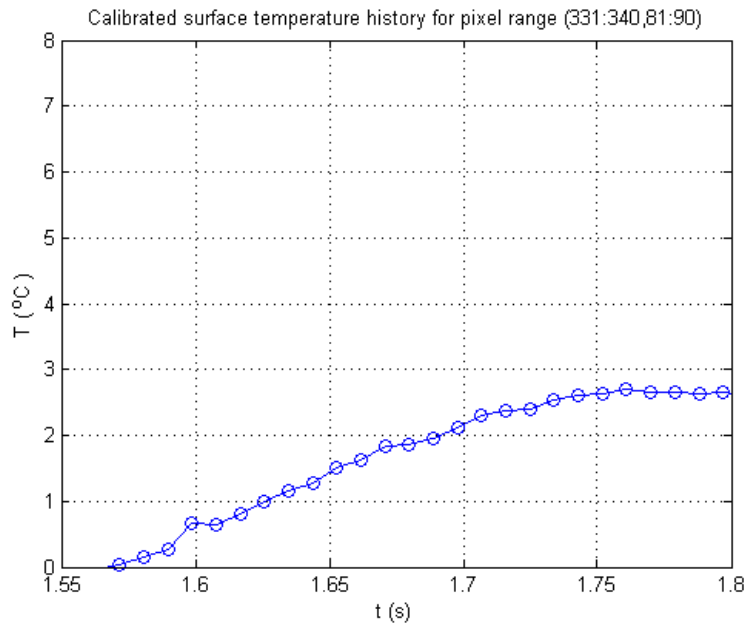


Figure 6.8: Calibrated surface temperature history for pixel range (331:340, 81:90)

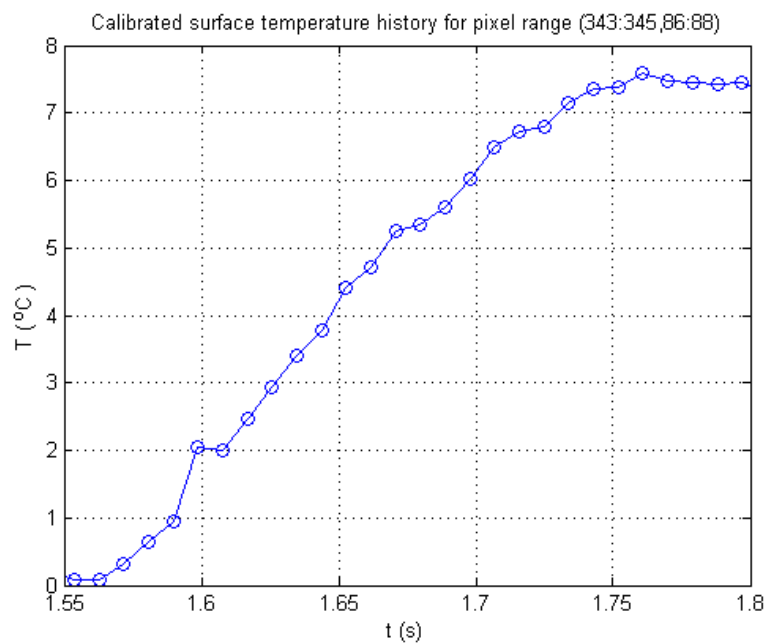


Figure 6.9: Calibrated surface temperature history for pixel range (343:345, 86:88)

6.4 Identifying Peak Heating Regions and the Axial Corner Flow Phenomena

In an attempt to apply to his newly acquired knowledge of axial corner flow and the application of infrared thermography in hypersonic flow studies, the author outlined a plan to investigate whether the calibrated temperature and heat flux information could

be used to visualise and quantify the peak regions due to convective aerodynamic heating. The plan is outlined below.

1. Inspect the calibrated temperature curve to identify the frame/s where peak temperatures occur.
2. Plot surface heat flux maps of this and neighbouring frames in the sequence.
3. Select specific points (on the model surface) in those regions identified as exhibiting peak heating and plot calibrated heat flux histories to understand and hopefully identify the phenomena characteristic of the axial corner flowfield e.g. local boundary layer separation and reattachment.
4. Generate heat flux contour maps to provide a convenient method of quantifying the heat transfer effects of aerodynamic heating.

6.4.1 Inspection of calibrated temperature curve

The calibrated surface temperature plot for the thermocouple junction was inspected to determine the frame/s where peak temperatures occurred. The calibrated data is presented in two formats in Figure 6.10. In Figure 6.10(a), the temperature is plotted against time and in Figure 6.10(b), it is plotted against the number of frames. It was important to remember that from the surface temperature history plot recorded by the thermocouple (Figure 6.6), the flow starts at approximately $t = 1.57\text{s}$ and ends at $t = 1.78\text{s}$. Therefore, the peak temperatures occur in the vicinity of Frame 170, and not Frame 177, as it may seem if one were to rely solely on inspecting Figure 6.10(b).

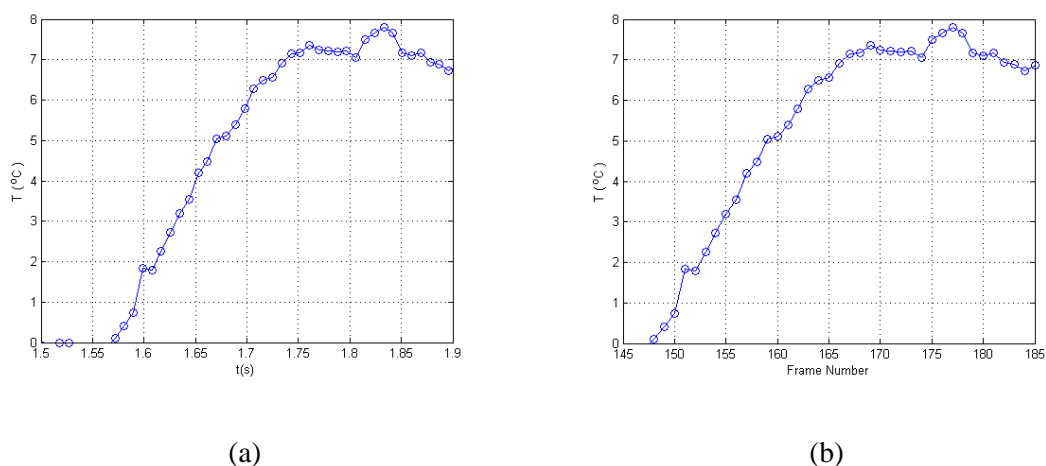


Figure 6.10: Calibrated surface temperature at thermocouple junction (a) Time (b) Number of frames

6.4.2 Surface heat flux mapping

Surface heat flux maps and corresponding contour maps were generated for Frame 170 and a few frames either side of it, namely Frame 166, 168, 172, and 174.

Surface heat flux maps for Frame 166 and Frame 168 using the MATLAB function `imagesc` are depicted in Figure 6.11. The other maps in this sequence look similar. Therefore, mapping frames very close to each other in a sequence at the level of resolution presented in Figure 6.11 does not yield much useful information aside from presenting a very pretty set of images.

However, what proves to be more useful is focusing on a section where a lot of activity seems to be occurring and generating contour maps. Hence, the usefulness of the images presented below lies in providing a good indication of where peak heating occurs.

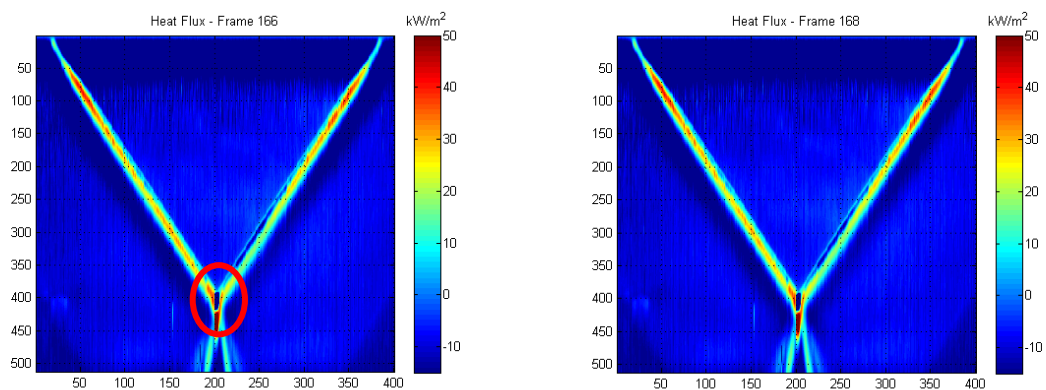


Figure 6.11: Surface heat flux maps of Frame 166 and Frame 168 for Run 285

The area of focus in this instance was the crotch or corner region of the model, indicated in Figure 6.11 by a red oval. The grid selection here was (350:420, 190:220), which was a resolution of 70 x 30 pixels. From the literature, and as discussed in Chapter 2, the flow in the corner region is characterised by a complex system of shock wave-boundary layer interactions; the local boundary layer separation and reattachment activity leads to regions of peak heating.

The whole sequence (Frame 166 to 174) is presented in the form of filled contour maps, generated using the MATLAB function `contourf`.

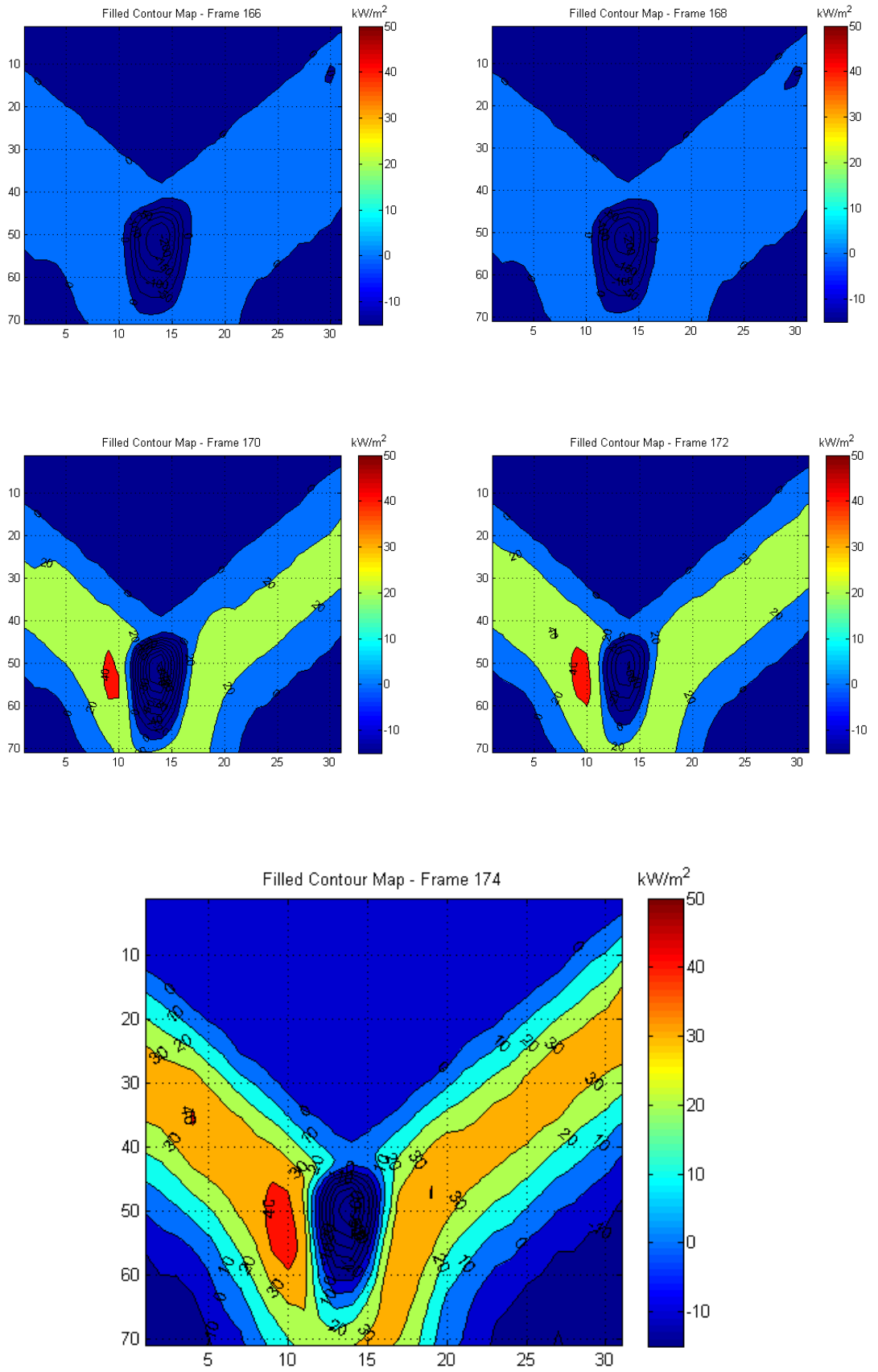


Figure 6.12: Filled contour heat flux maps of Frame 166 to Frame 174 for Run 285

As depicted in above in Figure 6.12, the filled contour maps provide a convenient method of quantifying the surface heat flux. It is important to note that the absolute values of the calibrated surface heat flux are not accurate. This is due to the author's very rudimentary understanding (at this stage anyway) of digital image processing with MATLAB, and any software for that matter.

Overall, however, the contour maps still provide a good visualisation of the heat flux activity on the model and their relative magnitudes. Moreover, it provides a good indication of where peak heating occurs, which forms part of the intended purpose of the current study.

Understandably, more work is required to establish a better understanding in the area of digital image processing of the thermograms.

6.4.3 Identification of boundary layer separation and reattachment

Streamwise locations on the experimental model were selected, with the aim of generating useful surface temperature and heat flux histories in the hope of identifying the phenomena of boundary layer separation and reattachment that is characteristic of axial corner flow (Charwat & Redekopp 1967).

The inspiration for this part of the investigation was the study by Henckel and Maurer (1989) and previous studies by researchers such as Charwat and Redekopp (1967) and Korkegi (1971). Henckel and Maurer selected a few locations on their experimental model (a swept-wing plate) and plotted the heat flux histories, whereas Korkegi and other researchers in similar studies focused on the axial corner configuration and took temperature and pressure measurements.

What they found was that the pressure and heat transfer measurements followed the same trend and that boundary layer separation could be observed by noticeable troughs in the pressure and heat transfer plots. Conversely, boundary layer reattachment could be observed by the plots exhibiting distinct peaks, which leads to destructive consequences, as evidenced by the case of the X-15 experimental aircraft.

As mentioned, the author selected a few points on the model in the streamwise direction. An example of a set of points is depicted in Figure 6.13.

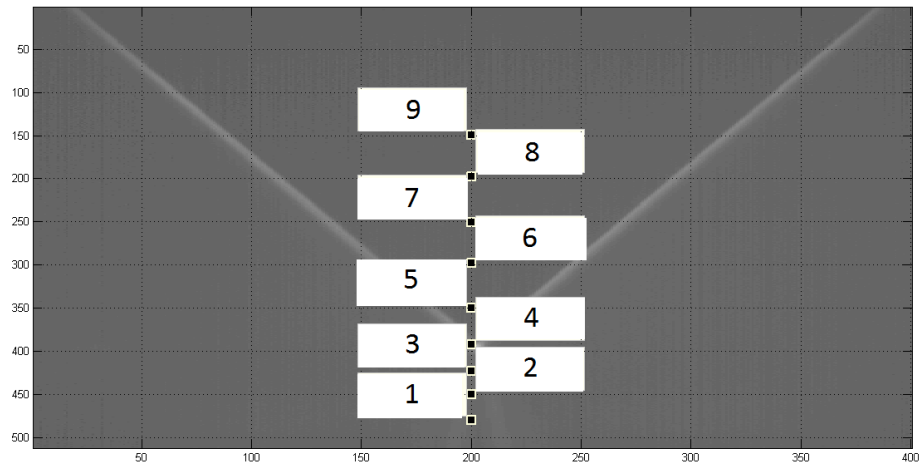


Figure 6.13: Streamwise locations on model to plot calibrated temperature and surface temperature histories

Unfortunately, the author did not generate a useful set of plots, although the following plot of locations 1 to 3 in Figure 6.14 shows some promise. The blue line is for the location of the crotch region of the model, and the other two lines are for locations further downstream of that point. Further analysis is required in this instance.

In summary, the author believes that useful information about the flow over the model can be gained by improving these plots and hopefully providing a better understanding of the interactions in the corner region.

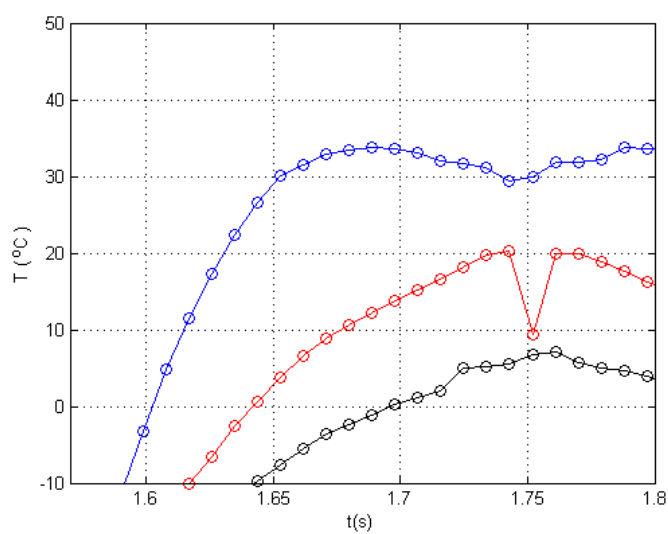


Figure 6.14: Temperature histories in streamwise direction for Locations (1), (2), and (3)

6.5 Uncertainty in Measurements

Uncertainty analysis is the procedure used to quantify data validity and accuracy. Careful study of this procedure may identify potential sources of unacceptable error can lead to improvement in measurement methods.

Although an important aspect of experimental work, this area was not covered to any significant extent in the current study due to time constraints. A brief list was generated of the sources of uncertainty related to the use of surface junction thermocouples and infrared thermography in hypersonic flow studies. A couple of the items are listed in the next chapter.

This area has been identified as further work in a subsequent study.

6.6 Chapter Summary

The results from Chapter 5 were analysed in the present chapter. A discussion on the in-situ calibration procedure and the heat flux maps produced were presented as well.

The conclusions from this study and further work will be presented in the next chapter.

Chapter 7

Conclusions and Further Work

7.1 Brief Review of Dissertation

This project sought to quantify the effects of convective aerodynamic heating over the experimental model at Mach 6. More specifically, the aims were to understand the nature of the flow in the crotch region of the model and to apply infrared thermography to map the surface heat flux in order to identify and quantify regions of peak heating.

The reader was introduced to the world of hypersonics and the topic and aims of this study in Chapter 1. Additionally, the relevance of the experimental model to the design of actual hypersonic inlets such as the Rectangular-to-Elliptical Transition (REST) inlet (Smart 2001), and the detrimental effects of aerodynamic heating were also described.

Chapter 2 covered background knowledge pertaining to the current work. In particular, the focus was on shock wave-boundary layer interactions, axial corner flow and heat transfer measurements using thermocouples and infrared thermography in hypersonic flow studies.

Chapter 3 introduced the analytical tools used in the project, namely a modified oblique shock theory, the aerodynamic heating equation, and the semi-infinite wall data reduction model.

The experimental setup was described in Chapter 4. Here, the reader was introduced to the equipment used to conduct the experiments, namely, The University of Southern

Queensland Hypersonic Wind Tunnel (TUSQ), the instrumentation (type K surface junction thermocouple and mid-wave infrared camera) and the experimental model.

The results were presented in Chapter 5 and discussed at length in Chapter 6. Included in the discussion was a comparison of the theoretical predictions of the flow conditions immediately downstream of the planar oblique shock waves and the heat flux values in two areas of the experimental model to the empirical results. The results and analysis of the in-situ calibrations of the infrared thermography system were also discussed and heat flux contour maps were also presented.

7.2 Conclusions

The results in this study have demonstrated that infrared thermography can be used as a means to identify peak heating regions on an object due to convective aerodynamic heating in a hypersonic flow.

The importance of properly calibrating the camera cannot be underestimated. As was demonstrated in the discussion and analysis of the experimental results, it is important to account for factors such as additional emission sources that affect the optical signal received by the camera, selecting the correct pixels and also the calibrating the thermocouple over the expected temperature range.

The knowledge gained from the review of studies investigating axial corner flow and the use of infrared thermography in hypersonic flow experiments was applied to analyse the experimental data. The author demonstrated that heat flux maps can aid in identifying areas of peak heating, and that contour mapping can be useful in quantifying those effects. As discussed in that chapter, more work is required in properly converting the calibrated temperature data into heat flux values. One of the major issues for the author was his inexperience in digital filtering techniques; hence, an area for further improvement.

Planning the experiments is very important. The author learned the importance of this facet of experimentation, as time could have been saved in calibrating the camera over the right temperature range and identifying earlier the need to take surface pressure measurements along with the temperature data. This information could have been used to identify local boundary layer separation and reattachment activity in the corner region.

7.3 Further Work

From the extensive work the author has conducted during the course of this project, the following areas have been identified for further work:

1. Surface pressure measurements
 - a. Span-wise and stream-wise measurements
 - i. Use this information to plot the pressure distribution in conical coordinates and locate peak regions of aerodynamic heating.
 - ii. Construct the flowfield model and compare against previous studies.
2. Improve the accuracy of the in-situ calibration procedure
 - a. Perform experiments to better identify and quantify uncertainties relating to the infrared camera and possibly the calibration process.
3. Perform experiments using the lower Mach number nozzles to look at the effects of shock interactions at a range of Mach numbers.
4. Conduct a numerical study of the different configurations.
5. Investigate the use of different surface flow visualisation techniques e.g. oil and Schlieren, to better understand axial corner flow over the configuration.
6. Identifying and quantifying all uncertainties (Korkegi 1971)
 - a. For instance, ensuring proper alignment of the model to yield equal pressures.

More can be added to the list, but the above constitutes the main bulk of what can be accomplished in an extension to the current work.

7.4 Closing

In closing, the author hopes that the reader has been taken on an interesting sojourn into the world of hypersonics, and in particular, an investigation into quantifying heat flux over a double swept-wedge configuration at Mach 6. Moreover, the author hopes that the reader has gained an understanding of, and an appreciation for, the importance of convective aerodynamic heating in the design of hypersonic flight vehicles⁴.

⁴ Finally, the author apologises for some formatting issues in this document. One of the many important lessons learned during this project was this: learn how to use LaTeX. MS Word will only give you grief.

List of References

- [1] Albertson, CW & Venkat, VS 2005, 'Shock Interaction Control for Scramjet Cowl Leading Edges', *AIAA/CIRA International Space Planes and Hypersonics Systems and Technologies Conference*, American Institute of Aeronautics and Astronautics, USA
- [2] Anderson, JD 2006, *Hypersonic and High-Temperature Gas Dynamics*, 2nd edn, American Institute of Aeronautics and Astronautics, Reston, Virginia
- [3] Buttsworth, DR 2001, 'Assessment of effective thermal product of surface junction thermocouples on millisecond and microsecond time scales', *Experimental Thermal and Fluid Science*, vol. 25, no. 6, pp. 409-420
- [4] Buttsworth, DR 2010, 'Ludwig Tunnel Facility with Free Piston Compression for Supersonic and Hypersonic Testing', *9th Australian Space Science Conference 2009*, Proceedings of the 9th Australian Space Science Conference, National Space Society of Australia Ltd, pp. 153-162
- [5] Carlomagno, GM Cardone, G Meola, C, and Astarita, T 1998 'Infrared Thermography as a Tool for Thermal Surface Flow Visualization', *Journal of Visualization*, vol.1, no.1, pp. 37-50
- [6] Charwat, AF & Redekopp, LG 1967, 'Supersonic Interference Flow Along the Corner of Intersecting Wedges', *AIAA Journal*, vol. 5, no. 3, pp. 480-488
- [7] Digi-key Corporation, 2014, *AD595AQ-ND*, Digi-key Corporation, Minnesota, USA, viewed 28 October 2014, <<http://www.digikey.com.au/product-detail/en/AD595AQ/AD595AQ-ND/612045>>
- [8] Edwards, n.d., *ADC (Active Digital Controller) Standard*, Edwards, Crawley, UK, viewed 28 October 2014, <<https://shop.edwardsvacuum.com/products/List.aspx?r=68>>
- [9] Emanuel, G 1992, 'Oblique shock wave with sweep', *Shock Waves*, vol. 2, no. 1, pp. 13 - 18
- [10] Ennis, RJ 2013, 'Scramspace Hypersonic Aerodynamic Drag Coefficient', ENG4111/ENG4112 Research Project, University of Southern Queensland, Toowoomba
- [11] Fox, RW Pritchard, PJ & McDonald AT, 2010, *Introduction to Fluid Mechanics*, 7th edn, John Wiley & Sons (Asia) Pte Ltd

- [12] Gounko, YP & Mazhul, II 2013, 'Numerical investigation of flow over two sweepback wedges at $M = 4$ and 6 ', *Thermophysics and Aeromechanics*, vol. 20, no. 2, pp. 179-193
- [13] Henckels, A & Maurer, F 1989, 'Applications of Infra-red Thermography in a Hypersonic Blowdown Wind Tunnel', *International Congress on Instrumentation in Aerospace Simulation Facilities*, Göttingen, West Germany, pp. 516-524
- [14] Malpress, R & Buttsworth, DR 2013, *TUSQ Operating Manual*, University of Southern Queensland
- [15] McGee, TD 1988, *Principles and Methods of Temperature Measurement*, John Wiley and Sons, New York, USA
- [16] National Instruments Corporation 2014, *Data Acquisition*, National Instruments Corporation, Austin, Texas, viewed 27 October 2014, <<http://www.ni.com/dataacquisition/nidaqmx.htm>>
- [17] Oldfield, MLG 2000, *OUEL Report 2233/2000: Guide to Impulse Response Heat Transfer Signal Processing Version 2*, University of Oxford, Department of Engineering Science, Oxford, UK
- [18] Omega Engineering Inc. 2014, *Cement-On Surface Thermocouples*, Omega Engineering Inc., Stamford, Connecticut, USA, viewed 26 July 2014, <<http://www.omega.com/pptst/CO-K.html>>
- [19] Productive Plastics 2014, *Perspex for glazing*, Productive Plastics, Perth, Western Australia, viewed 17 October 2014, <http://www.productiveplastics.com.au/uploaded/files/client_added/Mitchell%20Plastics%20-%20Glazing_236eng.pdf>
- [20] Roache, B 2004, 'Heat Transfer Measurements of a Re-entry Capsule Using Fast Response Thermocouples', ENG4111/ENG4112 Research Project, University of Southern Queensland, Toowoomba
- [21] Simeonides, G Vermeulen, JP Boerrigter, HL & Wendt, JF 1993, 'Quantitative Heat Transfer Measurements in Hypersonic Wind Tunnels by Means of Infrared Thermography', *IEEE Transactions on Aerospace and Electronic Systems*, vol. 29, no. 3, pp.878-893
- [22] sInfraRed Ptd Ltd 2014, *Onca-MWIR-MCT-640*, sInfraRed Pte Ltd, Midview City, Singapore, viewed 27 October 2014, <http://www.sinfrared.com/en/infrared_camera/mwir_mid_wave_infrared/onca-mwir-mct-640.asp>

-
- [23] TekNet Electronics, n.d., *DPI 260 Series: Digital Pressure Indicators*, TekNet Electronics, Atlanta, Georgia, viewed 28 October 2014, <http://www.teknetelectronics.com/DataSheet/DRUCK/DRUCK_DPI261.pdf>
- [24] Widodo, A 2012, 'Temperature Variations in a Free Piston Compression Wind Tunnel', PhD Thesis, University of Southern Queensland, Toowoomba

Appendix A

Project Specification

The University of Southern Queensland

FACULTY OF HEALTH, ENGINEERING AND SCIENCES

ENG 4111/4112 Research Project

PROJECT SPECIFICATION

- FOR:** James FUATA
- TOPIC:** Quantifying the Effects of Convective Aerodynamic Heating over a Double Swept-Wedge Configuration at Mach 6
- SUPERVISOR:** Dr. David Buttsworth
- ENROLMENT:** ENG 4111 /ENG 4112 – External, 2014
- PROJECT AIM:** This project seeks to quantify the effects of convective aerodynamic heating over a double swept-wedge configuration at a nominal flow speed of Mach 6. Type K surface junction thermocouples and infrared thermography will record surface temperature data, which will be analysed and processed in MATLAB to determine the heat transfer rates into the model. From there, surface heat flux maps will be produced to identify and quantify regions of peak heating due to convective aerodynamic heating.
- PROGRAMME:** Issue B, 1st October 2014

1. Conduct a literature review on hypersonic flow theory and axial corner flow
2. Understand swept oblique shock analysis and shock-boundary layer interactions.
3. Perform analytical calculations of the post-oblique shock flow conditions and heat transfer rates on the experimental model.
4. Take surface temperature readings of the experimental model with K type thermocouples.
5. Use infrared thermography to visualise the surface temperature on the experimental model.
6. Process and analyse experimental data in MATLAB to determine heat transfer rates.

7. Produce surface heat flux maps of the experimental model.
8. Compare empirical and theoretical results.

As time permits:

1. Complete new model of the experimental model (including surface pressure taps)

AGREED James Fuata (Student) _____ (Supervisor)

Date: 01 / 10 / 2014

Date: / / 2014

Appendix B

Oblique Shock Wave with Sweep

Introduction

The following method has been partially reproduced and adapted from the paper, *Oblique shock wave with sweep (1992)*, with permission from the author, Dr. George Emanuel⁵.

Nomenclature

In this analysis, a wedge is considered, whose lower surface is parallel to the x, z plane and aligned with the freestream. A cartesian coordinate system is used (Figure B.1), where x is aligned with the flow and y and z lay in planes perpendicular to the flow direction. In the x, y plane, the upper wedge surface and planar shock have angles θ and β , respectively. The leading edge of the wedge has a sweep angle of Λ . A plane that is perpendicular to the leading edge is called the sweep plane and is denoted with a \perp subscript. Downstream of the attached shock, the flow is denoted with a unity subscript.

Assumptions and Methodology

For inviscid flow of a perfect gas, the jump conditions associated with sweep, such as the pressure ratio $\left(\frac{p_1}{p_\infty}\right)$, stagnation pressure ratio $\left(\frac{p_{01}}{p_{0\infty}}\right)$, and the downstream Mach number M_1 will be determined.

The specific heat ratio (γ), wedge angle (θ) and freestream Mach number (M_∞) are assumed to be known, while the sweep angle (Λ) is a free parameter.

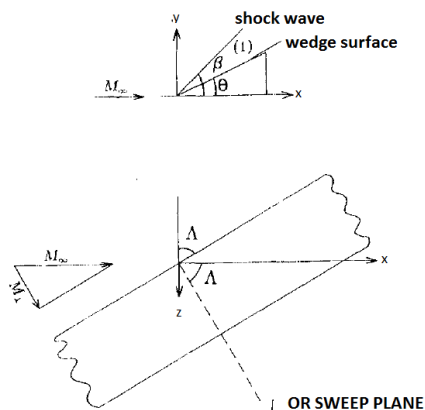


Figure B.1: Coordinate system for analysis (Emanuel 1992)

⁵ Permission granted on 25/10/14.

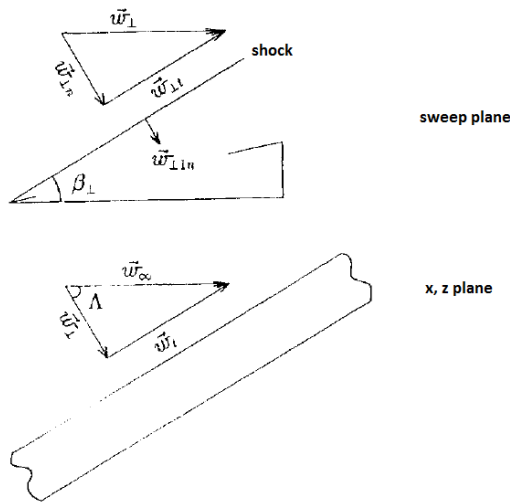


Figure B.2: Schematic showing various velocity components (Emanuel 1992)

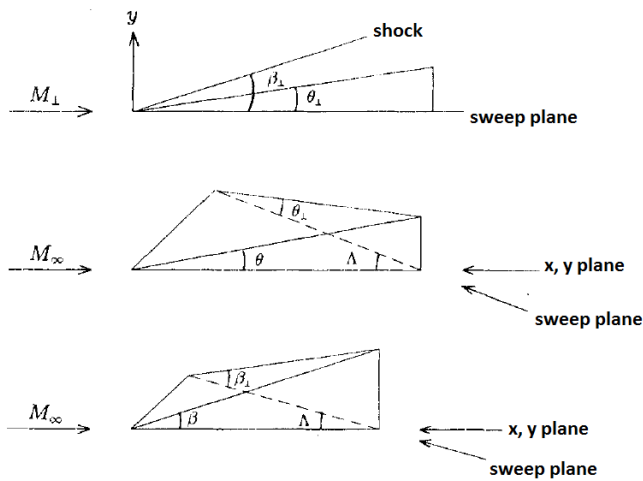


Figure B.3: Schematic relating various angles (Emanuel 1992)

Figure B.1 and Figure B.2 yield

$$M_{\perp} = M_{\infty} \cos \Lambda \tag{B.1}$$

$$\theta_{\perp} = \tan^{-1} \left(\frac{\tan \theta}{\cos \Lambda} \right) \tag{B.2}$$

The shock wave angle in the sweep plane (β_{\perp}) is implicitly given in the relation:

$$\tan \theta_{\perp} = \cot \beta_{\perp} \frac{M_{\perp}^2 \sin^2 \beta_{\perp} - 1}{1 + \{[(\gamma + 1)/2] - \sin^2 \beta_{\perp}\} M_{\perp}^2} \quad (\text{B.3})$$

$$\beta_{\perp} = \tan^{-1} \left\{ \frac{M_{\perp}^2 - 1 + 2\lambda \cos[(4\pi\delta + \cos^{-1} \chi)/3]}{3 \left(1 + \frac{\gamma - 1}{2} M_{\perp}^2\right) \tan \theta_{\perp}} \right\} \quad (\text{B.4})$$

where

$$\lambda = \left[(M_{\perp}^2 - 1) - 3 \left(1 + \frac{\gamma - 1}{2} M_{\perp}^2\right) \left(1 + \frac{\gamma + 1}{2} M_{\perp}^2\right) \tan^2 \theta_{\perp} \right]^{\frac{1}{2}} \quad (\text{7.1})$$

$$\chi = \frac{1}{\lambda^3} \left[(M_{\perp}^2 - 1)^3 - 9 \left(1 + \frac{\gamma - 1}{2} M_{\perp}^2\right) \right. \\ \left. \times \left(1 + \frac{\gamma - 1}{2} M_{\perp}^2 + \frac{\gamma + 1}{4} M_{\perp}^4\right) \tan^2 \theta_{\perp} \right] \quad (\text{7.2})$$

For an attached shock $|\chi| \leq 1$, while $\delta = 0$ for a strong solution shock and $\delta = 1$ for the weak solution.

Note that the above equations explicitly provide M_{\perp} , θ_{\perp} , and β_{\perp} in terms of γ , M_{∞} , θ and Λ .

The shock wave angle in the x, y plane then is

$$\beta = \tan^{-1}(\cos \Lambda \tan \beta_{\perp}) \quad (\text{7.3})$$

We observe that the following inequalities hold when $0 \leq \Lambda \leq \frac{\pi}{2}$.

$$1 \leq M_{\perp} \leq M_{\infty} \quad (\text{7.4})$$

$$\theta \leq \theta_{\perp} \quad (\text{7.5})$$

$$\beta \leq \beta_{\perp} \quad (\text{7.6})$$

Thus, the wedge and shock angles in the sweep plane equal or exceed their values in the x, y plane.

The normal component of the upstream Mach number in the sweep plane is given by:

$$M_{\perp n} = M_{\perp} \sin \beta_{\perp} \quad (7.7)$$

while its downstream counterpart is

$$M_{\perp 1n} = \left\{ \frac{1 + [(\gamma - 1)/2]M_{\perp n}^2}{\gamma M_{\perp n}^2 - (\gamma - 1)/2} \right\}^{\frac{1}{2}} \quad (7.8)$$

The Mach number component downstream of the shock in the sweep plane is

$$M_{\perp 1} = \frac{M_{\perp 1n}}{\sin(\beta_{\perp} - \theta_{\perp})} \quad (7.9)$$

The various ratios depend only on the ratio of specific heats and the normal component of the Mach number in the sweep plane.

For instance, the well known equation for pressure jump is given by:

$$\frac{p_1}{p_{\infty}} = \frac{2}{\gamma + 1} \left(\gamma M_{\perp n}^2 - \frac{\gamma - 1}{2} \right) \quad (7.10)$$

The foregoing relations cannot be used for the Mach number downstream of the shock (M_1). This number requires establishing \mathbf{w}_1 . As shown in the above figure, \mathbf{w}_{∞} is first decomposed into a component \mathbf{w}_t that is parallel to the leading edge of the wedge and a component \mathbf{w}_{\perp} that is perpendicular. The velocity is further decomposed into $\mathbf{w}_{\perp t}$ and $\mathbf{w}_{\perp n}$, which respectively are the tangential and normal components in the sweep plane. The two tangential velocity components, $\mathbf{w}_{\perp t}$ and \mathbf{w}_t are the same on both sides of the shock.

To obtain \mathbf{w}_1 , we write

$$\mathbf{w}_1 = \mathbf{w}_t + \mathbf{w}_{\perp t} + \mathbf{w}_{\perp 1n} \quad (7.11)$$

where

$$\mathbf{w}_{\perp t} = \mathbf{w}_{\perp} - \mathbf{w}_{\perp n} \quad (7.12)$$

$$\mathbf{w}_t = \mathbf{w}_{\infty} - \mathbf{w}_{\perp} \quad (7.13)$$

$$\mathbf{w}_{\perp n} = \frac{2}{\gamma + 1} \frac{1 + [(\gamma - 1)/2]M_{\perp n}^2}{M_{\perp n}^2} \mathbf{w}_{\perp n} \quad (7.14)$$

thereby obtaining

$$\mathbf{w}_1 = \mathbf{w}_{\infty} - \frac{2}{\gamma + 1} \frac{M_{\perp n}^2 - 1}{M_{\perp n}^2} \mathbf{w}_{\perp n} \quad (7.15)$$

Observe that

$$\mathbf{w}_{\infty} = w_{\infty} \hat{\mathbf{i}}_x = a_{\infty} M_{\infty} \hat{\mathbf{i}}_x \quad (7.16)$$

where a is the speed of sound and $\hat{\mathbf{i}}_x, \hat{\mathbf{i}}_y, \hat{\mathbf{i}}_z$, is a Cartesian orthonormal basis. We also have

$$\mathbf{w}_{\perp n} = a_{\infty} M_{\perp n} \hat{\mathbf{n}} \quad (7.17)$$

where $\hat{\mathbf{n}}$ is a unit normal vector to the shock in the downstream direction, i.e.,

$$\hat{\mathbf{n}} = \frac{\hat{\mathbf{i}}_x + \cot \beta \hat{\mathbf{i}}_y + \tan \Lambda \hat{\mathbf{i}}_z}{\sqrt{(\csc^2 \beta + \tan^2 \Lambda)}} \quad (7.18)$$

The velocity \mathbf{w}_1 is obtained by combining Equations (7.15) to (7.18).

$$\begin{aligned}
w_1 = a_\infty & \left\{ \left[M_\infty - \frac{2}{\gamma + 1} \frac{M_{\perp n}^2 - 1}{M_{\perp n} \sqrt{(\csc^2 \beta + \tan^2 \Lambda)}} \right] \hat{t}_x \right. \\
& + \frac{2}{\gamma + 1} \frac{M_{\perp n}^2 - 1}{M_{\perp n} \sqrt{(\csc^2 \beta + \tan^2 \Lambda)}} \\
& \left. \times (\cot \beta \hat{t}_y + \tan \Lambda \hat{t}_z) \right\}
\end{aligned} \tag{7.19}$$

and its magnitude is then

$$\begin{aligned}
w_1 = a_\infty & \left[M_\infty^2 - \frac{4}{\gamma + 1} \frac{(M_{\perp n}^2 - 1)M_\infty}{M_{\perp n} \sqrt{(\csc^2 \beta + \tan^2 \Lambda)}} \right. \\
& \left. + \frac{4}{(\gamma + 1)^2} \frac{(M_{\perp n}^2 - 1)^2}{M_{\perp n}^2} \right]^{\frac{1}{2}}
\end{aligned} \tag{7.20}$$

Hence, M_1 is given by

$$M_1 = \frac{w_1}{a_1} = \left(\frac{\left\{ \left(\frac{\gamma + 1}{2} \right) M_\infty M_{\perp n} \right\}^2 - \xi + (M_{\perp n}^2 - 1)^2}{\left\{ 1 + \left(\frac{\gamma - 1}{2} \right) M_{\perp n}^2 \right\} \left[\gamma M_{\perp n}^2 - \left(\frac{\gamma - 1}{2} \right) \right]} \right)^{\frac{1}{2}} \tag{7.21}$$

where

$$\xi = \frac{(\gamma + 1)(M_{\perp n}^2 - 1)M_\infty M_{\perp n}}{\sqrt{(\csc^2 \beta + \tan^2 \Lambda)}} \tag{7.22}$$

and

$$\frac{a_1}{a_\infty} = \left(\frac{T_1}{T_\infty} \right)^{\frac{1}{2}} = \frac{2}{\gamma + 1} \frac{\left\{ 1 + \left(\frac{\gamma - 1}{2} \right) M_{\perp n}^2 \right\}^{\frac{1}{2}} \left\{ \gamma M_{\perp n}^2 - \left(\frac{\gamma - 1}{2} \right) \right\}^{\frac{1}{2}}}{M_{\perp n}} \tag{7.23}$$

is utilised. Equation (7.21) is an explicit relation for M_1 in terms of known quantities.

With the foregoing relations, the orientation of \mathbf{w}_1 with respect to the x, y, z coordinate system is readily obtained as direction cosines

$$\cos \alpha_x = \frac{\mathbf{w}_1}{w_1} \uparrow_x \quad (7.24)$$

$$\cos \alpha_y = \frac{\mathbf{w}_1}{w_1} \uparrow_y \quad (7.25)$$

$$\cos \alpha_z = \frac{\mathbf{w}_1}{w_1} \uparrow_z \quad (7.26)$$

where α_x is the angle between \mathbf{w}_∞ and \mathbf{w}_1 .

Appendix C

Analytical Calculations for Run 280

Introduction

The analytical calculations for Run 280 will be presented in three parts.

- i. Upstream flow conditions
- ii. Downstream flow conditions
- iii. Aerodynamic heating

Results will be presented with minimal explanations, as the relevant material was covered in the main body of the dissertation and in Appendix B.

Upstream Flow Conditions

C.1.1 Stagnation conditions

Mean conditions were estimated by inspecting the stagnation pressure plot for Run 280 in the region shortly before rupture of the diaphragm that marked the start of the test flow.

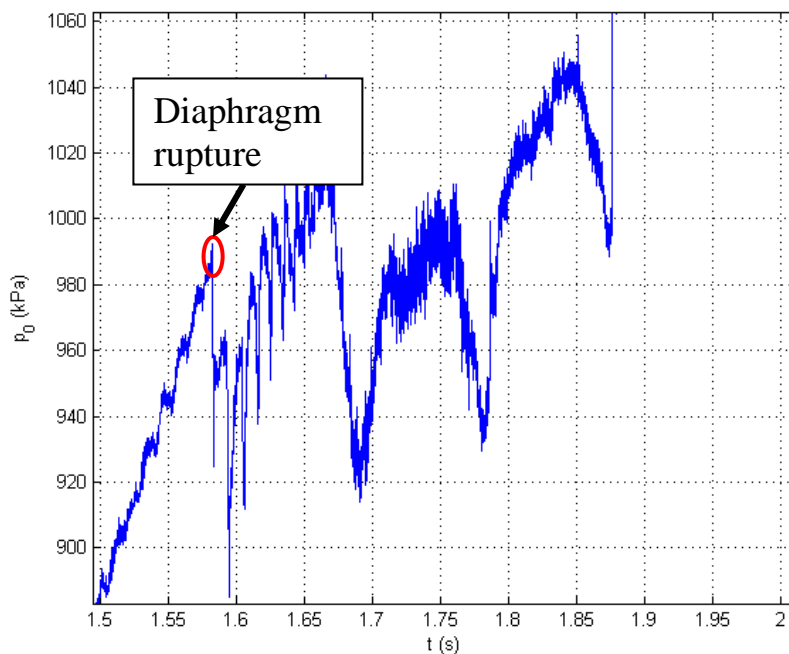


Figure 7.1: Close-up of measurements taken by piezoelectric pressure transducer in nozzle reservoir region

The test gas is compressed slowly at TUSQ, so the process can be considered isentropic. Therefore, the isentropic gas relations (Fox et al. 2010 p.599) can be used in this

instance to determine the flow conditions immediately upstream of the shock wave. Furthermore, the test gas (air) is assumed to be ideal, with a specific heat ratio, $\gamma = 1.4$. Therefore, the ideal gas equation (7.27) can also be used in this analysis.

Consequently, the stagnation temperature was derived from the pressure measurements and the corresponding plot generated.

$$\frac{T_0}{T} = \left(\frac{p_0}{p}\right)^{\frac{\gamma-1}{\gamma}}$$

$$\therefore T_0 = T_{amb} \left[\left(\frac{p_0}{p_{amb}}\right)^{\frac{\gamma-1}{\gamma}} \right]$$

where $T_{amb} = 287.6K$, $p_{amb} = 94.17kPa$, and $p_0 = 989.5 \times 10^3 Pa$

The mean stagnation temperature was also determined by inspecting the relevant plot.

$$\therefore T_0 = 563.2K$$

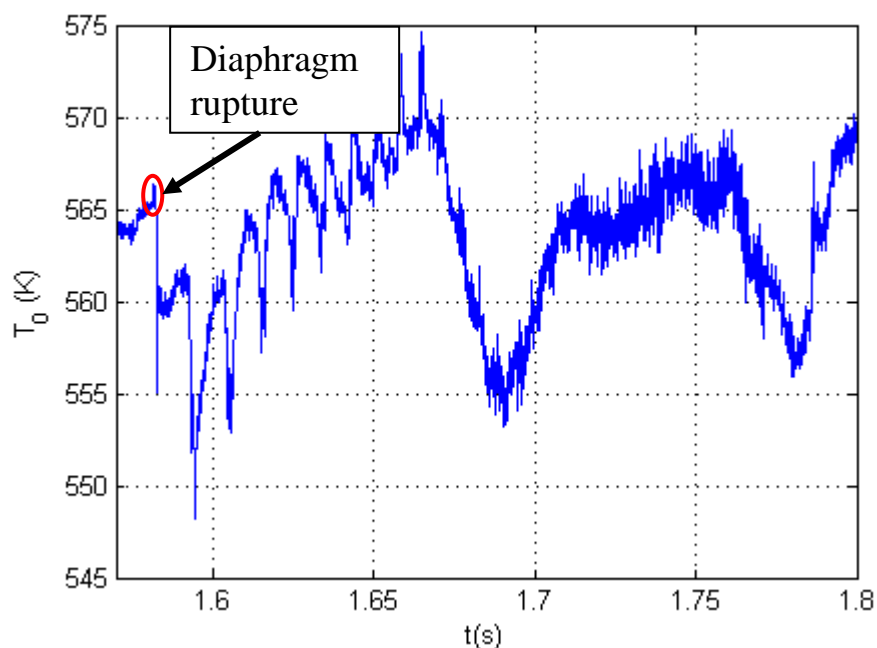


Figure 7.2: Stagnation temperature in the nozzle reservoir section during flow (Run 280)

For a calorically perfect gas, the pressure, density and temperature are related through the ideal gas equation (7.27) The freestream conditions can be determined using the isentropic relations.

$$p = \rho RT \quad (7.27)$$

$$\frac{p_0}{p_1} = \left(1 + \frac{\gamma - 1}{2} M_1^2\right)^{\frac{\gamma}{\gamma - 1}} \quad (7.28)$$

$$\frac{\rho_0}{\rho_1} = \left(1 + \frac{\gamma - 1}{2} M_1^2\right)^{\frac{1}{\gamma - 1}} \quad (7.29)$$

$$\frac{T_0}{T_\infty} = 1 + \frac{\gamma - 1}{2} M_1^2 \quad (7.30)$$

$$M_1 = \frac{u_1}{\sqrt{\gamma RT_1}} \rightarrow u_1 = M_1 \sqrt{\gamma RT_1} \quad (7.31)$$

Using Equation (7.28), the pressure upstream of the shock i.e. freestream temperature, is given by:

$$p_1 = \frac{p_0}{\left(1 + \frac{\gamma - 1}{2} M_1^2\right)^{\frac{\gamma}{\gamma - 1}}} = \frac{989.5 \times 10^3}{\left(1 + \frac{1.4 - 1}{2} 5.85^2\right)^{\frac{1.4}{1.4 - 1}}} = 731.9 Pa$$

The free-stream temperature is given by Equation (7.30).

$$T_1 = \frac{T_0}{\left(1 + \frac{\gamma - 1}{2} M_\infty^2\right)} = \frac{563.2}{\left(1 + \frac{1.4 - 1}{2} 5.85^2\right)} = 71.8 K$$

The free-stream density is determined by rearranging the ideal gas equation (Equation (7.27)).

$$\rho_1 = \frac{p_1}{RT_1} = \frac{731.9}{287 \times 71.8}$$

$$\therefore \rho_1 = 0.0355 \frac{kg}{m^3}$$

Downstream Flow Conditions

The results for the flow conditions immediately downstream of the swept oblique shocks were derived using the method by Emanuel (1992) that was presented in Appendix B.

C.1.2 Assumptions

- Steady, inviscid flow
- Calorically perfect gas $\therefore \gamma = 1.4$
- $\theta = 10^\circ$; wedge/flow deflection angle in the x-y plane
- $\Lambda = 65^\circ$ i.e. the sweep angle for this project is a fixed value, unlike in the original paper (Emanuel 1992), where it is a free parameter.
- All results are for an attached weak solution shock i.e. $\delta = 1$

C.1.3 Mach number, flow deflection angle, and shock wave angle in the sweep plane

$$M_{\perp} = M_{\infty} \cos \Lambda \quad (7.32)$$

$$\therefore M_{\perp} = 5.85 \cos 65^\circ = 2.472$$

$$\theta_{\perp} = \tan^{-1} \left(\frac{\tan \theta}{\cos \Lambda} \right) \quad (7.33)$$

$$\therefore \theta_{\perp} = \tan^{-1} \left(\frac{\tan 10^\circ}{\cos 65^\circ} \right) = 22.65^\circ$$

$$\beta_{\perp} = \tan^{-1} \left\{ \frac{M_{\perp}^2 - 1 + 2\lambda \cos[(4\pi\delta + \cos^{-1} \chi)/3]}{3 \left(1 + \frac{\gamma-1}{2} M_{\perp}^2 \right) \tan \theta_{\perp}} \right\} \quad (7.34)$$

where

$$\lambda = \left[(M_{\perp}^2 - 1) - 3 \left(1 + \frac{\gamma-1}{2} M_{\perp}^2 \right) \left(1 + \frac{\gamma+1}{2} M_{\perp}^2 \right) \tan^2 \theta_{\perp} \right]^{\frac{1}{2}} \quad (7.35)$$

$$\chi = \frac{1}{\lambda^3} \left[(M_{\perp}^2 - 1)^3 - 9 \left(1 + \frac{\gamma-1}{2} M_{\perp}^2 \right) \right. \\ \left. \times \left(1 + \frac{\gamma-1}{2} M_{\perp}^2 + \frac{\gamma+1}{4} M_{\perp}^4 \right) \tan^2 \theta_{\perp} \right] \quad (7.36)$$

Substituting known values into (7.35)

$$\lambda = \left[(2.472^2 - 1) - 3 \left(1 + \frac{1.4 - 1}{2} 2.472^2 \right) \left(1 + \frac{1.4 + 1}{2} 2.472^2 \right) \tan^2 22.65 \right]^{\frac{1}{2}}$$

$$\therefore \lambda = 4.057$$

$$\chi = \frac{1}{4.057^3} \left[(2.472^2 - 1)^3 - 9 \left(1 + \frac{\gamma - 1}{2} 2.472^2 \right) \right. \\ \left. \times \left(1 + \frac{\gamma - 1}{2} 2.472^2 + \frac{\gamma + 1}{4} 2.472^4 \right) \tan^2 22.65 \right]$$

$$\therefore \chi = 0.7160$$

$$\beta_{\perp} = \tan^{-1} \left\{ \frac{2.472^2 - 1 + 2(4.057) \cos[(4\pi(1) + \cos^{-1} 0.7160)/3]}{3 \left(1 + \frac{\gamma - 1}{2} 2.472^2 \right) \tan 22.65} \right\}$$

$$\therefore \beta_{\perp} = 46.96^{\circ}$$

For an attached shock, $|\chi| \leq 1$, while $\delta = 0$ for a strong solution shock and $\delta = 1$ for the weak solution.

The shock wave angle in the x, y plane then is

$$\beta = \tan^{-1}(\cos \Lambda \tan \beta_{\perp}) \quad (7.37)$$

$$\beta = \tan^{-1}(\cos 65^{\circ} \tan 46.96)$$

$$\therefore \beta = 24.35^{\circ}$$

The normal component of the upstream Mach number in the sweep plane is given by:

$$M_{\perp n} = M_{\perp} \sin \beta_{\perp} \quad (7.38)$$

$$M_{\perp n} = 2.472 \sin 46.96$$

$$\therefore M_{\perp n} = 1.807$$

while its downstream counterpart is

$$M_{\perp 2n} = \left\{ \frac{1 + [(\gamma - 1)/2]M_{\perp n}^2}{\gamma M_{\perp n}^2 - (\gamma - 1)/2} \right\}^{\frac{1}{2}} \quad (7.39)$$

$$M_{\perp 2n} = \left\{ \frac{1 + \left[\frac{(1.4 - 1)}{2} \right] (1.807)^2}{(1.4)(1.807)^2 - \frac{(1.4 - 1)}{2}} \right\}^{\frac{1}{2}}$$

$$\therefore M_{\perp 2n} = 0.6150$$

The Mach number component downstream of the shock in the sweep plane is

$$M_{\perp 2} = \frac{M_{\perp 2n}}{\sin(\beta_{\perp} - \theta_{\perp})} \quad (7.40)$$

$$M_{\perp 2} = \frac{0.6150}{\sin(46.96 - 22.65)}$$

$$\therefore M_{\perp 2} = 1.494$$

The local speed of sound upstream of the shock is:

$$a_1 = \sqrt{\gamma RT_1} \quad (7.41)$$

$$a_1 = \sqrt{1.4 \times 287 \times 71.8}$$

$$\therefore a_1 = 169.8 \frac{m}{s}$$

The velocity components immediately downstream of the shock wave can be determined from the following relation by Emanuel (1992)

$$\mathbf{w}_2 = a_1 \left\{ \left[M_1 - \frac{2}{\gamma + 1} \frac{M_{\perp n}^2 - 1}{M_{\perp n} \sqrt{(\csc^2 \beta + \tan^2 \Lambda)}} \right] \hat{\uparrow}_x + \frac{2}{\gamma + 1} \frac{M_{\perp n}^2 - 1}{M_{\perp n} \sqrt{(\csc^2 \beta + \tan^2 \Lambda)}} \times (\cot \beta \hat{\uparrow}_y + \tan \Lambda \hat{\uparrow}_z) \right\} \quad (7.42)$$

The velocity components are

$$u_{2x} = a_1 \left(M_1 - \frac{2}{\gamma + 1} \frac{M_{1n}^2 - 1}{M_{1n} \sqrt{(\csc^2 \beta + \tan^2 \Lambda)}} \right) \quad (7.43)$$

$$u_{2x} = 170.3 \left(5.85 - \frac{2}{1.4 + 1} \frac{1.807^2 - 1}{1.807 \sqrt{(\csc^2 24.35 + \tan^2 65)}} \right)$$

$$\therefore u_{2x} = 938.8 \frac{m}{s}$$

$$u_{2y} = a_1 \left(\frac{2}{\gamma + 1} \frac{\cot \beta (M_{1n}^2 - 1)}{M_{1n} \sqrt{(\csc^2 \beta + \tan^2 \Lambda)}} \right) \quad (7.44)$$

$$u_{2y} = 170.3 \left(\left(\frac{2}{1.4 + 1} \right) \frac{\cot 24.35 (1.807^2 - 1)}{1.807 \sqrt{(\csc^2 24.35 + \tan^2 65)}} \right)$$

$$\therefore u_{2y} = 121.1 \frac{m}{s}$$

$$u_{2z} = a_1 \left(\frac{2}{\gamma + 1} \frac{\tan \Lambda (M_{1n}^2 - 1)}{M_{1n} \sqrt{(\csc^2 \beta + \tan^2 \Lambda)}} \right) \quad (7.45)$$

$$u_{2z} = 170.3 \left(\left(\frac{2}{1.4 + 1} \right) \frac{\tan 65 (1.807^2 - 1)}{1.807 \sqrt{(\csc^2 24.35 + \tan^2 65)}} \right)$$

$$\therefore u_{2z} = 117.5 \frac{m}{s}$$

The magnitude of the downstream velocity is then

$$u_2 = \sqrt{u_{2x}^2 + u_{2y}^2 + u_{2z}^2} \quad (7.46)$$

$$u_2 = \sqrt{938.8^2 + 121.1^2 + 117.5^2}$$

$$\therefore u_2 = 953.8 \frac{m}{s}$$

The oblique shock relations (Fox et al. 2010 pp.670-671) will now be used to determine the other flow properties downstream of the shock, namely pressure, temperature and density.

Pressure ratio

$$\frac{p_2}{p_1} = \frac{2\gamma}{\gamma + 1} M_{\perp n}^2 - \frac{\gamma - 1}{\gamma + 1} \quad (7.47)$$

$$\begin{aligned} \frac{p_2}{p_1} &= \frac{2(1.4)}{1.4 + 1} 1.807^2 - \frac{1.4 - 1}{1.4 + 1} \\ &\therefore \frac{p_2}{p_1} = 3.643 \end{aligned}$$

Density ratio

$$\frac{\rho_2}{\rho_1} = \frac{\left(\frac{\gamma + 1}{2}\right) M_{\perp n}^2}{1 + \left(\frac{\gamma - 1}{2}\right) M_{\perp n}^2} \quad (7.48)$$

$$\begin{aligned} \frac{\rho_2}{\rho_1} &= \frac{\left(\frac{1.4 + 1}{2}\right) 1.807^2}{1 + \left(\frac{1.4 - 1}{2}\right) 1.807^2} \\ &\therefore \frac{\rho_2}{\rho_1} = 2.370 \end{aligned}$$

Temperature ratio

$$\frac{T_2}{T_1} = \frac{\left(1 + \left[\frac{\gamma - 1}{2}\right] M_{\perp n}^2\right) \left(\gamma M_{\perp n}^2 - \left[\frac{\gamma - 1}{2}\right]\right)}{\left(\frac{\gamma + 1}{2}\right)^2 M_{\perp n}^2} \quad (7.49)$$

$$\begin{aligned} \frac{T_2}{T_1} &= \frac{\left(1 + \left[\frac{1.4 - 1}{2}\right] 1.807^2\right) \left(1.4(1.807)^2 - \left[\frac{1.4 - 1}{2}\right]\right)}{\left(\frac{1.4 + 1}{2}\right)^2 1.807^2} \\ &\therefore \frac{T_2}{T_1} = 1.537 \end{aligned}$$

Finally, the flow conditions immediately downstream of the oblique shock wave can be calculated.

Density

$$\rho_2 = \rho_1 \times 2.37 \quad (7.50)$$

$$\rho_2 = 0.0355 \times 2.37$$

$$\therefore \rho_2 = 0.0842 \frac{kg}{m^3}$$

Temperature

$$T_2 = T_1 \times 1.537 \tag{7.51}$$

$$T_2 = 71.8 \times 1.537$$

$$\therefore T_2 = 110.3K$$

Pressure

$$p_2 = p_1 \times 3.643 \tag{7.52}$$

$$p_2 = 731.9 \times 3.643$$

$$\therefore p_2 = 2666Pa = 2.666kPa$$

The local speed of sound downstream of the shock

$$a_2 = \sqrt{\gamma RT_2} \tag{7.53}$$

$$a_2 = \sqrt{1.4 \times 287 \times 110.3}$$

$$\therefore a_2 = 210.6 \frac{m}{s}$$

Downstream Mach number

$$M_2 = \frac{u_2}{a_2} \tag{7.54}$$

$$M_2 = \frac{953.8}{210.6}$$

$$\therefore M_2 = 4.53$$

Summary of Flow Conditions

Table 7.1: Summary of flow conditions

Property	Upstream	Downstream
Pressure	731.9Pa	2666Pa
Temperature	71.8K	110.3K
Density	$0.0355 \frac{kg}{m^3}$	$0.0842 \frac{kg}{m^3}$
Flow velocity	$993.3 \frac{m}{s}$	$953.8 \frac{m}{s}$
Local speed of sound	$169.8 \frac{m}{s}$	$210.6 \frac{m}{s}$
Mach number	5.85	4.53

Aerodynamic Heating

Because inviscid flow has been assumed, the flow conditions calculated in the previous section are therefore the boundary layer edge conditions that will be used in the following aerodynamic heating equation (Anderson 2006 p.298):

$$q_w = \rho_e u_e C_H (h_{aw} - h_w)$$

Firstly, the absolute viscosity coefficient needs to be calculated in order to determine the local Reynolds number. The downstream absolute viscosity coefficient can be calculated from Sutherland's Law (Anderson 2006 p.292). This law is accurate for air over a range of several thousand degrees and is certainly appropriate for the current calculations.

$$\frac{\mu_2}{\mu_{ref}} = \left(\frac{T}{T_{ref}} \right)^{\frac{3}{2}} \frac{T_{ref} + S}{T + S} \quad (7.55)$$

For air, the reference values are

$$T_{ref} = 288K$$

$$\mu_{ref} = 1.789 \times 10^{-5} \frac{kg}{ms}$$

$$S = 110K$$

$$T = T_2 = 110.3K$$

The viscosity coefficient immediately through the shock wave is

$$\mu_2 = (1.789 \times 10^{-5}) \left[\left(\frac{110.3}{288} \right)^{\frac{3}{2}} \left(\frac{288 + 110}{110.3 + 110} \right) \right]$$

$$\therefore \mu_2 = 7.663 \times 10^{-6} \frac{kg}{ms}$$

Taking the flow conditions calculated in the previous section:

$$\rho_e = \rho_2 = 0.0842 \frac{kg}{m^3}$$

$$u_e = u_2 = 953.8 \frac{m}{s}$$

$$T_e = T_2 = 110.3K$$

$$\mu_e = \mu_2 = 7.663 \times 10^{-6} \frac{kg}{ms}$$

The wall temperature is the peak value measured with the surface junction thermocouple during the test flow

$$T_w = 301K$$

The wall temperature to boundary layer edge temperature ratio is

$$\frac{T_w}{T_e} = \frac{301}{110.3} = 2.73$$

In order to calculate the flat-plate Stanton number, the wall to boundary layer edge temperature ratio and the ordinate in Figure 6.12 in Anderson (2006 p. 297) need to be located and determined.

$$C_H \sqrt{Re_x} = 0.34$$

The next step is to calculate the local Reynolds number (Re_x), which involves estimating the distance, x . The method to achieve this was described in Section 3.2.4.

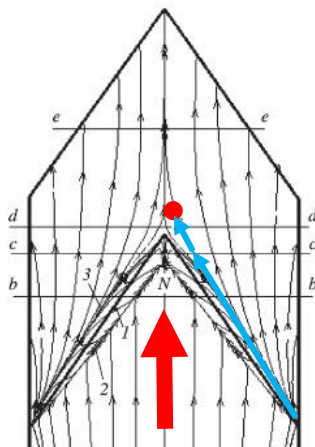


Figure 7.3 Flow pattern at Mach 6 with flow direction indicated by the red arrow (Goukko and Mazhul 2013)

Using the method described in Chapter 3, the straight-line segments of the streamline from the leading edge to the thermocouple junction (indicated by the red dot) is

$$x = 170 \times 10^{-3} m$$

The flow properties immediately downstream from the shock wave (ρ_e, u_e, T_e) were calculated in the previous section and will be used to determine the local Reynolds number (Re_x).

$$Re_x = \frac{\rho_e u_e x}{\mu_e} \tag{7.56}$$

$$\therefore Re_x = \frac{(0.0842)(953.8)(170 \times 10^{-3})}{7.663 \times 10^{-6}} = 1.782 \times 10^6$$

Finally, the Stanton Number (C_H) is given by

$$C_H = \frac{C_H \sqrt{Re_x}}{\sqrt{Re_x}} = \frac{0.34}{\sqrt{1.782 \times 10^6}} = 2.547 \times 10^{-4} \quad (7.57)$$

The specific heat capacity at constant pressure can be estimated with the following relation (Anderson 2006 p.305).

$$c_p = \frac{7R}{2} = \frac{7 \times 287}{2} \quad (7.58)$$

$$\therefore c_p = 1004.5 \frac{J}{kgK}$$

The enthalpy at the boundary layer edge

$$h_e = c_p T_e = 1004.5 \times 110.3 \quad (7.59)$$

$$\therefore h_e = 1.108 \times 10^5 \frac{J}{kg}$$

Total enthalpy

$$h_0 = h_e + \frac{u_e^2}{2} = 1.108 \times 10^5 + \frac{953.8^2}{2} \quad (7.60)$$

$$\therefore h_0 = 5.657 \times 10^5 \frac{J}{kg}$$

The recovery factor (r) accounts for the viscous dissipation of the high kinetic energy through the viscous boundary layer. For laminar flow, it is (Anderson 2006 p. 299):

$$r = \sqrt{Pr} \quad (7.61)$$

$$\therefore r = \sqrt{0.715} = 0.846$$

Adiabatic wall enthalpy

$$h_{aw} = h_e + r(h_0 - h_e) = 1.108 \times 10^5 + 0.846(5.685 \times 10^5 - 1.108 \times 10^5) \quad (7.62)$$

$$\therefore h_{aw} = 4.955 \times 10^5 \frac{J}{kg}$$

$$h_w = c_p T_w = 1004.5 \times 301 \quad (7.63)$$

$$\therefore h_w = 3.024 \times 10^5 \frac{J}{kg}$$

Finally, the local heat flux can be determined using the aerodynamic heating equation

$$q_w = (0.0842 \times 953.8 \times (2.547 \times 10^{-4})) \times (4.955 \times 10^5 - 3.024 \times 10^5)$$

$$\therefore q_w = 3951 \frac{W}{m^2} = 3.95 \frac{kW}{m^2}$$

Appendix D

Analytical Calculations for Run 285

Introduction

As was the case for Run 280, the analytical calculations for Run 285 will also be presented in three parts.

- iv. Upstream flow conditions
- v. Downstream flow conditions
- vi. Aerodynamic heating

Results will be presented with minimal explanations, as the relevant material was covered in the main body of the dissertation and in Appendix B.

Upstream Flow Conditions

D.1.1 Stagnation conditions

Mean conditions were estimated by inspecting the stagnation pressure and temperature plots for Run 285 in the region shortly before rupture of the diaphragm that marked the start of the test flow.

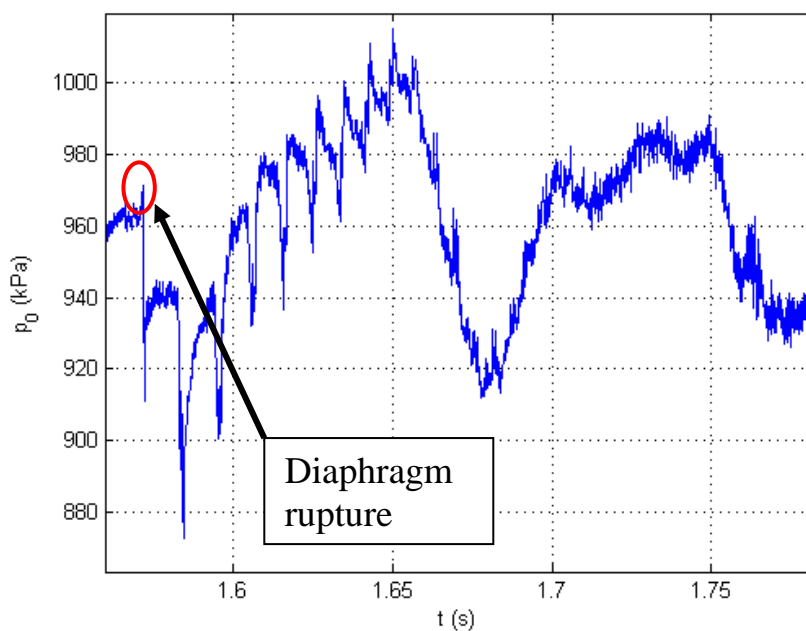


Figure 7.4: Close-up of measurements taken by piezoelectric pressure transducer in nozzle reservoir region during Run 285

The test gas is compressed slowly at TUSQ, so the process can be considered isentropic. Therefore, the isentropic gas relations (Fox et al. 2010 p.599) can be used in this instance to determine the flow conditions immediately upstream of the shock wave.

Furthermore, the test gas (air) is assumed to be ideal, with a specific heat ratio, $\gamma = 1.4$. Therefore, the ideal gas equation (7.27) can also be used in this analysis.

Consequently, the stagnation temperature was derived from the pressure measurements and the corresponding plot generated.

$$\frac{T_0}{T} = \left(\frac{p_0}{p}\right)^{\frac{\gamma-1}{\gamma}}$$

$$\therefore T_0 = T_{amb} \left[\left(\frac{p_0}{p_{amb}}\right)^{\frac{\gamma-1}{\gamma}} \right]$$

where $T_{amb} = 292K$, $p_{amb} = 94.94kPa$, and $p_0 = 940 \times 10^3 Pa$

$$\therefore T_0 = 562K$$

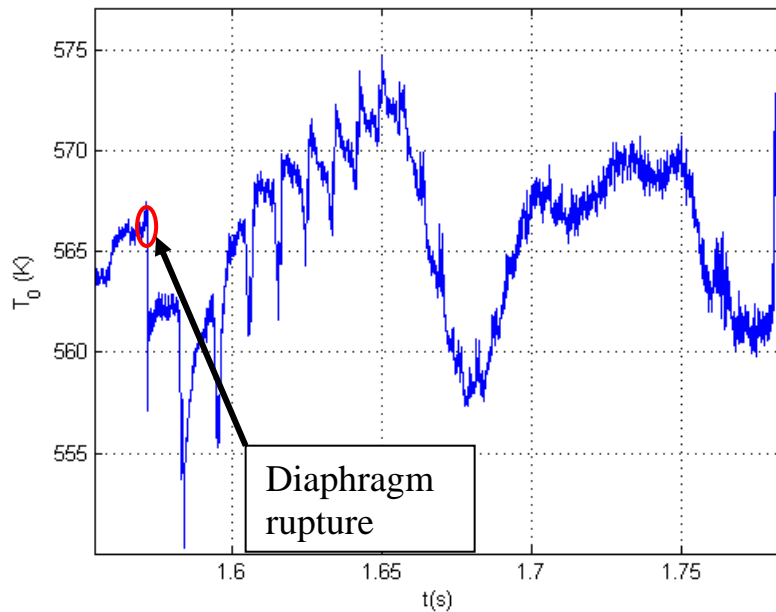


Figure 7.5: Stagnation temperature in nozzle reservoir during Run 285

For a calorically perfect gas, the pressure, density and temperature are related through the ideal gas equation (7.27). The freestream conditions can be determined using the ideal gas isentropic relations and this equation.

$$p = \rho RT \tag{7.64}$$

$$\frac{p_0}{p_1} = \left(1 + \frac{\gamma-1}{2} M_1^2\right)^{\frac{\gamma}{\gamma-1}} \tag{7.65}$$

$$\frac{\rho_0}{\rho_1} = \left(1 + \frac{\gamma - 1}{2} M_1^2\right)^{\frac{1}{\gamma - 1}} \quad (7.66)$$

$$\frac{T_0}{T_1} = 1 + \frac{\gamma - 1}{2} M_1^2 \quad (7.67)$$

$$M_1 = \frac{u_1}{\sqrt{\gamma RT_1}} \rightarrow u_1 = M_1 \sqrt{\gamma RT_1} \quad (7.68)$$

Using Equation (7.28), the pressure upstream of the shock i.e. freestream temperature, is given by:

$$p_1 = \frac{p_0}{\left(1 + \frac{\gamma - 1}{2} M_1^2\right)^{\frac{\gamma}{\gamma - 1}}} = \frac{940 \times 10^3}{\left(1 + \frac{1.4 - 1}{2} 5.85^2\right)^{\frac{1.4}{1.4 - 1}}} = 695.3 Pa$$

The free-stream temperature is given by Equation (7.30).

$$T_1 = \frac{T_0}{\left(1 + \frac{\gamma - 1}{2} M_\infty^2\right)} = \frac{562}{\left(1 + \frac{1.4 - 1}{2} 5.85^2\right)} = 71.6 K$$

The free-stream density is determined by rearranging the ideal gas equation (Equation (7.27)).

$$\rho_1 = \frac{p_1}{RT_1} = \frac{695.3}{287 \times 71.6}$$

$$\therefore \rho_1 = 0.0338 \frac{kg}{m^3}$$

Table 7.2: Summary of flow properties upstream of shock

Property	Symbol	Value
Stagnation pressure	p_0	$940 \times 10^3 Pa$
Stagnation temperature	T_0	$562 K$
Freestream/Upstream pressure	p_1	$695.3 Pa$
Upstream temperature	T_1	$71.6 K$
Upstream density	ρ_1	$0.0338 \frac{kg}{m^3}$

Downstream Flow Conditions

The results for the flow conditions immediately downstream of the swept oblique shocks were derived using the method by Emanuel (1992) that was presented in Appendix B.

The same assumptions per the calculations for Run 280 apply here also for Run 285.

D.1.2 Assumptions

- Steady, inviscid flow
- Calorically perfect gas $\therefore \gamma = 1.4$
- $\theta = 10^\circ$; wedge/flow deflection angle in x-y plane
- $\Lambda = 65^\circ$ i.e. the sweep angle for this project is a fixed value, unlike in the original paper (Emanuel 1992), where it is a free parameter.
- All results are for an attached weak solution shock i.e. $\delta = 1$

D.1.3 Mach number, flow deflection angle and shock wave angle in the sweep plane

The values for the sweep plane that were derived in the previous appendix for Run 280 are the same in Run 285, as the geometry and nominal Mach number for the flow did not change. These values have been summarised in Table 7.3.

Table 7.3: Mach number, flow deflection and shock wave angles for Run 285

Property	Symbol	Value
Mach number in sweep plane	M_{\perp}	2.472
Flow deflection angle in sweep plane	θ_{\perp}	22.65°
Shock wave angle in sweep plane	β_{\perp}	46.96°
Shock wave angle in x-y plane	β	24.35°
Normal component of Mach number in sweep plane	$M_{\perp n}$	1.807
Normal component of downstream Mach number in sweep plane	$M_{\perp 2n}$	0.6150
Downstream Mach number in sweep plane	$M_{\perp 2}$	1.494

The local speed of sound upstream of the shock is:

$$a_1 = \sqrt{\gamma RT_1} \quad (7.69)$$

$$a_1 = \sqrt{1.4 \times 287 \times 71.6}$$

$$\therefore a_1 = 169.7 \frac{m}{s}$$

The velocity components immediately downstream of the shock wave can be determined from the following relation by Emanuel (1992)

$$\mathbf{w}_2 = a_1 \left\{ \left[M_1 - \frac{2}{\gamma + 1} \frac{M_{\perp n}^2 - 1}{M_{\perp n} \sqrt{(\csc^2 \beta + \tan^2 \Lambda)}} \right] \uparrow_x + \frac{2}{\gamma + 1} \frac{M_{\perp n}^2 - 1}{M_{\perp n} \sqrt{(\csc^2 \beta + \tan^2 \Lambda)}} \times (\cot \beta \uparrow_y + \tan \Lambda \uparrow_z) \right\} \quad (7.70)$$

The velocity components are

$$u_{2x} = a_1 \left(M_1 - \frac{2}{\gamma + 1} \frac{M_{\perp n}^2 - 1}{M_{\perp n} \sqrt{(\csc^2 \beta + \tan^2 \Lambda)}} \right) \quad (7.71)$$

$$u_{2x} = 169.7 \left(5.85 - \frac{2}{1.4 + 1} \frac{1.807^2 - 1}{1.807 \sqrt{(\csc^2 24.35 + \tan^2 65)}} \right)$$

$$\therefore u_{2x} = 937.8 \frac{m}{s}$$

$$u_{2y} = a_1 \left(\frac{2}{\gamma + 1} \frac{\cot \beta (M_{\perp n}^2 - 1)}{M_{\perp n} \sqrt{(\csc^2 \beta + \tan^2 \Lambda)}} \right) \quad (7.72)$$

$$u_{2y} = 169.7 \left(\left(\frac{2}{1.4 + 1} \right) \frac{\cot 24.35 (1.807^2 - 1)}{1.807 \sqrt{(\csc^2 24.35 + \tan^2 65)}} \right)$$

$$\therefore u_{2y} = 121.0 \frac{m}{s}$$

$$u_{2z} = a_1 \left(\frac{2}{\gamma + 1} \frac{\tan \Lambda (M_{\perp n}^2 - 1)}{M_{\perp n} \sqrt{(\csc^2 \beta + \tan^2 \Lambda)}} \right) \quad (7.73)$$

$$u_{2z} = 169.7 \left(\left(\frac{2}{1.4 + 1} \right) \frac{\tan 65 (1.807^2 - 1)}{1.807 \sqrt{(\csc^2 24.35 + \tan^2 65)}} \right)$$

$$\therefore u_{2z} = 117.4 \frac{m}{s}$$

The magnitude of the downstream velocity is then

$$u_2 = \sqrt{u_{2x}^2 + u_{2y}^2 + u_{2z}^2} \quad (7.74)$$

$$u_2 = \sqrt{937.8^2 + 121.0^2 + 117.4^2}$$

$$\therefore u_2 = 952.8 \frac{m}{s}$$

The pressure, temperature and density ratios that were determined for Run 280 using the oblique shock relations (Fox et al. 2010 pp. 670-671) also apply here for Run 285.

Pressure ratio

$$\frac{p_2}{p_1} = 3.643 \quad (7.75)$$

Density ratio

$$\frac{\rho_2}{\rho_1} = 2.370 \quad (7.76)$$

Temperature ratio

$$\frac{T_2}{T_1} = 1.537 \quad (7.77)$$

Finally, the flow conditions immediately downstream of the oblique shock wave can be calculated.

Density

$$\rho_2 = \rho_1 \times 2.37 \quad (7.78)$$

$$\rho_2 = 0.0338 \times 2.37$$

$$\therefore \rho_2 = 0.0801 \frac{kg}{m^3}$$

Temperature

$$T_2 = T_1 \times 1.537 \quad (7.79)$$

$$T_2 = 71.64 \times 1.537$$

$$\therefore T_2 = 110.1K$$

Pressure

$$p_2 = p_1 \times 3.643 \quad (7.80)$$

$$p_2 = 695.3 \times 3.643$$

$$\therefore p_2 = 2533Pa = 2.533kPa$$

The local speed of sound downstream of the shock

$$a_2 = \sqrt{\gamma RT_2} \quad (7.81)$$

$$a_2 = \sqrt{1.4 \times 287 \times 110.1}$$

$$\therefore a_2 = 210.3 \frac{m}{s}$$

Downstream Mach number

$$M_2 = \frac{u_2}{a_2} \quad (7.82)$$

$$M_2 = \frac{952.8}{210.3}$$

$$\therefore M_2 = 4.53$$

Summary of Flow Conditions

Property	Upstream	Downstream
Pressure	695.3Pa	2533Pa
Temperature	71.6K	110.1K
Density	0.0338 $\frac{kg}{m^3}$	0.0801 $\frac{kg}{m^3}$
Flow velocity	992.7 $\frac{m}{s}$	952.8 $\frac{m}{s}$
Local speed of sound	169.7 $\frac{m}{s}$	210.3 $\frac{m}{s}$
Mach number	5.85	4.53

Aerodynamic Heating

Because inviscid flow has been assumed, the flow conditions calculated in the previous section are therefore the boundary layer edge conditions. These will be used in the aerodynamic heating equation (Anderson 2006 p. 298)

$$q_w = \rho_e u_e C_H (h_{aw} - h_w)$$

Firstly, the absolute viscosity coefficient needs to be calculated in order to determine the local Reynolds number. The downstream absolute viscosity coefficient can be calculated from Sutherland's Law (Anderson 2006 p. 292). This law is accurate for air over a range of several thousand degrees and is certainly appropriate for the current calculations.

$$\frac{\mu_2}{\mu_{ref}} = \left(\frac{T}{T_{ref}} \right)^{\frac{3}{2}} \frac{T_{ref} + S}{T + S} \quad (7.83)$$

For air, the reference values are

$$T_{ref} = 288K$$

$$\mu_{ref} = 1.789 \times 10^{-5} \frac{kg}{ms}$$

$$S = 110K$$

$$T = T_2 = 110.4K$$

The viscosity coefficient immediately through the shock wave is

$$\mu_2 = (1.789 \times 10^{-5}) \left[\left(\frac{110.1}{288} \right)^{\frac{3}{2}} \left(\frac{288 + 110}{110.1 + 110} \right) \right]$$

$$\therefore \mu_2 = 7.647 \times 10^{-6} \frac{kg}{ms}$$

Taking the flow conditions calculated in the previous section:

$$\rho_e = \rho_2 = 0.0801 \frac{kg}{m^3}$$

$$u_e = u_2 = 952.8 \frac{m}{s}$$

$$T_e = T_2 = 110.1K$$

$$\mu_e = \mu_2 = 7.647 \times 10^{-6} \frac{kg}{ms}$$

The wall temperature is the peak value measured with the surface junction thermocouple during the test flow

$$T_w = 298.5K$$

The wall temperature to boundary layer edge temperature ratio is

$$\frac{T_w}{T_e} = \frac{298.5}{110.1} = 2.71$$

In order to calculate the flat-plate Stanton number, the wall to boundary layer edge temperature ratio and the ordinate in Figure 6.12 in Anderson (2006 p. 297) need to be located and determined.

$$C_H \sqrt{Re_x} = 0.34$$

The next step is to calculate the local Reynolds number. The method and value for x have been described and determined earlier. This value is the same as that used for the analysis of Run 280, because the same thermocouple was used for the surface temperature measurements.

$$x = 170 \times 10^{-3}m$$

The flow properties immediately downstream from the shock wave (ρ_e, u_e, T_e) were calculated in the previous section and will be used to determine the local Reynolds number (Re_x) .

$$Re_x = \frac{\rho_e u_e x}{\mu_e} \tag{7.84}$$

$$\therefore Re_x = \frac{(0.0801)(952.8)(170 \times 10^{-3})}{7.647 \times 10^{-6}} = 1.698 \times 10^6$$

Finally, the Stanton Number (C_H) is given by

$$C_H = \frac{C_H \sqrt{Re_x}}{\sqrt{Re_x}} = \frac{0.34}{\sqrt{3.995 \times 10^5}} = 2.6093 \times 10^{-4} \quad (7.85)$$

The specific heat capacity at constant pressure can be estimated with the following relation (Anderson 2006 p.305) and was calculated in Appendix C.

$$c_p = \frac{7R}{2} = \frac{7 \times 287}{2} \quad (7.86)$$

$$\therefore c_p = 1004.5 \frac{J}{kgK}$$

The enthalpy at the boundary layer edge

$$h_e = c_p T_e = 1004.5 \times 110.1 \quad (7.87)$$

$$\therefore h_e = 1.106 \times 10^5 \frac{J}{kg}$$

Total enthalpy

$$h_0 = h_e + \frac{u_e^2}{2} = 1.106 \times 10^5 + \frac{952.8^2}{2} \quad (7.88)$$

$$\therefore h_0 = 5.645 \times 10^5 \frac{J}{kg}$$

The recovery factor (r) accounts for the viscous dissipation of the high kinetic energy through the viscous boundary layer. For laminar flow, it is (Anderson 2006 p. 299):

$$r = \sqrt{Pr} \quad (7.89)$$

$$\therefore r = \sqrt{0.715} = 0.846$$

Adiabatic wall enthalpy

$$h_{aw} = h_e + r(h_0 - h_e) = 1.106 \times 10^5 + 0.846(5.645 \times 10^5 - 1.106 \times 10^5) \quad (7.90)$$

$$\therefore h_{aw} = 4.944 \times 10^5 \frac{J}{kg}$$

$$h_w = c_p T_w = 1004.5 \times 301 \quad (7.91)$$

$$\therefore h_w = 2.998 \times 10^5 \frac{J}{kg}$$

Finally, the local heat flux can be determined using the aerodynamic heating equation

$$q_w = (0.0801 \times 952.8 \times (2.6093 \times 10^{-4})) \times (4.944 \times 10^5 - 2.998 \times 10^5)$$

$$\therefore q_w = 3878 \frac{kW}{m^2} = 3.88 \frac{kW}{m^2}$$

Appendix E

MATLAB Code

Analytical Calculations for Run 280

```

ENG4112 Analytical calculations for Run 280
% Version 1 by J Fuata (28/10/14)

% References
% [1] Anderson, JD 2006, Hypersonic and High-temperature Gas
% Dynamics, 2edn, American Institute of Aeronautics and Astronautics,
% Reston, Virginia
% [2] Emmanuel, G, 1992, Oblique Shock Wave with Sweep,
% Shock Waves, Volume 2, Number 1, pp.13-18

% Aims
% 1. Calculate upstream flow conditions prior to flow
% 2. Calculate flow conditions immediately downstream of
% oblique shock wave with sweep on experimental model
% 3. Calculate local heat flux at thermocouple location

clc
clear all
close all

% Inputs
M1 = 5.85; % Nominal free-stream Mach number
theta = 10; % Flow deflection angle in x-y plane
gamma = 1.4; % Ratio of specific heats for air
lambda = 65; % Sweep angle (degrees)
degtorad = pi/180; % Convert degrees to radians
radtodeg = 1/degtorad; % Convert radians to degrees
delta = 1; % For attached weak oblique shock wave
T0 = 563.2; % Mean stagnation temperature prior to flow(K)
R = 287; % Gas constant for air (J/kgK)
p0 = 989.5e3; % Mean stagnation pressure prior to flow (kPa)
mu_ref = 1.789e-5; % Reference dynamic/absolute viscosity coefficient
[1]
Tref = 288; % Reference temperature for Sutherland's Law [1]
SA = 110; % Constant for Sutherland's Law [1]

% Free-stream conditions
% Pressure
g1 = (gamma-1)*0.5;
g2 = gamma/(gamma-1);
p1 = p0/((1+(g1*M1^2))^g2);
% Temperature
T1=T0/((1+((0.5*(gamma-1))*M1^2)));

rho1 = p1/(R*T1); % Upstream density (kg/m^3) from ideal gas equation

% Mach number and deflection angle in sweep plane
M90 = M1.*cos(degtorad.*lambda);
theta90 =
radtodeg*atan((tan(degtorad*theta))./(cos(degtorad.*lambda)));

% Shock wave angle in the sweep plane
% Lambda
lam1 = (M90.^2 - 1).^2;
lam2 = (1 + (((gamma - 1)/2).*M90.^2));
lam3 = (1 + (((gamma + 1)/2).*M90.^2));
lam4 = 3.*lam2.*lam3.*(tan(degtorad.*theta90)).^2;
lam5 = sqrt(lam1 - lam4); % Same as lam calculated later
% chi
chi1 = (M90.^2 - 1).^3;

```

```

chi2 = (1 + (((gamma-1)/2).*M90.^2));
chi3 = (1 + (((gamma-1)/2).*M90.^2) + (((gamma+1)/4).*M90.^4));
chi4 = 9.*chi2.*chi3.*(tan(degtorad.*theta90).^2));
chi5 = (1./(lam5.^3)).*(chi1-chi4);
% Beta (shock wave angle)
beta1 = (M90.^2);
beta2 = (((4*pi*delta) + (acos(chi5)))/3);
beta3 = (2.*lam5.*cos(beta2));
beta4 = beta1 - 1 + beta3;
beta5 = (((gamma-1)/2).*M90.^2);
beta6 = tan(degtorad.*theta90);
beta7 = 3.*(1+beta5).*beta6;
beta90 = radtodeg*(atan(beta4/beta7));

% Shock wave angle in the x-y plane
beta = radtodeg*atan((cos(lambda*degtorad))*(tan(beta90*degtorad)));

% Normal component of the upstream Mach number in the sweep plane
M90n = M90*sin(beta90*degtorad);

% Normal component of downstream Mach number in the sweep plane
p1b = 1+ ((0.5*(gamma-1)).*M90n.^2);
p2b = (gamma.*M90n.^2)-(0.5*(gamma-1));
M90_1n = sqrt(p1b/p2b);

% Mach number component downstream of the shock in the sweep plane
M90_1 = M90_1n ./ sin(degtorad.*(beta90-theta90));

% Speed of sound upstream of oblique shock wave with sweep
a1 = sqrt(gamma*R*(T1));

% Vector components of flow downstream of oblique shock wave

v2x = a1.*(M1 - (2./(gamma+1)).*(M90n.^2 - 1)./(M90n.*sqrt(
((csc(degtorad.*beta)).^2) + ((tan(degtorad.*lambda)).^2))
)));

v2y = a1 .* (((2./(gamma+1)).*(M90n.^2 - 1)./(M90n.*sqrt(
((csc(degtorad.*beta)).^2) + ((tan(degtorad.*lambda)).^2))
).*
(cot(degtorad.*beta))
)));

v2z = a1 .* (((2./(gamma+1)).*(M90n.^2 - 1)./(M90n.*sqrt(
((csc(degtorad.*beta)).^2) + ((tan(degtorad.*lambda)).^2))
).*
(tan(degtorad.*lambda))
)));

% Magnitude of v2
v2mag = sqrt(v2x.^2 + v2y.^2 + (v2z.^2));

% Equation (13) from [2]
epsilon = ((gamma+1).*M90n.^2-
1).*M90n*M1)/(sqrt(((1./(sin(degtorad.*beta))).^2) +
((tan(degtorad.*lambda)).^2)));

% Sonic speed ratio (a2/a1)
sonic_ratio = ((2./(gamma+1)) .* (sqrt(1+((gamma-1).*0.5).*M90n.^2))
.* (sqrt((gamma.*M90n.^2) - (0.5*(gamma-1)))))./M90n;

% Downstream sonic speed, a2
a2 = a1.*sonic_ratio;

```

```

% Downstream Mach number, M2, based on combination of Eq. (9) to (12)
[2]
% Components of downstream Mach number, M2
M2x = v2x./a2;
M2y = v2y./a2;
M2z = v2z./a2;

% Magnitude of M2
M2 = sqrt(M2x.^2 + M2y.^2 + M2z.^2);

% Angles between upstream and downstream flow
alpha_x = radtodeg.*acos((v2x./v2mag));
d_alphax = sprintf('Alpha_x = %3.3gdeg%/n',alpha_x);
disp(d_alphax)

alpha_y = radtodeg.*acos((v2y./v2mag));
d_alphay = sprintf('Alpha_y = %3.3gdeg%/n',alpha_y);
disp(d_alphay)

alpha_z = radtodeg.*acos((v2z./v2mag));
d_alphaz = sprintf('Alpha_z = %3.3gdeg%/n',alpha_z);
disp(d_alphaz)

% Calculate ratios
% Pressure
pratio = (2/(gamma+1))*( (gamma*M90n^2) - (0.5*(gamma-1)) );
% Density
rhoratio = ((gamma + 1) * M90n^2)/(2 + ((gamma-1)*M90n^2));
% Temperature
Tratio = pratio/rhoratio;

% Calculate post-shock flow conditions
p2 = pratio*p1; % Pressure (Pa)
rho2 = rhoratio*rho1; % Density (kg/m^3)
T2 = (Tratio*T1); % Temperature degC
T2K=T2+273; % K

% Calculate mu from T2
muA = mu_ref*(T2/Tref)^(3/2) * (Tref+SA)/(T2+SA);

%%%%%%%%%%%%%%%%%%%%%%%%%%%%%%%%%%%%%%%%%%%%%%%%%%%%%%%%%%%%%%%%%%%%%%%% CONVECTIVE AERODYNAMIC HEATING %%%%%%%%%
Tw = 28; % Maximum surface temperature from Run 280 (deg C)
TwK=Tw+273; % Tw in K
TwTeratio = TwK/T2;
ChRex = 0.34; % (Figure 6.12 Anderson 2006, p.297)
x=170e-3; % Straight-line distance from leading edge to thermocouple
Pr=0.715; % Prandtl number
r=sqrt(Pr); % Recovery factor for laminar hypersonic flow over a flat
plate
%(Eq 6.90 Anderson 2006, p.299)
cp = (7/2)*R; % Specific heat capacity at constant pressure

% Reynolds number at x
Rex = (rho2*v2mag*x)/muA; % Use mu based on Sutherland's Law
% Flat plate Stanton number
Ch = ChRex/sqrt(Rex);

he = cp*T2; % Enthalpy at boundary layer edge
h0 = he + (v2mag^2)*0.5; % Total enthalpy in outside boundary layer
haw = he + r*(h0-he); % Adiabatic wall enthalpy
hw = cp*TwK; % Wall enthalpy

```

```
% Adiabatic wall temperature
Taw=cp*haw;
% Calculate heat flux, qw
qw = rho2*v2mag*Ch*(haw-hw); % Surface heat flux (W/m^2)
qw=qw/1000; % kW/m^2

% Display results
d_theta90 = sprintf('Deflection angle in the sweep plane is theta90 =
%3.5gdeg',theta90);
d_beta90 = sprintf('Shock wave angle in the sweep plane is beta90 =
%3.5gdeg',beta90);
d_beta = sprintf('Shock wave angle in the x-y plane is beta =
%3.5gdeg',beta);
d_M2 = sprintf('Downstream mach number in sweep plane, M2 =
%3.3g',M2);
d_v2mag = sprintf('Magnitude of flow velocity downstream of oblique
shock in sweep plane, v2 = %3.4gm/s',v2mag);
d_pratio=sprintf('Pressure ratio = %3.4g%/n',pratio);
d_rhoratio=sprintf('Denchity ratio = %3.4g%/n',rhoratio);
d_Tratio=sprintf('Temperature ratio = %3.4g%/n',Tratio);
d_muA = sprintf('Absolute viscosity muA = %3.4g kg/ms%/n',muA);
d_qw=sprintf('qw is %3.4gkW/m^2',qw);

disp(d_theta90)
disp(d_beta90)
disp(d_beta)
disp(d_M2)
disp(d_v2mag)
disp(d_pratio)
disp(d_rhoratio)
disp(d_Tratio)
disp(d_muA)
disp(d_qw)
```

Analytical Calculations for Run 285

```

% ENG4112 Analytical calculations for Run 285
% Version 1 by J Fuata (26/10/14)

% References
% [1] Anderson, JD 2006, Hypersonic and High-temperature Gas
% Dynamics, 2edn, American Institute of Aeronautics and Astronautics,
% Reston, Virginia
% [2] Emmanuel, G, 1992, Oblique Shock Wave with Sweep,
% Shock Waves, Volume 2, Number 1, pp.13-18

% Aims
% 1. Calculate upstream flow conditions prior to flow
% 2. Calculate flow conditions immediately downstream of
% oblique shock wave with sweep on experimental model
% 3. Calculate local heat flux at thermocouple location

clc
clear all
close all

% Inputs
M1 = 5.85; % Nominal free-stream Mach number
theta = 10; % Flow deflection angle in x-y plane
gamma = 1.4; % Ratio of specific heats for air
lambda = 65; % Sweep angle (degrees)
degtorad = pi/180; % Convert degrees to radians
radtodeg = 1/degtorad; % Convert radians to degrees
delta = 1; % For attached weak oblique shock wave
T0 = 562; % Mean stagnation temperature prior to test flow (K)
R = 287; % Gas constant for air (J/kgK)
p0 = 940e3; % Mean stagnation pressure prior to test flow (Pa)
mu_ref = 1.789e-5; % Reference absolute viscochity coefficient [1]
Tref = 288; % Reference temperature for Sutherland's Law [1]
SA = 110; % Constant for Sutherland's Law [1]

% Calculate freestream pressure and temperature from isentropic
relations
% Pressure
p1 = p0/((1+((gamma-1)*0.5)*M1^2))^(gamma/(gamma-1));
% Temperature
T1=T0/((1+((0.5*(gamma-1))*M1^2)));
rho1 = p1/(R*T1); % Upstream density (kg/m^3) from ideal gas equation

%%%%%%%%%% Oblique shock wave with sweep method [2] %%%%%%%%%%%
% Mach number and deflection angle in sweep plane
M90 = M1.*cos(degtorad.*lambda);
theta90 =
radtodeg*atan((tan(degtorad*theta))./(cos(degtorad.*lambda)));

% Shock wave angle in the sweep plane
% Lambda
lam1 = (M90.^2 - 1).^2;
lam2 = (1 + (((gamma - 1)/2).*M90.^2));
lam3 = (1 + (((gamma + 1)/2).*M90.^2));
lam4 = 3.*lam2.*lam3.*(tan(degtorad.*theta90)).^2;
lam5 = sqrt(lam1 - lam4);
% Chi
chi1 = (M90.^2 - 1).^3;
chi2 = (1 + (((gamma-1)/2).*M90.^2));

```



```

chi3 = (1 + (((gamma-1)/2).*M90.^2) + (((gamma+1)/4).*M90.^4));
chi4 = 9.*chi2.*chi3.*((tan(degtorad.*theta90).^2));
chi5 = (1./(lam5.^3)).*(chi1-chi4);
% Beta (shock wave angle)
beta1 = (M90.^2);
beta2 = (((4*pi*delta) + (acos(chi5)))/3);
beta3 = (2.*lam5.*cos(beta2));
beta4 = beta1 - 1 + beta3;
beta5 = (((gamma-1)/2).*M90.^2);
beta6 = tan(degtorad.*theta90);
beta7 = 3.*(1+beta5).*beta6;
beta90 = radtodeg*(atan(beta4/beta7));

% Shock wave angle in the x-y plane
beta = radtodeg*atan((cos(lambda*degtorad))*(tan(beta90*degtorad)));

% Normal component of the upstream Mach number in the sweep plane
M90n = M90*sin(beta90*degtorad);

% Normal component of downstream Mach number in the sweep plane
p1b = 1+ ((0.5*(gamma-1)).*M90n.^2);
p2b = (gamma.*M90n.^2)-(0.5*(gamma-1));
M90_1n = sqrt(p1b/p2b);

% Mach number component downstream of the shock in the sweep plane
M90_1 = M90_1n ./ sin(degtorad.*(beta90-theta90));

% Speed of sound upstream of oblique shock wave with sweep
a1 = sqrt(gamma*R*(T1));

% Vector components of flow downstream of oblique shock wave
v2x = a1.*(M1 - ((2./(gamma+1)).*(M90n.^2 - 1)./(M90n.*sqrt(
((csc(degtorad.*beta)).^2) + ((tan(degtorad.*lambda)).^2)))));
v2y = a1.*(((2./(gamma+1)).*(M90n.^2 - 1)./(M90n.*sqrt(
((csc(degtorad.*beta)).^2) + ((tan(degtorad.*lambda)).^2)))).*
(cot(degtorad.*beta))));
v2z = a1.*(((2./(gamma+1)).*(M90n.^2 - 1)./(M90n.*sqrt(
((csc(degtorad.*beta)).^2) + ((tan(degtorad.*lambda)).^2)))).*
(tan(degtorad.*lambda))));

% Magnitude of v2
v2mag = sqrt(v2x.^2 + v2y.^2 + (v2z.^2));

% Equation (13) from [2]
epsilon = ((gamma+1).*M90n.^2-
1).*M90n*M1./sqrt(((1./(sin(degtorad.*beta))).^2) +
((tan(degtorad.*lambda)).^2));
% Sonic speed ratio (a2/a1)
sonic_ratio = ((2./(gamma+1)).*(sqrt(1+((gamma-1).*0.5).*M90n.^2))
.*(sqrt((gamma.*M90n.^2) - (0.5*(gamma-1)))))./M90n;

% Downstream sonic speed, a2
a2 = a1.*sonic_ratio;

% Downstream Mach number, M2, based on combination of Eq. (9) to (12)
[2]
% Components of downstream Mach number, M2
M2x = v2x./a2;
M2y = v2y./a2;
M2z = v2z./a2;

```

```

% Magnitude of M2
M2 = sqrt(M2x.^2 + M2y.^2 + M2z.^2);

% Angles between upstream and downstream flow
alpha_x = radtodeg.*acos((v2x./v2mag));
d_alphax = sprintf('Alpha_x = %3.3gdeg%/n',alpha_x);
disp(d_alphax)

alpha_y = radtodeg.*acos((v2y./v2mag));
d_alphay = sprintf('Alpha_y = %3.3gdeg%/n',alpha_y);
disp(d_alphay)

alpha_z = radtodeg.*acos((v2z./v2mag));
d_alphaz = sprintf('Alpha_z = %3.3gdeg%/n',alpha_z);
disp(d_alphaz)

% Calculate ratios
% Pressure
pratio = (2/(gamma+1))*( (gamma*M90n^2) - (0.5*(gamma-1)) );
% Density
rhoratio = ((gamma + 1) * M90n^2)/(2 + ((gamma-1)*M90n^2));
% Temperature
Tratio = pratio/rhoratio;

% Calculate post-shock flow conditions
p2 = pratio*p1; % Pressure (Pa)
rho2 = rhoratio*rho1; % Density (kg/m^3)
T2 = (Tratio*T1); % Temperature (degC)
T2K=T2+273; % K

% Calculate mu from T2
muA = mu_ref*(T2/Tref)^(3/2) * (Tref+SA)/(T2+SA);

%%%%%%%%%%%%%%%%%%%%%%%%%%%%%%%%%%%%%%%%%%%%%%%%%%%%%%%%%%%%%%%%%%%%%%%%%% CONVECTIVE AERODYNAMIC HEATING %%%%%%%%%%%%%%%%%%%%%%%%%%%%%%%%%%%%%%%%%%%%%%%%%%%%%%%%%%%%%%%%%%%%%%%%%%%
Tw = 25.5; % Maximum surface temperature from Run 280 (deg C)
TwK=Tw+273; % Tw in K
TwTeratio = TwK/T2;
ChRex = 0.34; % (Figure 6.12 Anderson 2006, p.297)
x=170e-3; % Straight-line distance from leading edge to thermocouple
Pr=0.715; % Prandtl number
r=sqrt(Pr); % Recovery factor for laminar hypersonic flow over a flat
plate
%(Eq 6.90 Anderson 2006, p.299)
cp = (7/2)*R; % Specific heat capacity at constant pressure

% Reynolds number at x
Rex = (rho2*v2mag*x)/muA; % Use mu based on Sutherland's Law
% Flat plate Stanton number
Ch = ChRex/sqrt(Rex);

he = cp*T2; % Enthalpy at boundary layer edge
h0 = he + (v2mag^2)*0.5; % Total enthalpy in outside boundary layer
haw = he + r*(h0-he); % Adiabatic wall enthalpy
hw = cp*TwK; % Wall enthalpy

% Adiabatic wall temperature
Taw=cp*haw;
% Calculate heat flux, qw
qw = rho2*v2mag*Ch*(haw-hw); % Surface heat flux (W/m^2)
qw=qw/1000; % kW/m^2

```

```
% Display results
d_theta90 = sprintf('Deflection angle in the sweep plane is theta90 =
%3.5gdeg',theta90);
d_beta90 = sprintf('Shock wave angle in the sweep plane is beta90 =
%3.5gdeg',beta90);
d_beta = sprintf('Shock wave angle in the x-y plane is beta =
%3.5gdeg',beta);
d_M2 = sprintf('Downstream mach number in sweep plane, M2 =
%3.3g',M2);
d_v2mag = sprintf('Magnitude of flow velocity downstream of oblique
shock in sweep plane, v2 = %3.4gm/s',v2mag);
d_pratio=sprintf('Pressure ratio = %3.4g%/n',pratio);
d_rhoratio=sprintf('Denchity ratio = %3.4g%/n',rhoratio);
d_Tratio=sprintf('Temperature ratio = %3.4g%/n',Tratio);
d_muA = sprintf('Absolute viscosity muA = %3.4g kg/ms%/n',muA);
d_qw=sprintf('qw is %3.4gkW/m^2',qw);

disp(d_theta90)
disp(d_beta90)
disp(d_beta)
disp(d_M2)
disp(d_v2mag)
disp(d_pratio)
disp(d_rhoratio)
disp(d_Tratio)
disp(d_muA)
disp(d_qw)
```

Impulse Response Function Based on Semi-Infinite Wall Model (Oldfield 2000)

```

function [h,shift]=desT2qsiimp1(fs,np,rrck,test)
%function [h,shift]=desT2qsiimp1(fs,np,rrck,test)
% Version 1 MLG Oldfield 9/5/99.%
% Designs (des) filter to convert surface temperature T
% to heat transfer rate q (T2q) for a semi-infinite substrate (si)
% gives impulse response (imp) h.
%
%outputs:
% h np-point filter impulse response row vector
% shift positive time shift required to time align filtered
signal.
%inputs:
% fs Sampling frequency
% np number of Temperature sample points in data to be
processed.
% rrck sqrt(rho*c*k), the thermal product of the semi-infinite
substrate
% test = 1 tests the filter, = 0 doesn't.
%
%typical call: [h,shift]=desT2qsiimp1(2e5,1000,480,1);
%
% To use the impulse response filter to convert an np-point
temperature column vector T into
% a heat transfer vector q, make sure initial temperature T(1)= 0,
then call
% q = fftfilt(h,T);
% Then shift the result (shift will be -1): q(1:np-1)=q(2:np);
% Note: fftfilt uses Fast Fourier Transforms and is much faster for
large numbers of points
% than using filter or conv functions.
% The design process may get long for more than 1000 points, but the
use is very quick!

%Method:
% A step function in q, q1 gives a parabola in T1, in terms of time
t:
%
% 
$$T1(t) = (1/(\text{sqrt}(\text{rho}*\text{c}*k)))*(2/\text{sqrt}(\text{pi})) * t^{(1/2)}$$

%
% The first np points of the T to q impulse response is obtained by
deconvoluting
% a known q1 and T1 pair in sampled form, using the Matlab filter
function
% (you need the signal processing toolbox).
% In z-transform form, the process is
% 
$$Q(z) = H(z)T(z)$$
, where H(z) is the z transform of the impulse
response h(t).
% Then, for a known pair of Q1(z) and T1(z) sequences,
% 
$$H(z) = Q1(z)/T1(z)$$
.
% This can be evaluated by the Matlab function h =
filter(q1,T1,imp), where imp is the
% discrete impulse sequence [1 0 0 0 ...]'
% The 16 figure accuracy of Matlab makes this possible!
% Since q1(1)= 0 it is necessary to timeshift by one point before
deconvoluting.

```

```

%
% After the impulse response h is obtained and stored as a row
vector,
% it can be used efficiently to compute q1 from a measured sampled T
signal:
%     q = fftfilt(h,T);
%
% If test = 1, it plots the approximations and tests the model in
time with a
% sqrt(t) trace which should give a step response.
%
%Copyright MLG Oldfield 1999. Not to be used, sold, copied or
published without permission.

%Generate shifted time vector
t = (1/fs:(1/fs):np/fs)';
lt = length(t);

%Note shift for output of function
shift = -1;

%Generate a unit step in q1
q1 = ones(np,1);

%calculate shifted T1(t) corresponding to step of q1
% T1(s) = (1/s)*(1/(sqrt(rho*c*k))sqrt(s))
%         = (1/(sqrt(rho*c*k)))*(s^3/2)
%Taking inverse transform:
% T1(t) = (1/(sqrt(rho*c*k)))*(2/sqrt(pi))*t^(1/2)

T1 = (1/rrck)*(2/sqrt(pi))*t.^(1/2);

%Deconvolute to get impulse response for T to q
delta = [1;zeros((np-1),1)]; %Impulse function
h = filter(q1,T1,delta);

% the filter is now designed, so return if we don't need to test it.
if test ~= 1
    return
end

% OK, so let's test it.
%
%Time testing

figure(1); %plot impulse response

ns = min([50 np]);
stem(h(1:ns));

title('First 50 points Impulse response of impulse filter.')

xlabel('Sample number')
ylabel('Impulse response')
grid
pause

% Time test vector. Max size - 1e5!
nt=np;
if nt > 1e5;
    warning('only up to 1e5 time steps allowed')

```

```

    nt=1e5;
end

%Generate non-shifted time vector
t2 = (0:(1/fs):(nt-1)/fs)';
lt2 = length(t2);

%calculate input of T2(t) to give step of q2
%   T2(s) = (1/s)*(1/(sqrt(rho*c*k)*sqrt(s)))
%           = (1/(sqrt(rho*c*k)))*(s^3/2)
%Taking inverse transform:
%   T2(t) = (1/(sqrt(rho*c*k)))*(2/sqrt(pi))*t2^(1/2)

T2 = (1/rrck)*(2/sqrt(pi))*t2.^(1/2);

figure(2)
plot(t2,T2)
title('Time test signal to ideally give step q output.')

xlabel('time (s)')
ylabel('Temperature test signal T2')

grid
pause

figure(3)
plot(sqrt(t2),T2)
title('Time test signal to ideally give step q output.')

xlabel('sqrt(time) (s)^1/2')
ylabel('Temperature test signal T2')

grid
pause

%Now filter T2(t) to turn it into q2(t)

q2 = fftfilt(h,T2);

q2 = q2(2:nt); %shift it
t2 = t2(1:nt-1);

figure(4);
semilogx(t2,q2-1, '.');
grid
%ax =axis;
%axis([ax(1:2) 0.99 1.01]);
title('Time test output of T2q impulse filter (ideal = 0.0).')

xlabel('Log time (s)')
ylabel('q deviation from 1.0')
%whos

```

Stagnation Pressure and Temperature Plotting for Run 280

```

% ENG4112
% Version 1 by D Buttsworth and J Fuata (08/07/14)
% Version 2 by J Fuata (20/10/14)

% References
% [1] Oldfield, MLG 2000, OUEL Report 2233/2000: Guide to Impulse
Response
% Heat Transfer Signal Processing Version 2, University of Oxford,
% Department of Engineering Science, Oxford, UK
% [2] Productive Plastics 2014, Perspex for glazing, Productive
Plastics,
% Perth, Western Australia, viewed 17 October 2014,
%
<http://www.productiveplastics.com.au/uploaded/files/client_added/Mitc
hell%20Plastics%20-%20Glazing_236eng.pdf>

% Aim: To plot stagnation pressure and temperature and surface
temperature
% for Run 280

close all
clc
clear all

% Load data from acquisition system
load run280.txt

% Input parameters
t=run280(:,1); % Time
v0=run280(:,2); % Channel 0: Piezo-electric pressure transducer
readings (V)
v3=run280(:,5); % Channel 3: Thermocouple readings of wall
temperature (V)
Tamb=14.6; % Recorded ambient temperature on model surface (degC)
Tamb=Tamb+273; % Convert ambient temperature to K
s0=800; % Piezo-electric pressure transducer sensitivity; 800kPa/V
s3=100; % Type K thermocouple sensitivity 100mV/degC; 1V = 100degC
patm=94.17; % Ambient/atmospheric pressure (kPa) in TUSQ
rho = 1190; % Density of perspex (kg/m^3)
k = 0.189; % Thermal conductivity of perspex (W/mK)
c = 1465.4; % Specific heat capacity of perspex (J/kgK)

v0 = v0 - mean(v0(1:1000)); % Normalise the voltage data from
% the mean of recorded voltage prior to flow
Tw = v3*s3; % Convert thermocouple voltage values into
temperature(degC)
TwK=Tw+273; % Convert thermocouple temperature to K
p0=patm+(v0*s0); % Convert transducer voltage values into pascals
% and add atmospheric pressure (kPa)

T0=Tamb*((p0/patm).^(0.4/1.4)); % Stagnation temperature in nozzle
% reservoir Apply low-pass Butterworth filter for wall temperature
values
[B,A]=butter(2,0.1);
Twf=filter(B,A,Tw); % Apply filter to wall temperature values, Tw
%Twf=Twf-mean(Twf(101:1201)); Twf(1:100)=Twf(101:200);

```

```

%%%
% Calculate mean stagnation conditions
p0mean = mean(mean(p0(15813:15825)));
T0mean = mean(mean(T0(15813:15825)));

%%% Apply Semi-infinite Wall Data Reduction Model (Oldfield
2000)%%
% This filter converts a surface temperature T to a heat transfer rate
q
% for a semi-infinite substrate. It also gives an impulse response, h
fs=10e3; % Sampling rate (Hz)
np=1000; % Number of sample points
rrck=sqrt(rho*c*k); % Thermal product of perspex
test=0;
[h,shift]=desT2qsiimp1(fs,np,rrck,test);
q=fftfilt(h,Twf); % Convert the measured wall temperatures (Tw) to q

% Apply low-pass Butterworth filter for wall heat flux values
[B,A]=butter(2,0.01);
qf=filter(B,A,q); % Units: W/m^2
qf=qf/1000; % kW/m^2

%%%%%%%%%%%%%%%%%%%%%%%%%%%%%%%%%%%%%%%%%%%%%%%%%%%%%%%%%%%%%%%%%%%%%%%% Plot results
%%%%%%%%%%%%%%%%%%%%%%%%%%%%%%%%%%%%%%%%%%%%%%%%%%%%%%%%%%%%%%%%%%%%%%%%
% Stagnation Pressure
figure(1)
plot(t,p0),xlabel('t (s)'),ylabel('p_0 (kPa)'),grid on

% Zoom into test time to determine mean stagnation pressure
figure(2)
plot(t,p0), xlabel('t (s)'),ylabel('p_0 (kPa)');
axis([1.5812 1.5824 800 1100]), grid on

% Stagnation temperature
figure(3)
plot(t,T0),xlabel('t(s)'),ylabel('T_0 (K)'),grid on

% Zoom into test time to determine mean stagnation temperature
figure(4)
plot(t,T0),xlabel('t(s)'),ylabel('T_0 (K)');
axis([1.5812 1.5824 545 575]), grid on

% Surface temperature
figure(5)
plot(t,Twf),xlabel('t(s)'),ylabel('T_w ( ^oC )');
axis([0 max(t) 10 30]),grid on

% Zoom into filtered surface temperature
figure(6)
TwfK=Twf+273; % Convert Twf to K
plot(t,TwfK),xlabel('t (s)'),ylabel('T_w (K)');
axis([1.57 1.8 285 305]), grid on

% Surface heat flux (filtered)
figure(7)
plot(t,qf),xlabel('t (s)'),ylabel('q_w (kW/m^2)');
axis([1.57 1.8 10 40]),grid on

```


Stagnation Pressure and Temperature Plotting for Run 285

```

% ENG4112
% Version 1 by D Buttsworth and J Fuata (23/09/14)
% Version 2 by J Fuata (20/10/14)

% References
% [1] Oldfield, MLG 2000, OUEL Report 2233/2000: Guide to
% Impulse Response Heat Transfer Signal Processing Version 2,
% University of
% Oxford, Department of Engineering Science, Oxford, UK
% [2] Productive Plastics 2014, Perspex for glazing, Productive
% Plastics,
% Perth, Western Australia, viewed 17 October 2014,
%
% <http://www.productiveplastics.com.au/uploaded/files/client_added/Mitc
% hell%20Plastics%20-%20Glazing_236eng.pdf>

% Aim: To plot stagnation pressure and temperature and surface
% temperature
% for Run 285

close all
clc
clear all

% Load data from acquisition system
load run285.txt

% Input parameters
t=run285(:,1); % Time
v0=run285(:,2); % Channel 0: Piezo-electric pressure transducer
readings (V)
v3=run285(:,3); % Channel 3: Thermocouple readings of wall
temperature (V)
Tamb=18.6; % Recorded ambient temperature on model surface (degC)
Tamb=Tamb+273; % Convert ambient temperature to K
s0=800; % Piezo-electric pressure transducer sensitivity; 800kPa/V
s3=100; % Type K thermocouple sensitivity 100mV/degC; 1V = 100degC
patm=94.94; % Ambient/atmospheric pressure (kPa) in TUSQ
rho = 1190; % Density of perspex (kg/m^3)
k = 0.189; % Thermal conductivity of perspex (W/mK)
c = 1465.4; % Specific heat capacity of perspex (J/kgK)

v0 = v0 - mean(v0(1:1000)); % Normalise the voltage data from
% the mean of recorded voltage prior to flow
Tw = v3*s3; % Convert thermocouple voltage values into
temperature(degC)
TwK=Tw+273; % Convert thermocouple temperature to K
p0=patm+(v0*s0); % Convert transducer voltage values into pascals
% and add atmospheric pressure (kPa)

T0=Tamb*((p0/patm).^(0.4/1.4)); % Stagnation temperature in nozzle
% reservoir Apply low-pass Butterworth filter for wall temperature
values
[B,A]=butter(2,0.1);
Twf=filter(B,A,Tw); % Apply filter to wall temperature values, Tw
%Twf=Twf-mean(Twf(101:1201)); Twf(1:100)=Twf(101:200);

```

```

% Calculate mean stagnation conditions
p0mean = mean(mean(p0(15813:15825)));
T0mean = mean(mean(T0(15813:15825)));
    %%% Apply Semi-infinite Wall Data Reduction Model (Oldfield
2000)%%
% This filter converts a surface temperature T to a heat transfer rate
q
% for a semi-infinite substrate. It also gives an impulse response, h
fs=10e3; % Sampling rate (Hz)
np=1000; % Number of sample points
rrck=sqrt(rho*c*k); % Thermal product of perspex
test=0;
[h,shift]=desT2qsiimp1(fs,np,rrck,test);
q=fftfilt(h,Twf); % Convert the measured wall temperatures (Tw) to q

% Apply low-pass Butterworth filter for wall heat flux values
[B,A]=butter(2,0.01);
qf=filter(B,A,q); % Units: W/m^2
qf=qf/1000; % kW/m^2

%%%%%%%%%%%%%%%%%%%%%%%%%%%%%%%%%%%%%%%%%%%%%%%%%%%%%%%%%%%%%%%%%%%%%%%% Plot results
%%%%%%%%%%%%%%%%%%%%%%%%%%%%%%%%%%%%%%%%%%%%%%%%%%%%%%%%%%%%%%%%%%%%%%%%
% Stagnation Pressure
figure(1)
plot(t,p0),xlabel('t (s)'),ylabel('p_0 (kPa)'),grid on

% Zoom into test time to determine mean stagnation pressure
figure(2)
plot(t,p0), xlabel('t (s)'),ylabel('p_0 (kPa)');
axis([1.5812 1.5824 800 1100]), grid on

% Stagnation temperature
figure(3)
plot(t,T0),xlabel('t(s)'),ylabel('T_0 (K)'),grid on

% Zoom into test time to determine mean stagnation temperature
figure(4)
plot(t,T0),xlabel('t(s)'),ylabel('T_0 (K)');
axis([1.5812 1.5824 545 575]), grid on

% Surface temperature
figure(5)
plot(t,Twf),xlabel('t(s)'),ylabel('T_w ( ^oC )');
axis([0 max(t) 10 30]),grid on

% Zoom into filtered surface temperature
figure(6)
TwfK=Twf+273; % Convert Twf to K
plot(t,TwfK),xlabel('t (s)'),ylabel('T_w (K)');
axis([1.57 1.8 285 305]), grid on

% Surface heat flux (filtered)
figure(7)
plot(t,qf),xlabel('t (s)'),ylabel('q_w (kW/m^2)');
axis([1.57 1.8 10 40]),grid on

```

Calibration Sequences

```

% ENG4112
% Version 1 by D Buttsworth & J Fuata (26/09/14)
% Version 2 by J Fuata (16/10/14)

% Aim
% (1) To create three sets of calibration polynomial coefficients
% (2) To plot each calibration curve

clear all
close all
clc

%%%%%%%%%%%%%%%%%%%%%%%%%%%%%%%%%%%%%%%%%%%%%%%%%%%%%%%%%%%%%%%%%%%%%%%% Calibration Sequence 1 %%%%%%%%%
T1 = (30:5:75)'; % Calibration temperature range
n = length(T1);
cnts1 = zeros(size(T1));

for i = 1:n,
    fname = ['..\285zip\CAL_285\cal285_',int2str(T1(i)),'.png'];
    A = imread(fname);
    colormap('gray');
    image(A/1000)
    cnts1(i) = mean(mean(A(343:345,86:88))); % Thermocouple junction
location
    title(['Temperature = ',int2str(T1(i)), 'degC'])
    pause
end

p1 = polyfit(cnts1,T1,2); % Generate calibration polynomial
coefficients
cnts_fits1 = [20:50]*1e3; % Number of photons counted/detected
T_fits1 = polyval(p1,cnts_fits1); % Convert counts into temperature
(degC)

%%%%%%%%%%%%%%%%%%%%%%%%%%%%%%%%%%%%%%%%%%%%%%%%%%%%%%%%%%%%%%%%%%%%%%%% Calibration Sequence 2 %%%%%%%%%
T2 = [23.5, 25:1:37]'; % Calibration temperature range
n = length(T2);
cnts2 = zeros(size(T2));

for i = 1:n,
    fname = ['..\285zip\CAL_285\cal285a_',int2str(T2(i)*10),'.png'];
    A = imread(fname);
    colormap('gray');
    image(A/1000)
    cnts2(i) = mean(mean(A(343:345,86:88))); % Thermocouple junction
location
    title(['Temperature = ',int2str(T2(i)), 'degC'])
    pause
end

p2 = polyfit(cnts2,T2,2); % Generate calibration polynomial
coefficients
cnts_fits2 = [25:35]*1e3; % Number of photons counted/detected
T_fits2 = polyval(p2,cnts_fits2); % Convert counts into temperature
(degC)

```

```

%%%%%%%%%%%%%%%%%%%%%%%%%%%%%%%%%%%%%%%%%%%%%%%%%%%%%%%%%%%%%%%%%%%%%%%% Calibration Sequence 3 %%%%%%%%%%%%%%%%%%%%%%%%%%%%%%%%%%%%%%%%%%%%%%%%%%%%%%%%%%%%%%%%%%%%%%%%%
T3 = (16.5:0.5:26)'; % Calibration temperature range
n = length(T3);
cnts3 = zeros(size(T3));

for i = 1:n,
    fname = ['..\285zip\CAL_285\cal285b_',int2str(T3(i)*10),'.png'];
    A = imread(fname);
    colormap('gray');
    image(A/1000)
    cnts3(i) = mean(mean(A(343:345,86:88))); % Thermocouple junction
location
    title(['Temperature = ',int2str(T3(i)), 'degC'])
    pause
end

p3 = polyfit(cnts3,T3,2); % Generate calibration polynomial
coefficients
cnts_fits3 = [10:50]*1e3; % Number of photons counted/detected
T_fits3 = polyval(p3,cnts_fits3); % Convert counts into temperature
(degC)

% Save calibration polynomial coefficients for use in other files
save cal_poly p1
save cal_polyB p2
save cal_polyC p3

figure(2)
subplot(3,1,1)
plot(cnts1,T1,'o',cnts_fits1,T_fits1)
title('Calibration Curve - Sequence 1')
xlabel('Number of Counts'), ylabel('Temperature ( ^o C )')
axis([20e3 45e3 0 80]), grid on

subplot(3,1,2)
plot(cnts2,T2,'o',cnts_fits2,T_fits2)
title('Calibration Curve - Sequence 2')
xlabel('Number of Counts'), ylabel('Temperature ( ^o C )')
axis([25e3 31e3 0 40]), grid on

subplot(3,1,3)
plot(cnts3,T3,'o',cnts_fits3,T_fits3)
title('Calibration Curve - Sequence 3')
xlabel('Number of Counts'), ylabel('Temperature ( ^o C )')
axis([26e3 30e3 0 30]), grid on

```

Comparison of Calibrated and Recorded Plots

```

% ENG4112
% Version 1 by D Buttsworth & J Fuata (23/9/14)
% Version 2 by J Fuata (20/10/14)

% Aims
% To plot the following for Run 285
% (1) Surface temperature history
% (2) Calibrated surface temperature history
% (3) Surface heat flux history
% (4) Calibrated surface heat flux history

% [1] Productive Plastics 2014, Perspex for glazing, Productive
Plastics,
% Perth, Western Australia, viewed 17 October 2014,
%
<http://www.productiveplastics.com.au/uploaded/files/client\_added/Mitchell%20Plastics%20-%20Glazing\_236eng.pdf>

clear all
close all
clc

% Import calibration polynomial -- see cal285C.m for details
load cal_polyC

% Import time file (recorded from Run 285 .xvi file)
load time285.txt

% Import recorded data
load run285.txt

% Input parameters
t=run285(:,1); % Time (s) from TC#2 file
v0=run285(:,2); % Piezoelectric transducer readings of stagnation
pressure in barrel (V)
v1=run285(:,3); % Thermocouple readings of surface temperature (V)
Tamb=18.6; % Recorded ambient temperature on model surface (degC)
Tamb=Tamb+273; % Convert ambient temperature to K
s0=800; % Piezo-electric pressure transducer sensitivity; 800kPa/V
s1=100; % K-type thermocouple sensitivity 10mV/degC. Therefore, 1V =
100degC
patm=94.17; % Atmospheric pressure (kPa) in TUSQ
rho = 1190; % Density of perspex (kg/m^3) [1]
k = 0.189; % Thermal conductivity of perspex (W/mK) [1]
c = 1465.4; % Specific heat capacity of perspex (J/kgK) [1]

%%%%%%%%%%%%%%%%%%%%%%%%%%%%%%%%%%%%%%%%%%%%%%%%%%%%%%%%%%%%%%%%%%%%%%%%% RECORDED DATA
%%%%%%%%%%%%%%%%%%%%%%%%%%%%%%%%%%%%%%%%%%%%%%%%%%%%%%%%%%%%%%%%%%%%%%%%%
% Convert text file information into temperature and pressure values
v0 = v0 - mean(v0(1:1000));
Tw = v1*s1; % Convert into temperature values (degC)
p0=patm+(v0*s0); % Convert into pascals and add atmospheric pressure
(kPa)

% Apply low-pass Butterworth filter for surface temperature values
[B,A]=butter(2,0.025);

```

```

Twf=filter(B,A,Tw); % Filter surface temperature values, Tw
%Twf=Twf-mean(Twf(101:1201)); Twf(1:100)=Twf(101:200);

% Convert surface temperature T to a heat transfer rate q for a
% semi-infinite substrate. It also gives an impulse response, h
fs=10e3; % Sampling rate (Hz)
np=1000; % Number of sample points
rrck=sqrt(rho*c*k); % Thermal product of perspex
test=0;
[h,shift]=desT2qsiimp1(fs,np,rrck,test);
q1=fftfilt(h,Twf); % Convert thermocouple readings (Tw) to q

% Apply low-pass Butterworth filter to heat flux near TC#2 values
[B1,A1]=butter(2,0.01);
qf1=filter(B1,A1,q1); % W/m^2
qf1=qf1/1000; % kW/m^2

%%%%%%%%%%%%%%%%%%%%%%%%%%%%%%%%%%%%%%%%%%%%%%%%%%%%%%%%%%%%%%%%%%%%%%%% IR CAMERA
CALIBRATION%%%%%%%%%%%%%%%%%%%%%%%%%%%%%%%%%%%%%%%%%%%%%%%%%%%%%%%%%%%%%%%%%%%%%%%%
% Read video file 'run285.avi'
runObj = VideoReader('run285.avi');
get(runObj)

% Retrieve info about the video file
nFrames = runObj.NumberOfFrames; % Number of frames in video
vidHeight = runObj.Height; % Number of pixels in vertical (x)
direction
vidWidth = runObj.Width; % Number of pixels in horizontal (z)
direction
timeget = get(runObj, 'Duration'); % Duration of video (s)
rate = get(runObj, 'FrameRate'); % Capture rate (fps)

imin = 120; % First frame from run285 images
imax = 200; % Last frame from run285 images

% Work out time interval between frames
delta = timeget/nFrames;
% Work out time duration of 200 frames in s
timelength = imax*delta;
% Create time array based on the number of frames analysed
timerange = 0.2474:delta:(timelength-delta)+0.2474;
% 0.2474s is the difference between approximate start times of the
flow in
% the calibrated and recorded data via TC

% Create new time axis to plot against calibrated qw
t3 = timerange(119:200);

% crotch at about: 395,203 New values (26/9/14): 420,120
n = 420;
m = 120;

fname = ['..\285zip\RUN_285\run285_fr',int2str(imin),'.png'];
Aref = imread(fname);
linedataref = Aref(n,:);
col_array = [1:400];
row_array = [1:512];

for i = imin:imax,
    fname = ['..\285zip\RUN_285\run285_fr',int2str(i),'.png'];
    Afr1 = imread(fname);

```

```

    cnt_TCloc(i) = mean(mean(Afr1(343:345,86:88))); % Location of
thermocouple junction
end

% Convert counts for thermocouple to temperature values
T_TCloc = polyval(p,double(cnt_TCloc));
T_TCloc = T_TCloc + 33;
t285 = zeros(size(T_TCloc));
t285(120:end) = time285;

% Convert calibrated surface temperature T to a heat transfer rate q
for a
% semi-infinite substrate. It also gives an impulse response, h
fs2=50; % Sampling rate (Hz)
np2=82; % Number of sample points that will be in T_TCloc1 array
rrck=sqrt(rho*c*k); % Thermal product of perspex
test=0;
[h2,shift2]=desT2qsiimp1(fs2,np2,rrck,test);

q2=fftfilt(h2,T_TCloc(119:200)); % Convert IR calibrated temperature
values to q
[B2,A2]=butter(2,0.295);
qf2=filter(B2,A2,q2); % W/m^2
qf2=qf2/1000; % kW/m^2

%%%%%%%%%%%%% PLOTS %%%%%%%%%%%%%%

figure(1)
plot(t,Twf)
title('Surface temperature (Run 285)');
xlabel('t (s)'), ylabel('T ( ^oC )');
axis([1.57 1.78 18.5 26]);
grid on

figure(2)
plot(timerange,T_TCloc,'-o')
axis([1.57 1.78 0 8])
title('Calibrated surface temperature(Run 285)'), ylabel('T ( ^oC
)'), xlabel('t (s)');
grid on

figure(3)
plot(t,qf1)
title('Surface heat flux (Run 285)', xlabel('t (s)'), ylabel('q_w
(kW/m^2)');
axis([1.57 1.78 18 30]);
grid on

figure(4)
plot(t3,qf2)
title('Calibrated surface heat flux (Run 285)', xlabel('t (s)'),
ylabel('q_w (kW/m^2)');

```

Heat Flux Mapping

```
% ENG4112
% Version 1 by D Buttsworth & J Fuata (26/09/14)
% Version 2 by J Fuata (29/10/14)
% All contour mapping by J Fuata

% [1] Oldfield, MLG 2000, OUEL Report 2233/2000: Guide to Impulse
Response
% Heat Transfer Signal Processing Version 2, University of Oxford,
% Department of Engineering Science, Oxford, UK
% [2] Productive Plastics 2014, Perspex for glazing, Productive Plastics,
% Perth, Western Australia, viewed 17 October 2014,
%
<http://www.productiveplastics.com.au/uploaded/files/client\_added/Mitchel1%20Plastics%20-%20Glazing\_236eng.pdf>

% AIM
% 1. Generate heat flux maps of experimental model for Run 285
% 2. Generate filled contour heat flux maps of model for Run 285

clear all
close all
clc

% Import calibration polynomial
load cal_polyC

% Import time file (recorded from Run 285 .xvi file)
load time285.txt

% Import recorded data
load run285.txt

% Input parameters
t=run285(:,1); % Time (s) from TC#2 file
v0=run285(:,2); % Piezoelectric transducer readings of stagnation
pressure in barrel (V)
v1=run285(:,3); % Channel 1: Thermocouple readings of surface temperature
(V)
Tamb=18.6; % Recorded ambient temperature on model surface (degC)
Tamb=Tamb+273; % Convert ambient temperature to K
s0=800; % Piezo-electric pressure transducer sensitivity; 800kPa/V
s1=100; % K-type thermocouple sensitivity 10mV/degC. Therefore, 1V =
100degC
patm=94.94; % Atmospheric pressure (kPa)
rho = 1190; % Density of perspex (kg/m^3) [2]
k = 0.189; % Thermal conductivity of perspex (W/mK) [2]
c = 1465.4; % Specific heat capacity of perspex (J/kgK) [2]

% Read video file 'run285.avi'
runObj = VideoReader('run285.avi');
get(runObj)
```



```

% Retrieve info about the video file
nFrames = runObj.NumberOfFrames; % Number of files
vidHeight = runObj.Height; % Number of pixels in vertical (x) direction
vidWidth = runObj.Width; % Number of pixels in horizontal (z) direction
timeget = get(runObj, 'Duration'); % Duration of video (s)
rate = get(runObj, 'FrameRate'); % Capture rate (fps)

% Total of 200 frames captured
imin = 120; % First frame from run285 images
imax = 200; % Last frame from run285 images

%%%%%%%%%%%%%%%%%%%%%%%%%%%%%%%%%%%%%%%%%%%%%%%%%%%%%%%%%%%%%%%%%%%%%%%% Create timescale for calibrated plots %%%%%%%%%
% Work out time interval between frames
delta = timeget/nFrames;
% Work out time duration of 200 frames in s
timelength = imax*delta;
% Create time array based on the number of frames analysed
timerange = 0.2474:delta:(timelength-delta)+0.2474; % 0.2474s is the
difference
% between approximate start times of the flow in the calibrated
% and recorded data via the thermocouple
% Create new time axis to plot against
t3 = timerange(119:200);
%%%%%%%%%%%%%%%%%%%%%%%%%%%%%%%%%%%%%%%%%%%%%%%%%%%%%%%%%%%%%%%%%%%%%%%%
n = 420;
m = 120;

fname = ['..\285zip\RUN_285\run285_fr',int2str(imin),'.png'];
Aref = imread(fname);
linedataref = Aref(n,:);
col_array = [1:400];
row_array = [1:512];

for i = imin:imax,
    fname = ['..\285zip\RUN_285\run285_fr',int2str(i),'.png'];
    Afr1 = imread(fname);
    cnt_TCloc(i) = mean(mean(Afr1(343:345,86:88))); % Location of
thermocouple junction
    cnt_cornerloc(i) = mean(mean(Afr1(378:380,200:202))); % Approx. loc
of corner

    % Look at corner region and plot the surface temperature, heat flux
    % histories. Also generate contour maps
    cnt_cornerloc2(i) = mean(mean(Afr1(390:410,190:205))); % Second loc
of corner

end

%%%%%%%%%%%%%%%%%%%%%%%%%%%%%%%%%%%%%%%%%%%%%%%%%%%%%%%%%%%%%%%%%%%%%%%% DATA RECORDED WITH ACQUISITION SYSTEM
%%%%%%%%%%%%%%%%%%%%%%%%%%%%%%%%%%%%%%%%%%%%%%%%%%%%%%%%%%%%%%%%%%%%%%%%
v0 = v0 - mean(v0(1:1000)); %
Tw = v1*s1; % Convert thermocouple voltage values into temperature(degC)
p0=patm+(v0*s0); % Convert transducer voltage values into pascals and add
atmospheric pressure (kPa)

% Apply low-pass Butterworth filter for surface temperature values
[B,A]=butter(2,0.025);

```

```

Twf=filter(B,A,Tw); % Filter surface temperature values, Tw
Twf=Twf-mean(Twf(101:1201));
Twf(1:100)=Twf(101:200);

% This filter converts a surface temperature T to a heat transfer rate q
% for a semi-infinite substrate. It also gives an impulse response, h
fs=10e3; % Sampling rate (Hz)
np=1000; % Number of sample points
rrck=sqrt(rho*c*k); % Thermal product of perspex (TP)
test=0; % Refer Oldfield (2000) for details on this [
[h,shift]=desT2qsiimp1(fs,np,rrck,test); % Designs (des) a filter to
convert surface temperature T
% to heat transfer rate q (T2q) for a semi-infinite substrate (si)
% and gives impulse response (imp) h
q1=fftfilt(h,Twf); % Convert thermocouple readings (Tw) to q

% Apply low-pass Butterworth filter to heat flux near TC#2 values
[B1,A1]=butter(2,0.01);
qf1=filter(B1,A1,q1); % W/m^2
qf1=qf1/1000; % kW/m^2

%%%%%%%%%%%%%%%%%%%%%%%%%%%%%%%%%%%%%%%%%%%%%%%%%%%%%%%%%%%%%%%%%%%%%%%%
% Convert counts for thermocouple and corner region 1 locations into
% temperature values
T_TCloc = polyval(p3,double(cnt_TCloc)); % Thermocouple
T_cornerloc = polyval(p3,double(cnt_cornerloc)); % Corner region

% Shift temperature plots along vertical axis
T_TCloc = T_TCloc + 33;
T_cornerloc = T_cornerloc + 28;
t285 = zeros(size(T_TCloc));
t285(120:end) = time285;

%%%%%%%%%%%%%%%%%%%%%%%%%%%%%%%%%%%%%%%%%%%%%%%%%%%%%%%%%%%%%%%%%%%%%%%%
% Convert calibrated temperature to heat flux %%%%%%%%%%%%%
fs1=111; % Sampling rate (Hz)
np1=82; % Number of sample points
rrck=sqrt(rho*c*k); % Thermal product of perspex
test=0; % Test; see Oldfield (2000) for explanation
[h2,shift2]=desT2qsiimp1(fs1,np1,rrck,test);

%%%%%%%%%%%%%%%%%%%%%%%%%%%%%%%%%%%%%%%%%%%%%%%%%%%%%%%%%%%%%%%%%%%%%%%%
% Convert temperatures to heat flux values %%%%%%%%%%%%%
T_TCloc = [0 T_TCloc(120:200)];
q2=fftfilt(h2,T_TCloc); % Thermocouple
q3=fftfilt(h2,T_cornerloc); % Corner region

% % Create filter for heat flux values
[B3,A3]=butter(2,0.025);
qf2=filter(B3,A3,q2); % W/m^2
qf2=qf2/1000; % kW/m^2

%%%%%%%%%%%%%%%%%%%%%%%%%%%%%%%%%%%%%%%%%%%%%%%%%%%%%%%%%%%%%%%%%%%%%%%%
% Plot results %%%%%%%%%%%%%
% figure(1)
% plot(t,Twf)
% title('Recorded surface temperature at thermocouple during Run 285');
% axis([1.57 1.78 0 8]);
% grid on
%
```

```

figure(2)
plot(timerange(119:200),T_TCloc,'-o')
axis([1.58 1.78 0 8])
title('Calibrated surface temprature'), ylabel('T ( ^oC )'),xlabel('t
(s)');
grid on

figure(3)
plot(t,qf1)
title('Surface heat flux from recorded data'), xlabel('t (s)'),
ylabel('q_w (kW/m^2)');
%axis([1.57 1.78 0 20]);
grid on

figure(4)
plot(timerange,T_cornerloc,'-o')
title('Calibrated surface temperature in corner region'), ylabel('T ( ^oC
)'), xlabel('t (s)');
axis([1.57 1.78 0 25])
grid on

%%%%%%%%%%%%%%%%%%%%%%%%%%%%%%%%%%%%%%%%%%%%%%%%%%%%%%%%%%%%%%%%%%%%%%%%
%%%%%%%% CALIBRATED HEAT FLUX %%%%%%%%%
% Plot heat flux from Frame 140 to 175; map every 7th frame
figure(8)
subplot(2,3,1)
fname = ['..\285zip\RUN_285\run285_fr',int2str(147),'.png'];
Afr=imread(fname);
Tdata147 = polyval(p3,double(Afr));
q147=fftfilt(h2,Tdata147); % Convert IR calibrated temperature values to
q
qf147=filter(B3,A3,q147); % Units: W/m^2
qf147=qf147/1000; % kW/m^2
colormap('jet'), imagesc(qf147), colorbar, caxis([-15 40])
title('Surface heat flux - Frame 147')
h=colorbar;ylabel(h,'W/m^2')
grid on

subplot(2,3,2)
fname = ['..\285zip\RUN_285\run285_fr',int2str(154),'.png'];
Afr=imread(fname);
Tdata154 = polyval(p3,double(Afr));
q154=fftfilt(h2,Tdata154); % Convert IR calibrated temperature values to
q
qf154=filter(B3,A3,q154); % Units: W/m^2
qnorm154=qf154/1000; % kW/m^2
colormap('jet'), imagesc(qnorm154), colorbar, caxis([-15 40])
title('Surface heat flux - Frame 154')
h=colorbar;ylabel(h,'W/m^2')
grid on

subplot(2,3,3)
fname = ['..\285zip\RUN_285\run285_fr',int2str(161),'.png'];
Afr=imread(fname);
Tdata161 = polyval(p3,double(Afr));
q161=fftfilt(h2,Tdata161); % Convert IR calibrated temperature values to
q
qf161=filter(B3,A3,q161); % Units: W/m^2

```

```

qnorm161=qf161/1000; % kW/m^2
colormap('jet'), imagesc(qnorm161), colorbar, caxis([-15 40])
title('Surface heat flux - Frame 161')
h=colorbar;ylabel(h,'W/m^2')
grid on

subplot(2,3,4)
fname = ['..\285zip\RUN_285\run285_fr',int2str(168),'.png'];
Afr=imread(fname);
Tdata168 = polyval(p3,double(Afr));
q168=fftfilt(h2,Tdata168); % Convert IR calibrated temperature values to
q
qf168=filter(B3,A3,q168); % Units: W/m^2
qnorm168=qf168/1000; % kW/m^2
colormap('jet'), imagesc(qnorm168), colorbar, caxis([-15 40])
title('Surface heat flux - Frame 168')
h=colorbar;ylabel(h,'W/m^2')
grid on

subplot(2,3,5)
fname = ['..\285zip\RUN_285\run285_fr',int2str(175),'.png'];
Afr=imread(fname);
Tdata175 = polyval(p3,double(Afr));
q175=fftfilt(h2,Tdata175); % Convert IR calibrated temperature values to
q
qf175=filter(B3,A3,q175); % Units: W/m^2
qnorm175=qf175/1000; % kW/m^2
colormap('jet'), imagesc(qnorm175), colorbar, caxis([-15 40])
title('Surface heat flux - Frame 175')
h=colorbar;ylabel(h,'W/m^2')
grid on

subplot(2,3,6)
fname = ['..\285zip\RUN_285\run285_fr',int2str(182),'.png'];
Afr=imread(fname);
Tdata182 = polyval(p3,double(Afr));
q182=fftfilt(h2,Tdata182); % Convert IR calibrated temperature values to
q
qf182=filter(B3,A3,q182); % Units: W/m^2
qnorm182=qf182/1000; % kW/m^2
colormap('jet'), imagesc(qnorm182), colorbar, caxis([-15 40])
title('Surface heat flux - Frame 182')
h=colorbar;ylabel(h,'W/m^2')
grid on

%%%%%%%%%%%%%%%%%%%%%%%%%%%%%%%%%%%%%%%%%%%%%%%%%%%%%%%%%%%%%%%%%%%%%%%%
%
% CALIBRATED TEMPERATURE %
% Plot surface temperature from Frame 140 to 175; map every 7th frame
figure(9)
subplot(2,3,1)
fname = ['..\285zip\RUN_285\run285_fr',int2str(147),'.png'];
Afr=imread(fname);
Tdata147 = polyval(p3,double(Afr));
q147=fftfilt(h2,Tdata147); % Convert IR calibrated temperature values to
q
qf147=filter(B3,A3,q147); % Units: W/m^2
qf147=qf147/1000; % kW/m^2

```

```
colormap('jet'), imagesc(Tdata147), colorbar, caxis([-15 40])
title('Surface temperature - Frame 147')
h=colorbar;ylabel(h, '^oC')
grid on

subplot(2,3,2)
fname = ['..\285zip\RUN_285\run285_fr',int2str(154),'.png'];
Afr=imread(fname);
Tdata154 = polyval(p3,double(Afr));
q154=fftfilt(h2,Tdata154); % Convert IR calibrated temperature values to
q
qf154=filter(B3,A3,q154); % Units: W/m^2
qnorm154=qf154/1000; % kW/m^2
colormap('jet'), imagesc(Tdata154), colorbar, caxis([-15 40])
title('Surface temperature - Frame 154')
h=colorbar;ylabel(h, '^oC')
grid on

subplot(2,3,3)
fname = ['..\285zip\RUN_285\run285_fr',int2str(161),'.png'];
Afr=imread(fname);
Tdata161 = polyval(p3,double(Afr));
q161=fftfilt(h2,Tdata161); % Convert IR calibrated temperature values to
q
qf161=filter(B3,A3,q161); % Units: W/m^2
qnorm161=qf161/1000; % kW/m^2
colormap('jet'), imagesc(Tdata161), colorbar, caxis([-15 40])
title('Surface temperature - Frame 161')
h=colorbar;ylabel(h, '^oC')
grid on

subplot(2,3,4)
fname = ['..\285zip\RUN_285\run285_fr',int2str(168),'.png'];
Afr=imread(fname);
Tdata168 = polyval(p3,double(Afr));
q168=fftfilt(h2,Tdata168); % Convert IR calibrated temperature values to
q
qf168=filter(B3,A3,q168); % Units: W/m^2
qnorm168=qf168/1000; % kW/m^2
colormap('jet'), imagesc(Tdata168), colorbar, caxis([-15 40])
title('Surface temperature - Frame 168')
h=colorbar;ylabel(h, '^oC')
grid on

subplot(2,3,5)
fname = ['..\285zip\RUN_285\run285_fr',int2str(175),'.png'];
Afr=imread(fname);
Tdata175 = polyval(p3,double(Afr));
q175=fftfilt(h2,Tdata175); % Convert IR calibrated temperature values to
q
qf175=filter(B3,A3,q175); % Units: W/m^2
qnorm175=qf175/1000; % kW/m^2
colormap('jet'), imagesc(Tdata175), colorbar, caxis([-15 40])
title('Surface temperature - Frame 175')
h=colorbar;ylabel(h, '^oC')
grid on

subplot(2,3,6)
```

```

fname = ['..\285zip\RUN_285\run285_fr',int2str(182),'.png'];
Afr=imread(fname);
Tdata182 = polyval(p3,double(Afr));
q182=fftfilt(h2,Tdata182); % Convert IR calibrated temperature values to
q
qf182=filter(B3,A3,q182); % Units: W/m^2
qnorm182=qf182/1000; % kW/m^2
colormap('jet'), imagesc(Tdata182), colorbar, caxis([-15 40])
title('Surface temperature - Frame 182')
h=colorbar;ylabel(h,'^oC')
grid on

%%%%%%%%%%%%%%%%%%%%%%%%%%%%%%%%%%%%%%%%%%%%%%%%%%%%%%%%%%%%%%%%%%%%%%%% FRAME 170
%%%%%%%%%%%%%%%%%%%%%%%%%%%%%%%%%%%%%%%%%%%%%%%%%%%%%%%%%%%%%%%%%%%%%%%%
%%%%%%%% Identify peak heating region %%%%%%%%%
figure(10)
subplot(1,2,1)
fname = ['..\285zip\RUN_285\run285_fr',int2str(170),'.png'];
Afr=imread(fname);
Tdata170 = polyval(p3,double(Afr));
q170=fftfilt(h2,Tdata170); % Convert IR calibrated temperature values to
q
qf170=filter(B3,A3,q170); % Units: W/m^2
qf170=qf170/1000; % kW/m^2
colormap('jet'), imagesc(qf170), colorbar, caxis([-20 60])
title('Surface heat flux - Frame 170')
h=colorbar;title(h,'kW/m^2')
grid on

%%%%%%%% Generate filled contour map %%%%%%%%%
subplot(1,2,2)
colormap('jet')
[C,L]=contourf(qf170(350:420,190:220));
r=[0 0 1];
colorbar, caxis([-20 60]),clabel(C,L)
title('Surface heat flux - Filled Contour Map for Frame 170')
h=colorbar;title(h,'kW/m^2')
set(gca,'YDir','reverse');
grid on
%%%%%%%%%%%%%%%%%%%%%%%%%%%%%%%%%%%%%%%%%%%%%%%%%%%%%%%%%%%%%%%%%%%%%%%% FRAME 175
%%%%%%%%%%%%%%%%%%%%%%%%%%%%%%%%%%%%%%%%%%%%%%%%%%%%%%%%%%%%%%%%%%%%%%%%
%%%%%%%% Identify peak heating region %%%%%%%%%
figure(11)
subplot(1,2,1)
fname = ['..\285zip\RUN_285\run285_fr',int2str(175),'.png'];
Afr=imread(fname);
Tdata175 = polyval(p3,double(Afr));
q175=fftfilt(h2,Tdata175); % Convert IR calibrated temperature values to
q
qf175=filter(B3,A3,q175); % Units: W/m^2
qf175=qf175/1000; % kW/m^2
colormap('jet'), imagesc(qf175), colorbar, caxis([-10 70])
title('Surface heat flux - Frame 175')
h=colorbar;title(h,'kW/m^2')
grid on

%%%%%%%% Generate filled contour map %%%%%%%%%

```

```

subplot(1,2,2)
colormap('jet')
[C,L]=contourf(qf175(350:420,190:220));
r=[0 0 1];
colorbar, caxis([-10 70]),clabel(C,L)
title('Surface heat flux - Filled Contour Map for Frame 175')
h=colorbar;title(h,'kW/m^2')
set(gca,'YDir','reverse');
grid on

%%%%%%%%%%%%%%%%%%%%%%%%%%%%%%%%%%%%%%%%%%%%%%%%%%%%%%%%%%%%%%%%%%%%%%%% FRAME 185
%%%%%%%%%%%%%%%%%%%%%%%%%%%%%%%%%%%%%%%%%%%%%%%%%%%%%%%%%%%%%%%%%%%%%%%%
%%%%%%%% Identify peak heating region %%%%%%%%%
figure(12)
subplot(1,2,1)
fname = ['..\285zip\RUN_285\run285_fr',int2str(185),'.png'];
Afr=imread(fname);
Tdata185 = polyval(p3,double(Afr));
q185=fftfilt(h2,Tdata185); % Convert IR calibrated temperature values to
q
qf185=filter(B3,A3,q185); % Units: W/m^2
qf185=qf185/1000; % kW/m^2
colormap('jet'), imagesc(qf185), colorbar, caxis([-10 70])
title('Surface heat flux - Frame 185')
h=colorbar;title(h,'kW/m^2')
grid on

%%%%%%%% Generate filled contour map %%%%%%%%%
subplot(1,2,2)
colormap('jet')
[C,L]=contourf(qf185(350:420,190:220));
r=[0 0 1];
colorbar, caxis([-10 70]),clabel(C,L)
title('Surface heat flux - Filled Contour Map for Frame 185')
h=colorbar;title(h,'kW/m^2')
set(gca,'YDir','reverse');
grid on

%%%%%%%% Identifying boundary layer separation/reattachment %%%%%%%%%

for i = imin:imax,
    fname = ['..\285zip\RUN_285\run285_fr',int2str(i),'.png'];
    Afr1 = imread(fname);

    cntdata1(i) = (Afr1(400,190));
    cntdata2(i) = (Afr1(420,190));
    cntdata3(i) = (Afr1(440,190));
    cntdata4(i) = (Afr1(400,205));
    cntdata5(i) = (Afr1(420,205));
    cntdata6(i) = (Afr1(440,205));
    cntdata7(i) = (Afr1(400,220));
    cntdata8(i) = (Afr1(420,220));
    cntdata9(i) = (Afr1(440,220));

end

```

```

% % Shift temperature plots along vertical axis
% T_TCloc = T_TCloc + 33;
% T_cornerloc = T_cornerloc + 28;
% t285 = zeros(size(T_TCloc));
% t285(120:end) = time285;

%%%%% Convert calibrated temperature to heat flux %%%%%%%%%%%%%%
fs4=1000; % Sampling rate (Hz)
np4=82; % Number of sample points
rrck=sqrt(rho*c*k); % Thermal product of perspex
test=0; % Test; see Oldfield (2000) for explanation
[h4,shift]=desT2qsiimp1(fs4,np4,rrck,test);

% Convert counts to temperature values
Tdata1 = polyval(p3,double(cntdata1));
Tdata2 = polyval(p3,double(cntdata2));
Tdata3 = polyval(p3,double(cntdata3));
Tdata4 = polyval(p3,double(cntdata4));
Tdata5 = polyval(p3,double(cntdata5));
Tdata6 = polyval(p3,double(cntdata6));
Tdata7 = polyval(p3,double(cntdata7));
Tdata8 = polyval(p3,double(cntdata8));
Tdata9 = polyval(p3,double(cntdata9));

%%%%%%%%% Convert temperatures to heat flux values %%%%%%%%%%%%%%
qdata1=fftfilt(h4,Tdata1); % Location 1
qdata2=fftfilt(h4,Tdata2); % Location 2
qdata3=fftfilt(h4,Tdata3); % Location 3
qdata4=fftfilt(h4,Tdata4); % Location 4
qdata5=fftfilt(h4,Tdata5); % Location 5
qdata6=fftfilt(h4,Tdata6); % Location 6
qdata7=fftfilt(h4,Tdata7); % Location 7
qdata8=fftfilt(h4,Tdata8); % Location 8
qdata9=fftfilt(h4,Tdata9); % Location 9

% % Create filter for heat flux values
[B3,A3]=butter(5,0.025);
qfdata1=filter(B3,A3,qdata1); % W/m^2
qfdata1=qfdata1/1000; % kW/m^2

qfdata2=filter(B3,A3,qdata2); % W/m^2
qfdata2=qfdata2/1000; % kW/m^2

qfdata3=filter(B3,A3,qdata3); % W/m^2
qfdata3=qfdata3/1000; % kW/m^2

qfdata4=filter(B3,A3,qdata4); % W/m^2
qfdata4=qfdata4/1000; % kW/m^2

qfdata5=filter(B3,A3,qdata5); % W/m^2
qfdata5=qfdata5/1000; % kW/m^2

qfdata6=filter(B3,A3,qdata6); % W/m^2
qfdata6=qfdata6/1000; % kW/m^2

```



```
qfdata7=filter(B3,A3,qdata7); % W/m^2
qfdata7=qfdata7/1000; % kW/m^2

qfdata8=filter(B3,A3,qdata8); % W/m^2
qfdata8=qfdata8/1000; % kW/m^2

qfdata9=filter(B3,A3,qdata9); % W/m^2
qfdata9=qfdata9/1000; % kW/m^2

% Plot
figure(13)
plot(timerange,qfdata1,'-o',timerange,qfdata2,'-or',timerange,qfdata3,'-
ok')
grid on

figure(14)
plot(timerange,qfdata4,'-o',timerange,qfdata5,'-or',timerange,qfdata6,'-
ok')
grid on

figure(15)
plot(timerange,qfdata7,'-o',timerange,qfdata8,'-or',timerange,qfdata9,'-
ok')
grid on

figure(16)
plot(timerange,Tdata1,'-o',timerange,Tdata2,'-or',timerange,Tdata3,'-ok')
xlabel('t(s)'), ylabel('T ( ^oC )')
grid on
% axis([1.57 1.78

figure(17)
plot(timerange,Tdata4,'-o',timerange,Tdata5,'-or',timerange,Tdata6,'-ok')
xlabel('t(s)'), ylabel('T ( ^oC )')
axis([1.57 1.8 -10 50]);
grid on

figure(18)
plot(timerange,Tdata7,'-o',timerange,Tdata8,'-or',timerange,Tdata9,'-ok')
xlabel('t(s)'), ylabel('T ( ^oC )')
grid on
```